Novel Nanostructure Electrocatalysts for Oxygen Reduction and Hydrogen Evolution Reactions

By

Lin Luo

A thesis submitted in fulfilment of the requirements for the degree of Doctor of Philosophy in the Department of Chemistry, University of the Western Cape, South Africa

September 2019

UNIVERSITY of the
WESTERN CAPE

Supervised by

Prof. Salam Titinchi

Dr Hanna Abbo

http://etd.uwc.ac.za/

Abstract

The widespread use of fossil energy has been most convenient to the world, while they also cause environmental pollution and global warming. Therefore, it is necessary to develop clean and renewable energy sources, among which, hydrogen is considered to be the most ideal choice, which forms the foundation of the hydrogen energy economy, and the research on hydrogen production and fuel cells involved in its production and utilization are naturally a vital research endeavor in the world.

Electrocatalysts are one of the key materials for proton exchange member fuel cells (PEMFCs) and water splitting. The use of electrocatalysts can effectively reduce the reaction energy barriers and improve the energy conversion efficiency. This thesis mainly focuses on development novel nanostructure electrocatalysts with low-cost, high activity and good durability used for oxygen reduction reaction (ORR) and hydrogen evolution.

(1) Nitrogen-doped PtNiMo ternary alloys were synthesized by impregnation reduction followed by annealing at high temperatures. The introduction of acid-resistant Mo atoms in the alloy not only stabilizes the near-surface Pt atoms, enhancing the catalytic stability, but also changes the electronic structure of adjacent Pt atoms and thus promote the desorption of oxide intermediates. The doped N can form Ni_4N with Ni at high temperature and is stabilized in the electrocatalyst to thus improve stability. Meanwhile, the pyridine N and pyrrole N also formed by annealing the carbon substrate in an NH_3 atmosphere and possess a promoting effect on oxygen reduction. By adjusting the near-surface Pt atom's content to balance the activity and stability, Pt_3Ni_3MoN/C shows the best activity

UNIVERSITY of the
WESTERN CAPE

http://etd.uwc.ac.za/

and stability. It showed mass activity of 900 mA mg^{-1} Pt at 0.90V *vs*. RHE in O_2-saturated 0.1 mol L^{-1} $HClO_4$ aqueous solutions, which is 3.75-fold higher compared with the commercial Pt/C (240 mA mg^{-1} Pt). After 30k accelerated durability tests, the mass activity of Pt_3Ni_3MoN/C is still 690 mA mg^{-1} Pt, which activity remains ~75%, while the Pt/C merely retains ~44%.

(2) Fabrication of self-supported Cu_2S-Cu_3P NW arrays on cupper foam by liquid-solid reaction and subsequent phosphidation at low temperature are used as an integrated electrode for hydrogen evolution (HER). No binding agents are needed to favor excellent catalytic activity for HER and it only requires a low overpotential of 158 mV to achieve a current density of 10 mA cm^{-2} and it displays a small Tafel slope of 45 mV dec^{-1}. In addition, the activity decrease is ignorable after holding at –500 mA cm^{-2} for a period of 75 h which demonstrates excellent stability, and the possible mechanisms are also discussed in the thesis.

(3) A two-step method was developed to fabricate a self-supported nanosheets arrays Ni-Co-P/NF nanocomposite electrode for hydrogen evolution. It was displayed that the bimetallic cobalt-nickel phosphide has great potential for HER at high current densities. The as-prepared Ni-Co-P/NF electrode exhibits a very good HER activity with overpotential of 85 mV and shows high stability for 24 h in 1.0 M KOH aqueous solution, the reasons for such good performance are also discussed. This work provides a mechanism for the synthesis of low-cost electrocatalyst with high efficiency for hydrogen evolution, which also offers a promising opportunity for the large-scale application of phosphides in alkaline electrolysis ascribed to their higher current density and impressive low overpotential.

UNIVERSITY of the
WESTERN CAPE

http://etd.uwc.ac.za/

Keywords

Proton exchange membrane fuel cells

Oxygen reduction reaction

Water splitting

Hydrogen evolution reaction

Electrocatalyst

Activity

Stability.

UNIVERSITY of the
WESTERN CAPE

http://etd.uwc.ac.za/

Declaration

I declare that **"Novel nanostructure electrocatalysts for oxygen reduction and hydrogen evolution reactions"** is my own work, that it has not been submitted for any degree or examination in any other university, and that all the sources I have used or quoted have been indicated and acknowledged by complete references.

Full name: Lin Luo Date: 3 Sept 2019

Signed:… Luo Lin ..

UNIVERSITY of the
WESTERN CAPE

http://etd.uwc.ac.za/

Acknowledgements

I would like to take this opportunity to express my deepest gratitude to Prof. Salam Titinchi and Dr. Hanna Abbo for their invaluable guidance and unique approach to the PhD research work in this thesis. They are not only my supervisors but also my good friends. Prof. Titinchi is hard working and his constant interest in developing his profession coupled with his dedicated work ethic impressed and motivated me to improve myself. I would also like to thank my co-supervisor Dr Abbo, who shared her knowledge, experience and skills throughout my PhD studies, and also assisted me to improve the quality of the publications and the thesis.

I would also like to thank my lab colleagues Jiajia Lu, Chen Yu, Fei Xu, Shouquan Feng, Mei Tang, Zhiyi Pan for their support during my studies. I would also like to thank the academic staff in the Chemistry Department for their support during my PhD studies at the University of the Western Cape.

I would like to express my appreciation to the Collaborative Innovation Center of Sustainable Energy Materials (CICSEM) in Guangxi University who provided much of the equipment to finish the thesis. I further extend my appreciation to Prof. Pei Kang Shen, Zhiqun Tian, Shibin Yin and their center for the valuable opportunity to do the work. Further thanks to Prof. Panagiotis Tsiakaras's who is such a good man for his support at the Laboratory of Alternative Energy Conversion Systems, Department of Mechanical Engineering, School of Engineering, University of Thessaly for the works he assisted me with and I wish him and Marina an enjoyable and good life.

UNIVERSITY of the
WESTERN CAPE

http://etd.uwc.ac.za/

I would like to thank the financial support provided by the Natural Science Foundation of China (21872040), the Natural Science Foundation of Guangxi (2016GXNSFCB380002) and the Nanning Science and Technology Project (20171107).

I would like to thank my family for their encouragement and support. Finally, I greatly value the emotional support from my parents, their love and belief in me throughout the PhD project.

UNIVERSITY of the
WESTERN CAPE

http://etd.uwc.ac.za/

Dedication

I dedicate this work to my mother, father, sister, my husband, daughter, and son.

UNIVERSITY of the
WESTERN CAPE

http://etd.uwc.ac.za/

Table of Contents

Abstract i

Keywords iii

Declaration iv

Acknowledgements v

Dedication vii

Table of Contents viii

List of Figures xii

List of Tables xvii

List of Acronyms xviii

CHAPTER 1 Introduction 1

1.1 Introduction of PEMFCs 3

1.1.1 Principle of PEMFCs 4

1.1.2 Components of PEMFCs 5

1.2 Oxygen Reduction Reaction 6

1.2.1 Principle of Oxygen Reduction Reaction 7

1.2.2 Development of ORR Electrocatalysts 11

1.3 Introduction of Water Splitting 14

1.3.1 Electrolytic Water Devices 16

1.3.2 Basic Mechanisms for Water Splitting 20

1.3.3 Evaluation the Activity of HER Electrocatalysts 22

UNIVERSITY of the
WESTERN CAPE

http://etd.uwc.ac.za/

1.3.4 Development of HER Electrocatalysts 25

1.4 Significance and Novelty of This Thesis 28

1.4.1 Significance of This Thesis 28

1.4.2 Novelty of This Thesis 29

1.5 References 31

CHAPTER 2 Physico-Chemical Characterization 38

2.1 X-ray Powder Diffraction (XRD) 38

2.2 X-ray Photoelectron Spectroscopy (XPS).....39

2.3 BET Specific Surface Area 39

2.4 Scanning Electron Microscope (SEM).....40

2.5 Transmission Electron Microscope (TEM).....41

2.6 References 42

CHAPTER 3 Enhancement of ORR via the Introduction of the Acid-Resistant Refractory Mo and Regulating the Near-Surface Pt Content.....43

3.1 Introduction 43

3.2 Experimental 46

3.2.1 Electrocatalysts Preparation 46

3.2.2 Electrocatalysts Characterization 47

3.3 Results and Discussions 49

3.3.1 Physico-Chemical Characterization 49

3.3.2 The Effect of Mo on the ORR Kinetics 57

UNIVERSITY of the
WESTERN CAPE

http://etd.uwc.ac.za/

3.3.3 The Regulation of Near-Surface Pt Content in PtNiMoN Alloy.....59

3.4 Conclusion 63

3.5 References 64

CHAPTER 4 Investigation of Cu_2S-Cu_3P Nanowire Arrays Self-Supported on Copper Foam for HER 68

4.1 Introduction 68

4.2 Experimental 71

4.2.1 Materials 71

4.2.2 Synthesis of $Cu(OH)_2$ NW Arrays.....71

4.2.3 Synthesis of Cu_2S-Cu_3P NW Arrays 71

4.2.4 Physico-Chemical Characterization 72

4.3 Results and Discussions 74

4.4 Conclusions 90

4.5 References 91

CHAPTER 5 Bimetallic Ni-Co Phosphide Nanosheets Self-Supported on Nickel Foam as High-Performance Electrocatalyst for Hydrogen Evolution Reaction.....97

5.1 Introduction 97

5.2 Experimental 101

5.2.1 Materials 101

5.2.2 Preparation of Ni-Co/NF, Co/NF and Ni/NF 101

UNIVERSITY of the
WESTERN CAPE

http://etd.uwc.ac.za/

5.2.3 Preparation of Ni-Co-P/NF, Co-P/NF and Ni-P/NF.....102

5.2.4 Physico-Chemical Characterization 102

5.3 Results and Discussions 104

5.4. Conclusions 126

5.5 References 127

CHAPTER 6 Conclusion and Prospective 134

UNIVERSITY of the
WESTERN CAPE

http://etd.uwc.ac.za/

List of Figures

Figure 1.1 Principle of a PEMFCs. 4

Figure 1.2 Principle of MEA. 5

Figure 1.3 The mechanisms of oxygen reduction reaction. 8

Figure 1.4 Trends in oxygen reduction activity plotted as a function of the oxygen binding energy.[27] 10

Figure 1.5 Trends in oxygen reduction activity plotted as a function of both the O and the OH binding energy.[27] 10

Figure 1.6 Schematic of various electrocatalyst development strategies, which aim to increase the number of active sites and/or increase the intrinsic activity of each active site.[53] 14

Figure 1.7 Various energy driven water splitting routes by using thermal, electrical, biochemical and photonic energy or their combinations.[56] 15

Figure 1.8 The principle of alkaline electrolyte water electrolysis. 17

Figure 1.9 Principle of proton exchange membrane water electrolyzer. 18

Figure 1.10 Principle of solid oxide water electrolyzer. 19

Figure 1.11 A volcano plot of experimentally measured exchange current density as a function of the DFT-calculated Gibbs free energy of hydrogen adsorption on pure metals.[69] 25

Figure 1.12 Elements that are used for constructing HER electrocatalysts.[86].. 27

Figure 1.13 Crustal abundance of metals that are used for constructing HER electrocatalysts.[86] 27

Figure 3.1 Schematic diagram for the synthesis of PtNiMo alloy electrocatalysts. 46

UNIVERSITY of the
WESTERN CAPE

http://etd.uwc.ac.za/

Figure 3.2 (a) XRD curves of the as-prepared samples with a scan rate of 5 min^{-1}. (b) Curve fitting for (220) diffraction peaks in part (a). 49

Figure 3.3 (a-c) TEM and HRTEM images of Pt_3Ni_3MoN/C, (d) HAADF-STEM image, (e) HRTEM image of a Pt_3Ni_3MoN alloy nanoparticle, (f) Overlapped mapping image of (g) Pt, (h) Ni, (i) Mo and (j) N elements. 52

Figure 3.4 (a) A TEM image of Pt_3Ni_3MoN/C and the corresponding distribution map of particle size before testing, (b) A TEM image of Pt_3Ni_3MoN/C and the corresponding distribution map of particle size after 30k CV cycles testing. 52

Figure 3.5 (a−c) Line profiles of Pt, Ni and Mo for Pt_3Ni_5MoN/C, Pt_3Ni_3MoN/C, and Pt_3NiMoN/C nanoparticles. The red arrows indicate the directions of the line profiles..... 53

Figure 3.6 (a-c) XPS peaks of N1s in Pt_3Ni_5MoN/C, Pt_3Ni_3MoN/C, and Pt_3NiMoN/C nanoparticles, respectively. 53

Figure 3.7 (a) XPS spectra of the investigated materials: (b) Ni2p, (c) Pt4f, and (d) Mo3d. 54

Figure 3.8 (a) ORR polarization curves of Pt_3Ni_3MoN/C and PtNiN/C in O_2-saturated 0.1 mol L^{-1} $HClO_4$ aqueous solutions before and after ADT, 25ºC, scan rate 5 mV s^{-1}, rotating rate 1,600 rpm; (b) Comparison of MA before and after 30k cycles; (c) Comparison of MA during the ADT at 0.90 V; (d) Comparison of ECSA during the ADT. 57

Figure 3.9 (a) Comparison of MA during ADT at 0.90 V; (b) Comparison of ECSA during ADT. 59

UNIVERSITY of the
WESTERN CAPE

http://etd.uwc.ac.za/

Figure 3.10 (a-d) CO stripping before and after ADT, by maintaining the potential at 0.15 V for 15 min in CO and 30 min in aqueous solutions saturated with N_2 and acidified with $HClO_4$ (0.10 mol L^{-1}), 20 mV s^{-1}. 60

Figure 3.11 (a-d) ORR polarization curves of Pt_3Ni_5MoN/C, Pt_3Ni_3MoN/C, Pt_3NiMoN/C and TKK Pt/C in O_2-saturated 0.1 mol L^{-1} $HClO_4$ aqueous solutions before and after ADT, 25°C, scan rate 5 mV s^{-1}, rotating rate 1,600 rpm. (e-h) MAs for Pt_3Ni_5MoN/C, Pt_3Ni_3MoN/C, Pt_3NiMoN/C compared with Pt/C before and after 30k cycles..... 61

Scheme 4.1 Schematic illustration of the synthesis of Cu_2S-Cu_3P NW arrays on copper foam..... 72

Figure 4.1 XRD curves of the samples with a scan rate of 10° min^{-1}. (a) Cu_2S-Cu_3P NW arrays. (b) $Cu(OH)_2$ NW arrays, (c) Cu_2S NW arrays, (d) Cu_3P NW arrays..... 75

Figure 4.2 (a) XPS summary of Cu_2S NW arrays, the corresponding (b) Cu2p and (c) S2p; (d) XPS summary of Cu_3P NW arrays, the corresponding (e) Cu2p and (f) P2p. 77

Figure 4.3 (a) XPS summary of Cu_2S-Cu_3P NW arrays, the corresponding (b) Cu2p, (c) S2p and (d) P2p..... 78

Figure 4.4 (a-e) SEM and EDS images of $Cu(OH)_2$ NW arrays, (f-j) SEM and EDS maps of Cu_2S-Cu_3P NW arrays. 79

Figure 4.5 SEM and EDS images of Cu2S NW arrays..... 80

Figure 4.6 SEM and EDS pictures of Cu_3P NW arrays. 80

Figure 4.7 (a-c) TEM and HRTEM images of Cu_2S-Cu_3P NW arrays. (d-g) Dark field image and element mapping images of Cu, S and P..... 82

UNIVERSITY of the
WESTERN CAPE

http://etd.uwc.ac.za/

Figure 4.8 Electrochemical measurements of the samples for hydrogen evolution in 1.0 M KOH aqueous solution. (a, b) Polarization curves and the corresponding Tafel plots. (c) Nyquist plots in frequency values from 100 kHz to 100 mHz. (d) The chronopotentiometry curve of Cu_2S-Cu_3P NW arrays holding at –500 mA cm^{-2} for lasting 75 h. 83

Figure 4.9 (a-e) Double-layer capacitance measurements for determining the electrochemically active surface area for all the electrocatalysts from voltammetry in 1.0 M KOH with different scan rates. (f) The capacitive currents at 0.20 V against the scan rate. (g) HER activities (current density) of the samples are normalized by their ESCA. 86

Figure 4.10 SEM and EDS pictures of Cu_2S-Cu_3P NW arrays after the stability test. 89

Figure 5.1 Schematic illustration for the synthesis of Ni-Co-P/NF. 104

Figure 5.2 XRD pattern of Ni-Co-P/NF electrocatalyst. 105

Figure 5.3 (a) XRD pattern of Ni-Co/NF, Co/NF; (b) curve fittings of (100) diffraction peaks in (a) that marked as black frame. 106

Figure 5.4 (a) SAED pattern and (b) XRD curves for Ni-Co/NF; the XRD with a scan rate of 5° min^{-1}, and the insert picture is shows curve fittings for (111) and (220) diffraction peaks. 107

Figure 5.5 (a) XRD pattern of Co-P/NF, Co/NF; (b) XRD pattern of Ni-P/NF, Ni/NF and NF. 108

Figure 5.6 (a) XPS summary of Ni-Co-P/NF and Ni-Co/NF, (b) Co2p, (c) Ni2p, (d) P2p and O1s of (e) Ni-Co/NF and (f) Ni-Co-P/NF. 109

Figure 5.7 SEM (a–c) and EDS (d–f) images of Ni-Co/NF precursor. 111

UNIVERSITY of the
WESTERN CAPE

http://etd.uwc.ac.za/

Figure 5.8 SEM (a–c) and EDS (d–g) images of Ni-Co-P/NF..... 112

Figure 5.9 SEM (a–c) and EDS (d–f) images of Co/NF electrocatalyst. 113

Figure 5.10 SEM (a–c) and EDS (d–g) images of Co-P/NF electrocatalyst..... 113

Figure 5.11 SEM (a–c) and EDS (d–e) images of Ni/NF electrocatalyst. 114

Figure 5.12 SEM (a–c) and EDS (d–f) images of Ni-P/NF electrocatalyst. 115

Figure 5.13 (a) TEM image of Ni-Co-P/NF, (b) the corresponding SAED pattern taken from (a), (c–f) HRTEM images, (g–j) the corresponding EDX mappings of Co, Ni, P and O elements. 116

Figure 5.14 Electrochemical measurements of the as-prepared samples for hydrogen evolution in 1.0 M KOH aqueous solution. (a) Polarization curves, (b) corresponding Tafel plots, (c) comparison of the HER activity in 1.0 M KOH aqueous solution for newly reported non-noble metal-based electrocatalysts, (d) chronopotentiometry curve with a constant current at –10 mA cm^{-2}. 118

Figure 5.15 Nyquist plots in frequency from 10^5 to 10^2 Hz with a single modulated in 1.0 M KOH aqueous solution for hydrogen evolution reaction.... 121

Figure 5.16 (a–g) Double-layer capacitance measurements for determining the ECSAs of all the electrocatalysts from voltammetry curves in 1.0 M KOH with different scan rates. (h) The capacitive currents at 0.20 V against the scan rates. 122

Figure 5.17 (a) The normalized HER activities (current density) by their ESCAs; (b) the corresponding Tafel slopes. 124

Figure 5.18 The Contact angles of (a) Ni-Co/NF and (b) Ni-Co-P/NF. 124

Figure 5.19 (a) Before and (b) after ultrasonication for 30 min..... 125

UNIVERSITY of the
WESTERN CAPE

http://etd.uwc.ac.za/

List of Tables

Table 3.1 Structural parameters of the samples extracted from X-ray powder diffraction. 51

Table 3.2 Contents and atomic ratios of Pt to Ni to Mo in all the investigated samples. 56

Table 3.3 Half-wave potentials ($E_{1/2}$) of Pt_3Ni_5MoN/C, Pt_3Ni_3MoN/C, Pt_3NiMoN/C, and TKK Pt/C. 62

Table 3.4 Mass activities for the prepared samples at 0.9 V. 62

Table 4.1 Comparison HER activities in 1.0 M KOH aqueous solution for Cu_2S-Cu_3P NW arrays with literatures recently reported. 84

Table 4.2 HER activity of different electrocatalysts. 88

Table 5.1 Comparison of the HER activity in 1.0 M KOH aqueous solution for several reported non-noble metal-based electrocatalysts (GCE means glassy carbon electrode, CFP means carbon fiber paper, CF means carbon fiber, CNS means carbon nanosheets). 120

Table 5.2 The ECSAs, η_{10} and Tafel slopes of all samples. 123

UNIVERSITY of the
WESTERN CAPE

http://etd.uwc.ac.za/

List of Acronyms

PEMFCs	proton exchange member fuel cells
HER	hydrogen evolution reaction
OER	oxygen evolution reaction
ORR	oxygen reduction reaction
PGM	platinum group metal
AFCs	alkaline fuel cells
PAFCs	phosphate fuel cells
MCFCs	molten carbonate fuel cells
SOFCs	solid oxide fuel cells
MEA	membrane electrode assembly
ESCAs	electrochemically active surface area
E-TEM	environmental spherical aberration transmission electron microscope
PEM	proton exchange membrane
SOE	solid-oxide electrolyzer
ΔG_{H^*}	hydrogen adsorption value
DFT	Density functional theory
XRD	X-ray powder diffraction
XPS	X-ray photoelectron spectroscopy
BET	Brunauer-Emmet-Teller
SEM	scanning electron microscopy
FESEM	field emission scanning electron microscopy
TEM	transmission electron microscopy

UNIVERSITY of the
WESTERN CAPE

http://etd.uwc.ac.za/

STEM	scanning transmission electron microscopy
EDX	energy dispersive X-ray spectroscopy
EELS	electron energy-loss spectroscopy
NCNCs	nitrogen-doped carbon nanocages
ADTs	accelerated durability tests
RHE	reversible hydrogen electrode
GCD	glassy carbon disk
CV	cyclic voltammetry
RDE	rotating disk electrode
fcc	face centered cubic
θ_{max}	peak maximum
$B_{2\theta}$	half-maximum
PCs	polarization curves
MA	mass activity
K-L equation	Koutecky-Levich equation
I_k	kinetic currents
I_d	diffusion limited current
CF	copper foam
TMCs	Transition metal chalcogenides
NW	nanowire
EIS	electrochemical impedance spectroscopy
CA	chronoamperometry
C_{dl}	double-layer capacitance
KOH	Potassium hydroxide

UNIVERSITY of the
WESTERN CAPE

http://etd.uwc.ac.za/

HCl	hydrochloric acid
$C_4H_6CoO_4 \cdot 4H_2O$	cobalt acetate tetrahydrate
$NiCl_2 \cdot 6H_2O$	nickel chloride hexahydrate
NH_4Cl	ammonium chloride
$NaHPO_2 \cdot H_2O$	sodium hypophosphite
C_2H_5OH	anhydrous ethanol
C_2H_5OH	ethanol
N_2	nitrogen
EDS	elemental mapping analysis
EDX	Energy Dispersive X-ray spectroscopy
HRTEM	high-resolution transmission electron microscopy
SAED	selected area electron diffraction
CP	chronopotentiometry
ECSAs	electrochemical active surface areas
FeP	iron phosphides
MoP	molybdenum phosphides
Cu_3P	copper phosphides

UNIVERSITY of the
WESTERN CAPE

http://etd.uwc.ac.za/

CHAPTER 1 Introduction

The widespread use of fossil energy has on the one hand been most convenient to the world, while on the other hand also causes adverse consequences such as environmental pollution and global warming. In order to achieve the sustainable development of human society and not adversely affect the environment, it is essential to develop clean and renewable energy sources, such as solar energy, wind energy, tidal energy, and similar non-destructive processes. Hydrogen derived energy is considered to be the most ideal choice, which forms the foundation of the hydrogen energy economy, and the research on hydrogen production and fuel cells involved in its production and utilization are naturally a vital research endeavor in the world.

Electrocatalysts are one of the key materials for proton exchange member fuel cells (PEMFCs) and water splitting. The use of electrocatalysts can effectively reduce the reaction energy barriers and improve the corresponding energy conversion efficiency.[1, 2]

UNIVERSITY of the
WESTERN CAPE

Hydrogen with a high energy density has been widely investigated as an ideal energy source for a sustainable development venture with the only by-product being water without carbon dioxide production.[3] However, large-scale hydrogen production currently arises from the steam reforming of fossil fuels. Accordingly, the search for green methods to produce H_2 is crucial for the hydrogen energy economy. Among the various methods, water electrolysis, which uses electricity obtained from renewable energy sources (e.g., wind and solar), is an ideal method to produce H_2 due to its high conversion efficiencies and zero carbon dioxide emission. Water electrolysis is a promising approach for large-scale and sustainable hydrogen production.[4] Presently, hydrogen produced by the electrolysis of water only

http://etd.uwc.ac.za/

account for about 4% of the worldwide total hydrogen production. An important reason for this is that the production of hydrogen and oxygen are affected by the cost and energy conversion efficiency.[5]

For water splitting, two processes are involved, described as a) the hydrogen evolution reaction (HER) at the cathode and b) the oxygen evolution reaction (OER) at the anode. In practical applications, electrocatalysts are required for both anode and cathode electrodes, because of the existence of overpotentials (the difference between the practical potential and the thermodynamic potential). Commonly, the electrocatalysts used for water splitting are mainly noble metals, and metal oxides, alloys, and hydroxides, such as Pt, Rh, RuO_2, Ru_2P, and IrO_2.[6,7] Although the noble metal electrocatalysts have excellent catalytic activity and stability for water splitting, their high price and scarcity limits their general usage.[8]

For PEMFCs, there are also two processes involved, described as a) the hydrogen oxidation reaction at the anode and b) the oxygen reduction reaction (ORR) at the cathode. Compared with hydrogen oxidation, the oxygen reduction process is much more difficult, which is the key step for the electrochemical reaction efficiency, and thus significantly affects the efficiency output of PEMFCs.[9,10] At present, the cathode electrocatalysts used in PEMFCs are mainly noble metal electrocatalysts mainly composed of platinum group metal (PGM) based metals, such as Pt, Pd and their alloys.[11] Presently, the Pt loading at the cathode is about 0.4 mg cm^{-2} while at the anode it is about 0.05 mg cm^{-2}, that means, a 100 KW fuel cell stack requires 100 g of platinum, and 0.5 billion fuel cell electric vehicles will require 150,000 tons of platinum. One has to consider that the world's Pt resources are expected to be in the range of 28,000 tons and thus will only be able to serve 20% of fuel cell electric

UNIVERSITY of the
WESTERN CAPE

http://etd.uwc.ac.za/

vehicles. Therefore, the development of efficient, stable and inexpensive electrocatalysts is essential for the large-scale water splitting and PEMFCs.

1.1 Introduction of PEMFCs

Fuel cell is an electrochemical device that converts chemical energy in fuels and oxidants directly into electrical energy. In 1839, William Grove produced hydrogen and oxygen by electrolyzing water and made the first fuel cell. Subsequently this type of fuel cell has been improved for nearly 180 years. As a new type of chemical power source, the fuel cell is known as the 4th generation power technology after hydropower, thermal power and nuclear power. Compared with thermal power generation, the fuel cell is environmental-friendly, not limited by the Carnot cycle, and generates no emissions (or extremely low) of CO, CO_2, SO_2, NO_x and unburned harmful substances.[12]

Fuel cells can be divided into five categories according to their electrolyte properties viz., a) alkaline fuel cells (AFCs), b) proton exchange membrane fuel cells (PEMFCs), c) phosphate fuel cells (PAFCs), d) molten carbonate fuel cells (MCFCs), and e) solid oxide fuel cells (SOFCs). Among them, PEMFCs use a sulfonic acid proton exchange membrane as a solid electrolyte. It has the characteristics of high energy conversion efficiency, being environmentally friendly, has a rapid start at room temperature, and a long life and high power density. It could be fixed in a power station, introduced in electric vehicles, and employed as special power supplies and mobile power supplies.

UNIVERSITY of the
WESTERN CAPE

http://etd.uwc.ac.za/

1.1.1 Principle of PEMFCs

The nature of PEMFCs is typified by the "reverse reaction" of water splitting, which is mainly composed of anode, cathode and proton exchange membrane, and the electrocatalysts on the electrode are used to accelerate the catalytic reactions (Fig 1.1).

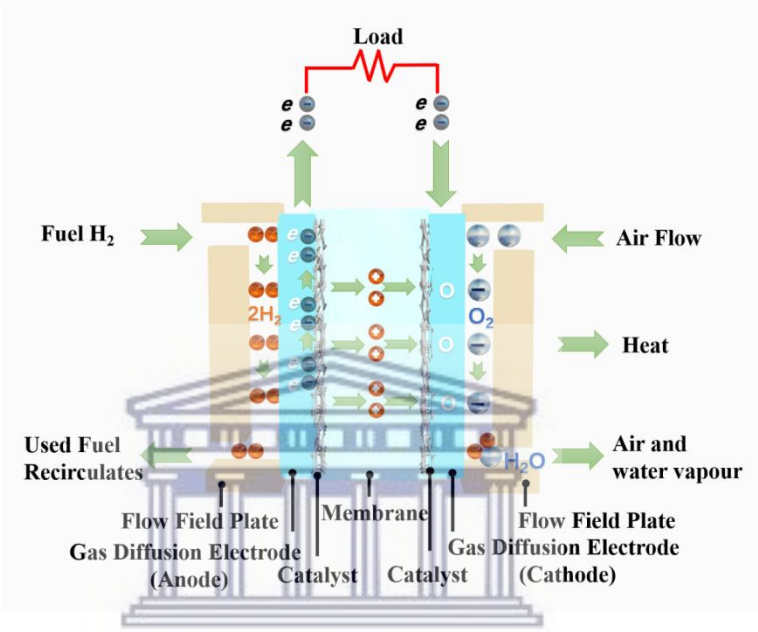

Figure 1.1 Principle of a PEMFCs.

UNIVERSITY of the
WESTERN CAPE

The working principle of PEMFC is as follows:

At the anode: H_2 reaches the anode through a pipe or a flow field plate. Under the action of the anode electrocatalyst, the hydrogen molecule oxidizes and dissociates into two protons, and releases two electrons. The anode electrode reaction is:

$$H_2 \rightarrow 2H^+ + 2e \qquad \phi_1^{\theta} = 0V$$

At the Cathode: oxygen (or air) reaches the cathode through a pipe or a flow field plate. Under the action of the cathode electrocatalyst, oxygen molecules react with hydrogen ions that pass through the proton exchange membrane, produce water and generate heat. The cathode electrode reaction is:

http://etd.uwc.ac.za/

$$1/2O_2 + H^+ + 2e \rightarrow H_2O \qquad \phi_2^\theta = 1.23V$$

The general chemical reaction equation is:

$$H_2 + 1/2O_2 \rightarrow H_2O \qquad E^\theta = \varphi_2^\theta - \varphi_1^\theta = 1.23\ V$$

At the same time, the electrons move from anode to cathode, and work through the load to produce electricity.

1.1.2 Components of PEMFCs

PEMFC single cell mainly include membrane electrodes, bipolar plates and current collectors. The membrane electrode assembly (MEA) is the core component of PEMFCs. It is a single component that combines an anode, a proton exchange membrane, and a cathode into a sandwich structure.

The MEA is usually composed of 5 layers: an anode diffusion layer, an anode electrocatalyst layer, a proton exchange membrane, a cathode electrocatalyst layer, and a cathode diffusion layer (Fig 1.2).

UNIVERSITY of the
WESTERN CAPE

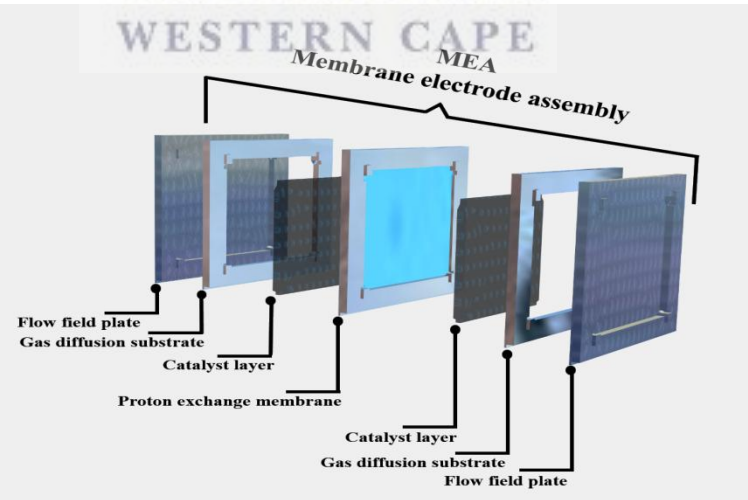

Figure 1.2 Principle of MEA.

http://etd.uwc.ac.za/

Among them, the electrocatalyst is one of the key materials and it is the site where the electrochemical reactions take place. Specifically, for the cathode electrocatalysts which suffer from high oxygen concentration and especially in the electrochemical environment, it is facile to be oxidized and thus reduce the catalytic activity or even totally negate activity for oxygen reaction.[13-16]

Generally, under certain conditions, in order to satisfy the power output and service life of PEMFCs, the minimum quantity of Pt used in the fuel cell is closely related to the activity and stability of the electrocatalyst. It is common knowledge that, the electrocatalysts combined with the metal particles and carriers, the latter also described as support materials, possess physical and chemical structures that could also affect interactions between the metal particles and the support materials. Consequently, significant corresponding catalytic activity and stability of the prepared electrocatalysts may be adversely or favorably affected.[17-22] Therefore, the development of electrocatalysts with low cost, high catalytic activity and stability is important for the commercialization of PEMFCs.

UNIVERSITY of the
WESTERN CAPE

1.2 Oxygen Reduction Reaction

Platinum is currently the most effective monometallic electrocatalyst for oxygen reduction and it is thus critical for PEMFCs. Platinum is mainly used at the cathode, accounting for about 90% of the total Pt consumption in PEMFCs. It is thus expected that the limited availability and ever-growing demand for Pt in the automotive industry will inevitably result in an increase in the price of Pt. Therefore, improving the activity and stability of the cathode electrocatalysts to reduce the amount of Pt is significant for the commercialization of PEMFCs. Furthermore, due to the slow kinetics reaction of oxygen reduction, which is the key step of the chemical reaction,

http://etd.uwc.ac.za/

this limits the output of powder, and further increases the importance of cathode electrocatalysts.[23]

In fact, only understanding of the principle of oxygen reduction process may not enough mainly due to the following reasons:

(1) Both in acidic and alkaline solutions, the ORR process is a multi-electron electrochemical reaction involving 4 electrons compared to the hydrogen oxidation reaction at the anode electrode which only has 2 electrons that participate, the ORR process is much more difficult and involves many complicated intermediate steps.

(2) The electrochemical window of the ORR process involves a region with a positive potential, especially in an acidic electrolyte, and the surface of the electrode is covered by adsorbed oxygen or oxygen-containing species, and even forms oxides. What is more, the physical surface states of such oxide layer changes constantly with the potential and thus makes any investigation into the mechanism for oxygen reduction an extremely difficult and arduous one.[17]

1.2.1 Principle of Oxygen Reduction Reaction

UNIVERSITY of the
WESTERN CAPE

The oxygen reduction reaction is a complicated process, although many theoretical and experimental investigations have been undertaken,[24,25] the mechanism remains unclear.

Generally, it is accepted that oxygen reduction mainly follows two paths ways: a) a direct four-electron process, in which the oxygen is directly converted into water under the catalytic action of electrocatalyst, b) a two-electron process, in which oxygen is converted to H_2O_2 and then further into water (Fig 1.3).

http://etd.uwc.ac.za/

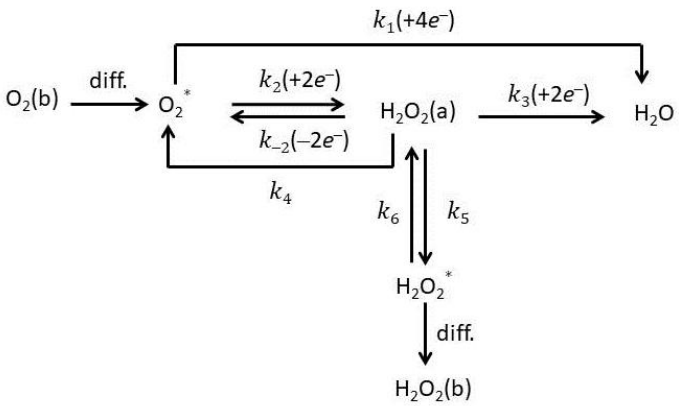

Figure 1.3 The mechanisms of oxygen reduction reaction.

For example, for PEMFCs, in acid media, the main steps involved in the conversion of oxygen into water by a direct four-electron reaction are as follows:

$$O_2 + * \rightarrow O_2 *$$

$$O_2 * + * \rightarrow 2O*$$

$$2O* + 4H^+ + 2e^- \rightarrow 2OH*$$

$$2OH* + 2H^+ + 2e^- \rightarrow 2* + H_2O$$

UNIVERSITY of the
WESTERN CAPE

or

$$O_2 + * \rightarrow O_2 *$$

$$O_2 * + H^+ \rightarrow OOH*$$

$$OOH* + * + e^- \rightarrow O* + OH*$$

$$O* + H^+ + e^- \rightarrow OH*$$

$$2OH* + 2H^+ + 2e^- \rightarrow 2H_2O + 2*$$

http://etd.uwc.ac.za/

In acidic medium, the reaction steps for conversion of oxygen by direct 2 electron process into hydrogen peroxide are mainly as follows:

$$O_2 + * \rightarrow O_2 *$$

$$O_2 * + H^+ \rightarrow OOH *$$

$$OOH * + H^+ \rightarrow H_2O_2 *$$

$$H_2O_2 * + * \rightarrow 2OH *$$

$$2OH * + 2H^+ \rightarrow 2H_2O + 2 *$$

Theoretical and experimental studies found that ORR has a higher efficiency since it involves a direct 4 electron process, which could also avoid the influence of H_2O_2 on proton exchange membrane produced by indirect two-electron process, which is also harmful to the MEA, including the proton exchange membrane, gas diffusion layer, and the electrocatalyst.[26] Therefore, the four-electronic process is considered to be a most efficient reaction for ORR, and thus catalytic materials that favor 4 electron processes should be selected.

UNIVERSITY of the
WESTERN CAPE

According to the Sabatier principle,[27] if the electrocatalyst is strongly combined with oxygen, the rate-limiting step of ORR is the removal of the oxides or anions from the electrocatalysts' surface. Conversely, if the binding to oxygen is too weak, the rate-limiting step of ORR is the removal of oxides or anions that absorbed on the surface of electrocatalysts. In other words, the rate-limiting step of ORR is the transfer of electrons and protons to the oxygen adsorbed on the electrocatalysts' surface. Thus, a good ORR electrocatalyst should have a moderate oxygen binding energy that favors oxygen absorption and desorption (Figs 1.4 and 1.5)[28, 29]

http://etd.uwc.ac.za/

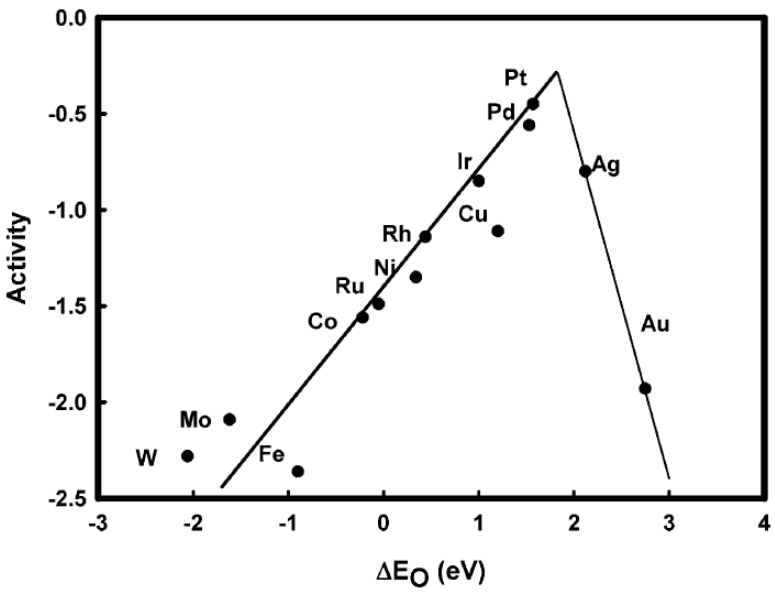

Figure 1.4 Trends in oxygen reduction activity plotted as a function of the oxygen binding energy.[27]

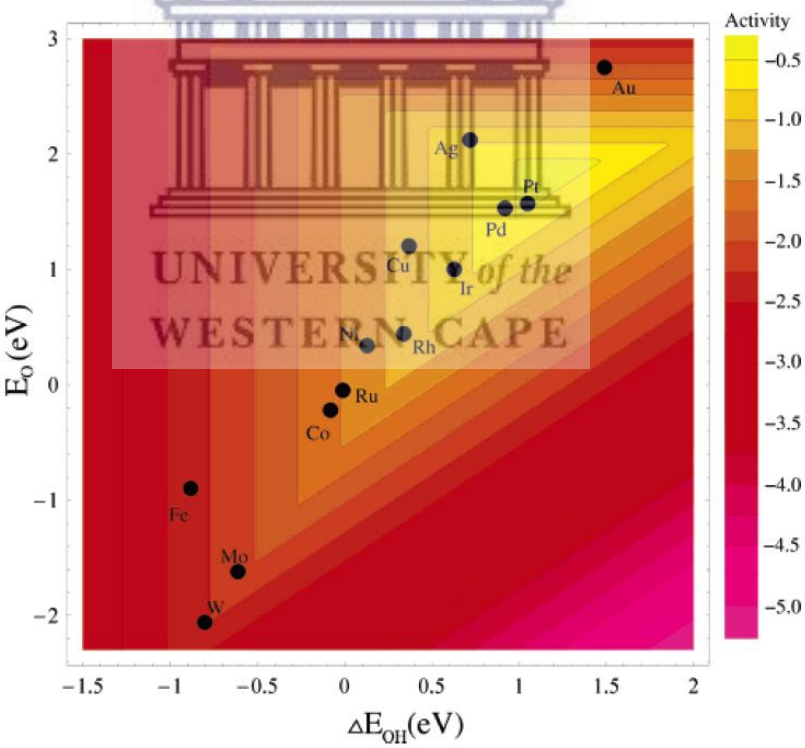

Figure 1.5 Trends in oxygen reduction activity plotted as a function of both the O and the OH binding energy.[27]

http://etd.uwc.ac.za/

1.2.2 Development of ORR Electrocatalysts

Platinum group metal (PGM) based materials are the most important electrocatalysts for ORR due to their superior catalytic properties. While, their scarcity and high cost mitigate against their continued usage, there is a great need to improve their utilization and reduce the dosage. One such development has been in the area of Pt nanoparticles being highly dispersed on carbon supports with high specific surface area, such as XC-72, CNTs, and graphene.[30-36] However even such highly dispersed electrocatalysts still suffer from in-sufficient activity and poor stability under the PEMFCs operating conditions.[35]

Generally, the electrochemically active surface area (ESCAs) and the catalytic active sites of Pt gradually decrease during the harsh working process, which is mainly due to the following reasons:[37-39]

(1) Migration and agglomeration of Pt particles. Since the surface energy of Pt nanoparticles is high and unstable, it is facile for these particles to migrate and agglomerate with each other. Meanwhile, there is a huge difference in the electronic structure between the metal Pt and the carbon support with their weak interactions making the metal particles relatively easy to move and agglomerate on the surface of the carrier.

(2) Dissolution and re-deposition of Pt particles. The Pt particles will inevitably be oxidized during the long-term operation, resulting in dissolution, and the Pt ions thus being dissolved at high potential will be deposited again on other Pt nanoparticles at a lower potential during the potential cycles, thus changing the morphology and structure of the entire electrocatalyst surface, and decrease the corresponding catalytic activity of the catalytic materials.

UNIVERSITY of the WESTERN CAPE
http://etd.uwc.ac.za/

(3) Poisoning of Pt particles. If air is used instead of pure oxygen as fuel for PEMFCs, it usually contains traces of SO_X, NO_X and hydrocarbons, which are easily adsorbed on the surface of the electrocatalyst, covering the active site of Pt, and thus poisoning the platinum-based catalytic materials.

(4) Corrosion of carbon supports. Commonly, the electrocatalyst support is amorphous carbon with a high specific surface area, and its surface contains a large number of defects and unsaturated bonds. At a low potential, about 0.207 V (*vs*. NHE), an intermediate oxide is formed on the surface of the carbon support. At high potentials (0.6~0.9 V *vs*. NHE) and in the presence of water, new defect sites will be formed, which will increase the content of surface oxygen functional groups such as -COOH and -OH and thus increase the hydrophilicity and impedance of the electrode, increase the gas transfer resistance, reduce the diffusion efficiency and consequently decline the performance of the electrode.

Therefore, optimizing the structure, morphology and composition of the Pt-based electrocatalyst to ensure maximum platinum activity and stability is significant for the development of PEMFCs.

UNIVERSITY of the
WESTERN CAPE

In recent decades, great achievements were achieved for ORR electrocatalysts. Generally, these improvements can be divided into several parts, low-Pt electrocatalysts, non-PGM based electrocatalysts, and metal-free electrocatalysts to name just a few.

Low-Pt electrocatalysts, alloy electrocatalysts, single-layer electrocatalysts, morphology-controllable alloy electrocatalysts, nano-film Pt-based electrocatalysts, monoatomic electrocatalysts, core-shell electrocatalysts, high crystal surface index framework electrocatalysts have been widely reported.[30, 40-42]

http://etd.uwc.ac.za/

Non-PGM based electrocatalysts, such as Fe-N-C, Co-N-C, Ni-N-C have been intensively studied, which also display interesting properties for oxygen reduction. Some electrocatalysts even displayed Pt-like catalytic activity for oxygen reduction, but it is still cannot be used for practical applications.[43-45]

For metal-free electrocatalysts, mainly carbon based materials doped by heterogeneous atoms, such as nitrogen, phosphorus, sulfur, and boron is a hot point for the development of electrocatalysts for oxygen reduction.[46-50]

In addition, researchers are also passionate to develop new nanostructured carbon supports and non-carbon carriers which are expected to enhance the activity and stability of the electrocatalyst by virtue of the positive interaction and the synergistic catalytic effect between the support and the active materials.[51,52]

Although the commercialization of Pt-based ORR electrocatalysts has accelerated in recent years, development of high-efficiency and low-Pt electrocatalysts is still the most practical way to achieve large-scale commercialization of PEMFCs. However, from the perspective of long-term development of new energy hydrogen-powered fuel vehicles and the limited platinum resources, development of highly active, non-precious metal electrocatalysts that completely replace Pt are more imperative.

Fortunately, in the past two decades, with the rapid development of materials science and nanotechnology, by regulating the chemical and/or physical properties of the electrocatalyst at the molecular or atomic levels (such as DFT simulation calculation)[28, 53], combined with advanced in situ characterization techniques, such as environmental spherical aberration transmission electron microscope (E-TEM),[54] high temperature XRD, in-situ Raman, in-situ electrochemical characterizations, large numbers of new concepts and new syntheses of ORR electrocatalysts and their corresponding ORR catalytic mechanism have been

UNIVERSITY of the
WESTERN CAPE
http://etd.uwc.ac.za/

proposed.[53] At the same time, some significant progress has been made in the rational design and preparation of highly efficient ORR electrocatalysts (Fig 1.6).

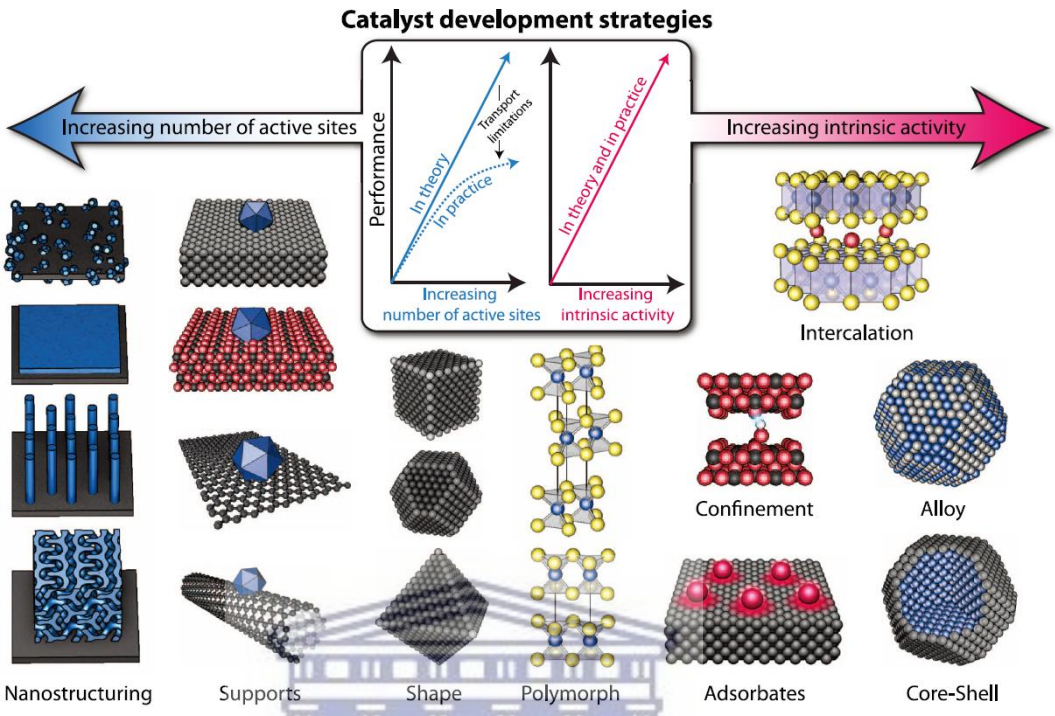

Figure 1.6 Schematic of various electrocatalyst development strategies, which aim to increase the number of active sites and/or increase the intrinsic activity of each active site.[53]

1.3 Introduction of Water Splitting

UNIVERSITY of the
WESTERN CAPE

Hydrogen energy is a secondary energy source produced by using other energy sources. At present, hydrogen energy is mostly obtained by fossil fuels. While, with the adjustment of the world's energy structure, the use of renewable energy to produce hydrogen is an idea choice of mankind.

The United Nations has predicted that in 2050, 40% of global energy and 60% of electricity will be provided by renewable energy. However, the development and utilization of renewable energy is affected by its intermittent and unpredictable nature, leading to serious energy waste and thus restricting its development. Hydrogen energy is an excellent energy carrier, which could be produced by

http://etd.uwc.ac.za/

electrolysis of water from renewable energy, such as solar energy, wind energy, water energy, ocean energy and geothermal energy (Fig 1.7).[55-57]

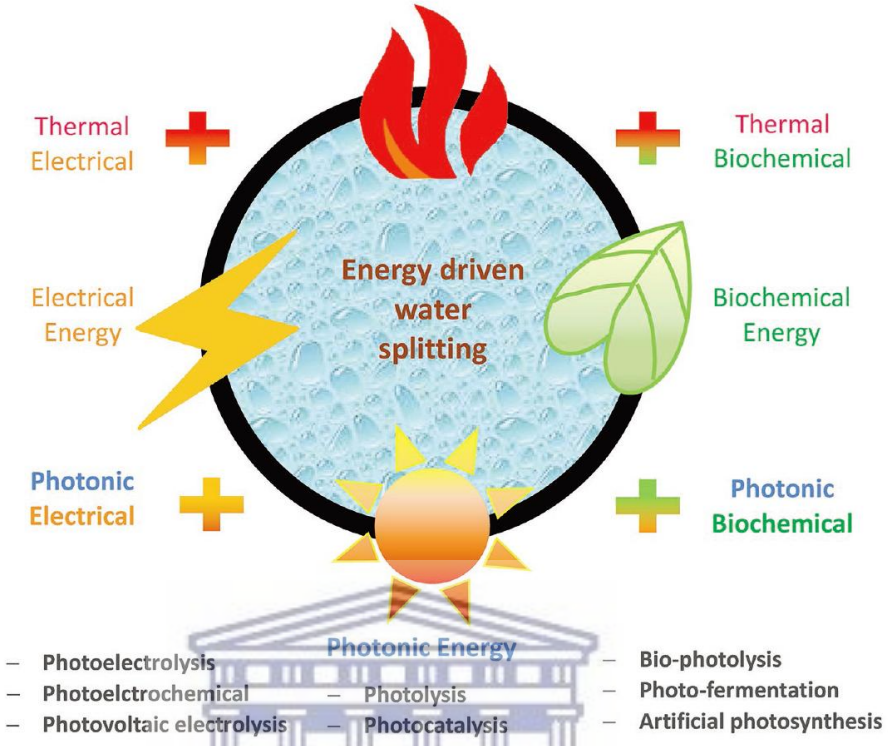

Figure 1.7 Various energy driven water splitting routes by using thermal, electrical, biochemical and photonic energy or their combinations.[56]

Water splitting could increase the usage and utilize efficiency of renewable energy by hydrogen production and thus alleviate the global energy crisis. Hydrogen energy is an ideal renewable energy source, and its advantages may be ascribed to the following: 1) Hydrogen may be stored not only in its pure form but in the form of compounds, and is widely distributed in nature. 2) It has the highest energy density, 1 mole H_2 could produce 286 KJ of heat, and the heat that is produced by hydrogen combustion is three times higher than the same mass of oil. 3) It is clean and environmentally-friendly, and the only by-product is pure water. 4) It has a variety of different forms of utilization. It can be used directly to generate heat energy by combustion, or as an energy source for engines or fuel cells. 5) As a raw material for

http://etd.uwc.ac.za/

the clean utilization of fossil fuels, such as oil and coal-based energy, which has a huge demand of hydrogen and used for hydrogenation processes.

The realization of hydrogen energy has three requirements: a) hydrogen production, b) storage and c) utilization. Among them, large-scale and inexpensive industrial hydrogen production is our primary concern. At present, there are many methods for preparing hydrogen. The most important industrial method is the use of fossil energy to produce hydrogen, followed by a variety of chemical processes such as the chlor-alkali industry, fermentation industry, synthetic ammonia industry, and refining industry, all of which generate a large amount of by-products.

Compared with the above mentioned methods, electrolysis of water offers an alternative promising method to produce hydrogen with high purity, which could use electricity produced by some renewable energy source. Compared to natural gas, petroleum and other fossil fuels used for hydrogen production, there are still many challenges in preparing hydrogen from renewable energy sources, the most important being reduction of costs.

UNIVERSITY of the
WESTERN CAPE

1.3.1 Electrolytic Water Devices

Water splitting is the process of using electricity to electrolyze water to produce hydrogen and oxygen. The purity of hydrogen obtained by water splitting is as high as 99.99%. To date, it is one of the most effective methods for producing hydrogen.

Electrolyzed water is mainly divided into three types: the alkaline electrolyzer, the proton exchange membrane (PEM) electrolyzer, and the solid-oxide electrolyzer (SOE) to produce hydrogen, among them, the first two are widely used in industry.

(1) The alkaline electrolyzer is the earliest method to produce hydrogen; the efficiency is about 65-80%, which is the lowest among the three types of electrolytic

http://etd.uwc.ac.za/

cells. It consists of a numbers of single cells, each of which consists of a cathode, an anode, a separator and an electrolyte. The principle of the alkaline electrolyzer (Fig 1.8) is shown as below.

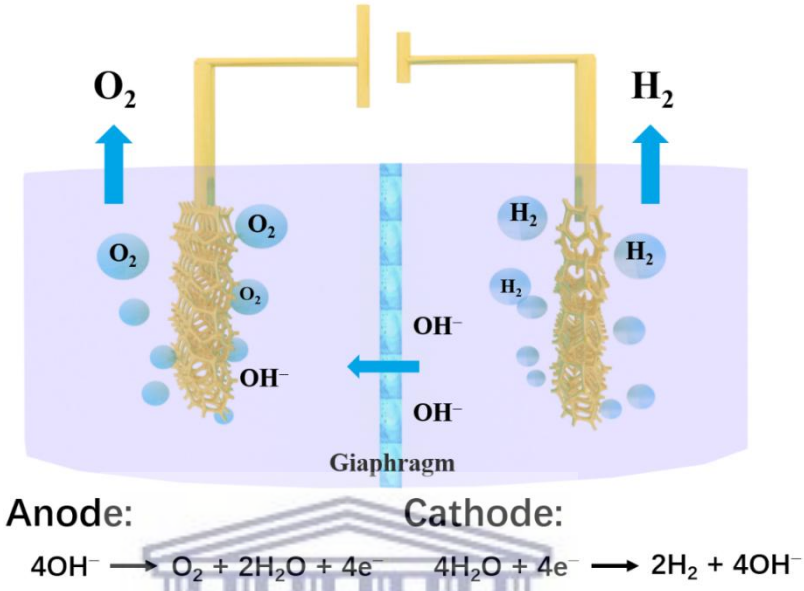

Figure 1.8 The principle of alkaline electrolyte water electrolysis.

The electrolyte is usually a sodium hydroxide or potassium hydroxide solution, a nickel-cobalt-iron composite material is used as an anode, a nickel-based material is used as a cathode, and asbestos as a separator. Water molecules on the surface of the cathode get electrons to form hydrogen and hydroxide ions (OH^-), after which the OH^- passes through the membrane to the anode, where electrons are lost on the surface of the anode to generate oxygen and water molecules.

The key issue for the alkaline electrolyzer is the high energy consumption. The actual decomposition voltage is generally between 1.8 and 2.6 V, and the electricity consumption per cubic meter of H_2 is about 4.5 to 5.5 kW·h.[58] In fact, the water molecules on the surface of the cathode receive electrons to form hydrogen and OH^- which is the rate determining step. Therefore, improving the dissociation of water

UNIVERSITY of the
WESTERN CAPE

http://etd.uwc.ac.za/

molecules and rapidly forming hydrogen intermediates are fundamental problems in solving the problem of energy consumption.[59]

(2) The PEM water electrolyzer is mainly an integrated structure consisting of two electrodes and a proton exchange membrane, usually a Nafion membrane as proton exchange membrane, with electrocatalytic powders (electrocatalysts) being adhered on both sides of the membrane (Fig 1.9).

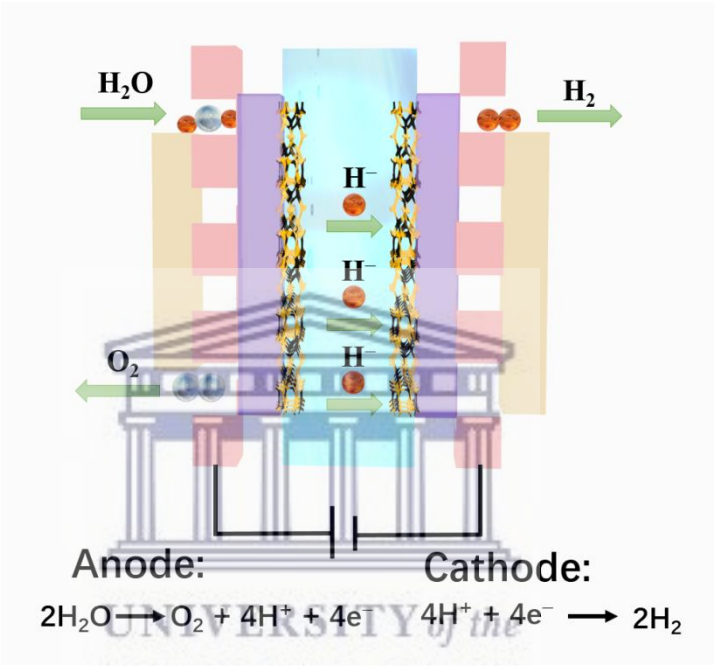

UNIVERSITY of the
WESTERN CAPE

Figure 1.9 Principle of proton exchange membrane water electrolyzer.

The principle of the PEM water electrolyzer is illustrated as follows: Pure water enters the system through the anode, and the electrons are oxidized at the anode to generate O_2 and H^+. The proton diffuses through the proton exchange membrane to the surface of the cathode to obtain an electron and been reduced to form H_2. The proton conduction in the proton exchange membrane is achieved by the transfer of H^+ from a sulfonic acid group to another one in the form of OH^-. The efficiency of the PEM water electrolyzer is >85% and also has a higher working current density (generally 0.6~2.0 A cm^2), thus it has greater capacity for hydrogen production.

http://etd.uwc.ac.za/

Since the Nafion membrane is strongly acidic in water, the PEM electrolyzer actually works in an acidic environment. Thus, its electrode material needs to work in an environment that satisfies an acidic medium and a high working current for a long time. That means, the development of an electrocatalyst with low-cost and high efficiency that could be used to replace precious metals is highly significant for the commercialization of the PEM water electrolyzer.

(3) Solid oxide water electrolysis is a technology using Y_2O_3 stabilized ZrO_2 as electrolyte and electrolysis of water vapor at high temperature (600~1000 ^oC).[60] Generally, a mixed sintered product of nickel and ceramic is used as a cathode, and a calcium-titanium composite oxide is used as an anode (Fig 1.10).

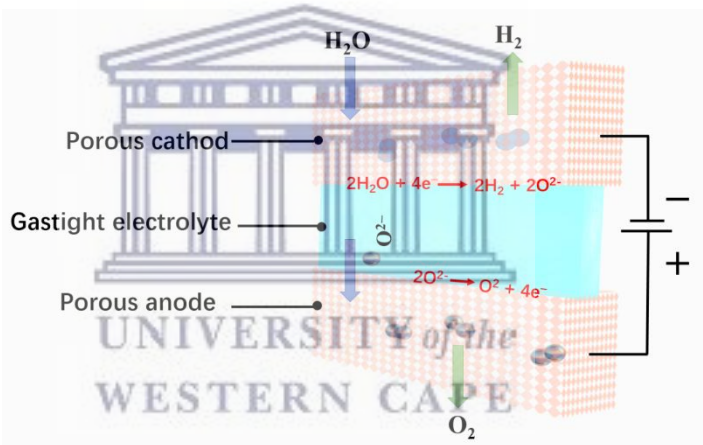

Figure 1.10 Principle of solid oxide water electrolyzer.

The advantage of the SOE electrolyzer is that it can directly utilize the thermal energy of high-temperature heat sources (such as nuclear energy, geothermal heat, and other heat sources) and thus improve the energy utilization efficiency. However, the cost of such an electrolyzer is so high that further investigations are needed to decrease the high cost for hydrogen production.

http://etd.uwc.ac.za/

1.3.2 Basic Mechanisms for Water Splitting

Generally, the water electrolyzer consists of four components: a) the electrolyte, b) the cathode, c) the anode and d) the power supply, in which the cathode obtains electrons from the external power supply for HER and the anode simultaneously loses electrons for OER. In fact, it is difficult to electrolyse water at 1.23 V (thermodynamic voltage at 25 ^{o}C and 1.0 atm) due to the intrinsic activation barriers of both electrodes and the resistances of the solution and contact points.[5]

However, the solution and contact resistances can be reduced by optimizing the design of electrolytic cells. In addition, the water splitting voltage can be reduced by coating electrocatalysts onto the both electrodes to reduce the intrinsic barriers for water splitting. Based on different electrolytes, water splitting can be expressed in different forms:

In acidic solutions

Cathode $2H^{+} + 2e^{-} \rightarrow H_2$

Anode $H_2O - 2e^{-} \rightarrow 2H^{+} + \frac{1}{2}O_2$

UNIVERSITY of the
WESTERN CAPE

In neutral and alkaline solutions

Cathode $2H_2O + 2e^{-} \rightarrow 2OH^{-} + H_2$

Anode $2OH^{-} - 2e^{-} \rightarrow H_2O + \frac{1}{2}O_2$

As noted from the half-reaction of water splitting, hydrogen evolution involves two mechanisms with three possible reaction steps in acidic electrolyte, in which the dominant reaction mechanism of the HER process can be determined by the Tafel slope from experimental data.[61-63] Generally, under acidic conditions in the first reaction step, the proton in the electrolyte receives an electron and subsequently

http://etd.uwc.ac.za/

forms an absorbed hydrogen atom (H_{ads}) on the active site of the electrocatalyst, which is usually called as the Volmer reaction.

$$H^+ + e^- \rightarrow H_{ads} \text{ (Volmer)}$$

$$b_1 = \frac{2.3RT}{\alpha F}$$

In this equation b is the Tafel slope, R is the ideal gas constant, T is the absolute temperature, α is the symmetry coefficient with a value of 0.5, and F is the Faraday constant.

The following desorption process has two different pathways to produce hydrogen. In the one, since the H_{ads} coverage is relatively low, it prefers to react with a H^+ and electron to generate H_2. This process is electrochemical desorption and named as the Heyrovsky reaction.

$$H_{ads} + H^+ + e^- \rightarrow H_2 \text{ (Heyrovsky)}$$

$$b_2 = \frac{2.3RT}{(1+\alpha)F}$$

UNIVERSITY of the
WESTERN CAPE

However, in the other process, an increasing H_{ads} coverage leads to a change of the dominant desorption process from the above electrochemical desorption to recombination between the adjacent H_{ads}, which is a Tafel reaction and it is also a chemical desorption process.

$$H_{ads} + H_{ads} \rightarrow H_2 \text{ (Tafel)}$$

$$b_3 = \frac{2.3RT}{2F}$$

At 25 ^{o}C, the calculated Tafel slopes of the above three reactions are 116, 38, and 29 mV dec^{-1} for b_1, b_2 and b_3, respectively. Unlike in the acid condition, the H_{ads} in alkaline solution comes from the electrochemical reduction of H_2O, which is more

http://etd.uwc.ac.za/

sluggish than the reduction of H^+ in acid solution because the H–O–H bond needs to be broken before absorbing hydrogen.[64] Therefore, it is more facile to evolve hydrogen in acid solution than in alkaline solution. However, most of the electrocatalysts are unstable in acid solution due to their poor corrosion resistance, especially among non-noble metals. Therefore, in order to enhance the stability of hydrogen evolution electrocatalysts, some strategies such as metal hybrids or carbon-coated structures have been developed.[4,65]

1.3.3 Evaluation the Activity of HER Electrocatalysts

To evaluate the performances of HER electrocatalysts, some crucial experimental and theoretical parameters, such as onset potential, overpotential, Tafel slope, exchange current density, stability, impedance and hydrogen bonding energy should be measured or calculated.

(1) Onset potential and overpotential.

The onset potential and overpotential at a certain current density (10 mA cm^{-2}) are used to compare the activities between different electrocatalysts. While, in fact, is difficult to get a precise value of the onset potential due to the high surface areas of electrocatalysts inevitably cause the capacitive current during the electrochemical test. Usually, a relatively low sweep rate, such as 2 or 5 mV s^{-1}, is set to reduce the capacitive current in linear sweep voltammetry. The overpotential at current density of –0.5 to –2 mA cm^{-2} is usually recognized as the onset potential in some papers. In addition, the overpotential at current density of –10 mA cm^{-2} is regarded as an important reference to compare the catalytic activities for different electrocatalysts, which is the current density expected for a 12.3% efficient solar water-splitting

UNIVERSITY of the
WESTERN CAPE

http://etd.uwc.ac.za/

device.[5] Generally, the lower the overpotential it means the better the HER activity of the electrocatalyst will be.

In practical measurement, the overpotential can be mainly divided into activity overpotential, concentration overpotential, and resistance overpotential. In order to eliminate the influence of these resistances, *iR* compensation is used to get accurate overpotential of electrocatalysts at a certain current density. Here, the value of *R* is the real part of the Nyquist curve at high frequencies.

(2) Tafel slope and exchange current density.

In electrochemical kinetics, the reaction rate mainly depends on overpotential, and the relationship can be expressed by the Butler–Volmer equation.[66]

$$j = j_0 (e^{(1-\alpha)\eta F/RT} - e^{-\alpha\eta F/RT})$$

where j is the current density, j_0 is the exchange current density, and η is the overpotential. When η is higher than 50 mV, the equation can be simplified to the Tafel equation.[67]

$$\eta = a + b \log j$$

UNIVERSITY of the
WESTERN CAPE

From this equation, two important parameters (b and j_0, which is j when η equals to zero) can be obtained. According to the value of b, the dominant reaction mechanism of the HER process can be revealed. When b is ~ 29 mV dec^{-1}, it means the first step, the adsorption of hydrogen is fast and chemical desorption process is the rate determining step. When b is ~ 38 mV dec^{-1}, it indicates that the adsorption of hydrogen is fast. However, the hydrogen desorption rate is relatively slow and therefore H_2 is evolved by the rate determining step, namely the electrochemical desorption reaction. When b is ~ 116 mV dec^{-1}, the first step is slow, regardless of

http://etd.uwc.ac.za/

whether hydrogen is generated by the electrochemical desorption reaction or chemical desorption reaction.

Another important parameter to evaluate the intrinsic activity of electrocatalysts is j_0. It describes the electrochemical reaction rate under reversible conditions. A small b and large j_0 are desirable for an ideal electrocatalyst for hydrogen evolution.

(3) Hydrogen bonding energy.

From these two reaction mechanisms of hydrogen evolution, it is clearly that the hydrogen absorption/desorption process are the key steps for water splitting. Therefore, to a certain extent, the hydrogen bonding strength on an electrocatalyst surface can be used to determine and predict the intrinsic activity for hydrogen evolution.

Specifically, a weak bonding strength between the active sites and hydrogen atoms will favor desorption of hydrogen, but it slows the absorption of hydrogen in the first step. A strong bonding strength between them will be facile for hydrogen absorption, while it has difficulty in releasing the produced hydrogen in the second or third step. Accordingly, an ideal electrocatalyst should have a moderate hydrogen bonding strength.[53,68,69]

In 1958, Parson firstly pointed out the relationship between the Gibbs free energy of hydrogen adsorption value (ΔG_{H^*}) and j_0.[70] A famous volcano-shaped curve, calculated ΔG_{H^*} on different transition metals as X axis and experimental j_0 as Y axis, was plotted by Norskov and co-workers (Fig 1.11).[69] It indicates that ΔG_{H^*} is a good descriptor for HER activity, an optimal HER electrocatalyst has the ΔG_{H^*} close to zero. Therefore, it is useful to optimize the catalytic activity to modify the ΔG_{H^*} by changing the compositions and structures.

UNIVERSITY of the
WESTERN CAPE
http://etd.uwc.ac.za/

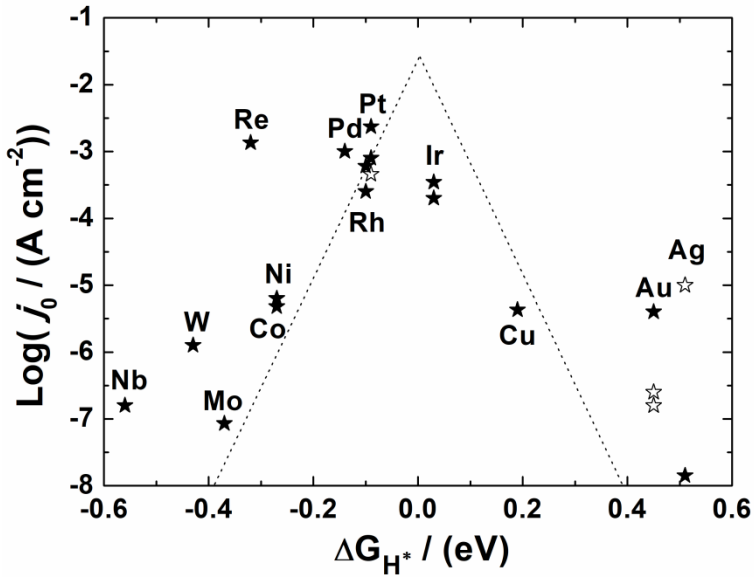

Figure 1.11 A volcano plot of experimentally measured exchange current density as a function of the DFT-calculated Gibbs free energy of hydrogen adsorption on pure metals.[69]

1.3.4 Development of HER Electrocatalysts

The HER electrocatalysts are generally used to reduce the activation energy for water splitting, thereby reducing the overpotential and energy consumption. The catalytic activity and stability of the electrocatalyst will determine the total voltage required and the conversion efficiency for water splitting. Therefore, it is significant to develop new electrocatalysts with high catalytic activity to increase the energy conversion efficiency for water splitting.[71]

In an acidic environment, Pt is an ideal electrocatalyst for the hydrogen evolution reaction. The overpotential is close to zero and the Tafel slope is also small.[72-75] Due to the high price and scarcity of the current electrocatalysts, it is necessary to develop other alternatives with high performance and low-cost catalytic materials, such as transition metal sulfides,[76] carbides[71,77] and phosphides,[78] nitrides,[79] and selenides,[80,81]. On the other hand, IrO_2 is a good electrocatalyst for the oxygen evolution reaction.[82] However, due to the harsh requirements of

UNIVERSITY of the WESTERN CAPE
http://etd.uwc.ac.za/

catalytic materials under the acidic environment and high potential conditions, it is very difficult for the electrocatalyst to exhibit high oxygen evolution catalytic activity and stability at the same time. No anode electrocatalyst has been found to date that could completely replace the precious metal.

In alkaline environments, precious metals and their oxides are still excellent electrocatalysts, but due to the stability of the oxides in alkaline environments, there are more choices of transition metal compounds. It has been found that, in an alkaline solution, the overpotential is generated in the hydrogen evolution process, because the hydrogen atoms need to be adsorbed on the surface of metals and the rate for formation of hydrogen intermediate is slow, in the process of water splitting.

At present, there are mainly three types of elements constituting the hydrogen evolution electrocatalysts: (1) The noble metals (such as Pt, Ir, Ru, Rh) currently being the most active HER electrocatalysts although easily being inactivated by poisoning. These metals also suffer from their scarcity and high price thus mitigating their use on large scale; (2) The transition metal elements: Fe, Co, Ni, Cu, Mo, W, Mn, and V, which are commonly used to form a non-precious metal electrocatalysts for hydrogen evolution; (3) Non-metallic elements: B, C, N, P, S, and Se, which are commonly used as doping elements to form non-precious metal electrocatalysts for hydrogen evolution.

At present, some effective non-precious metal electrocatalysts for HER have been synthesized. The presence of these transition metal elements increases sequentially: W = Mo < Co < Cu < Ni < Fe. However, the cost is inversely proportional to the presence in the earth, and the larger the availability, the lower the price. Therefore, in the past decade, a large number of studies have been carried out on these transition metals, to develop heterogeneous electrocatalysts or synthesize defective structure

UNIVERSITY of the
WESTERN CAPE
http://etd.uwc.ac.za/

electrocatalysts,[83-85] in the hope of finding an ideal HER electrocatalyst to replace precious metals (Figs 1.12 and 1.13).

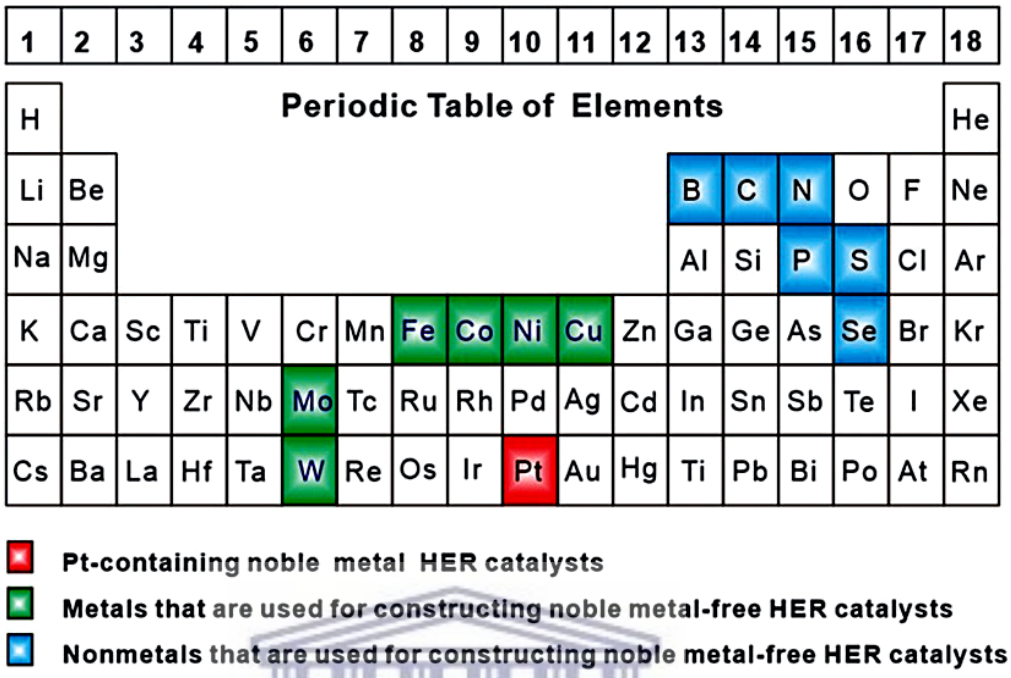

Figure 1.12 Elements that are used for constructing HER electrocatalysts.[86]

UNIVERSITY of the
WESTERN CAPE

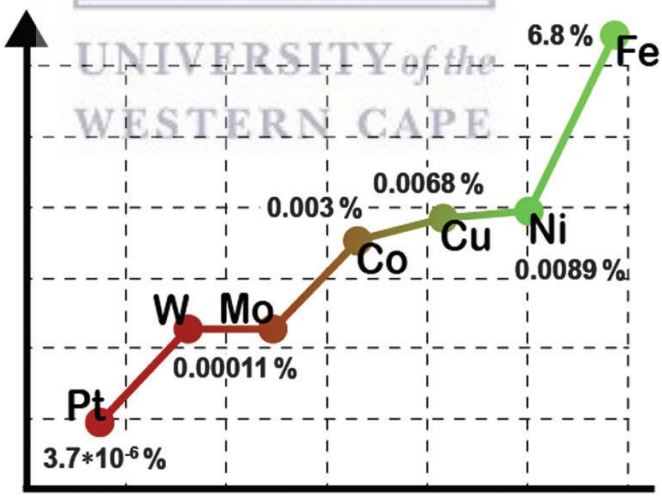

Figure 1.13 Crustal abundance of metals that are used for constructing HER electrocatalysts.[86]

http://etd.uwc.ac.za/

1.4 Significance and Novelty of this work

1.4.1 Significance

For ORR electrocatalysts, the relatively low efficiency for oxygen reduction is the main obstacle for the commercialization of PEMFCs resulting in numerous studies over the last decade. Due to the slow kinetics of oxygen reduction, Pt is currently the most effective monometallic electrocatalyst for ORR and it is thus essential for hydrogen-feed PEMFCs. The limited abundance and ever-growing demand for Pt in automotive industry will inevitably increase its price. Although tremendous investigations to address this issue have been made, further reduction of costs through the synthesis of new electrocatalysts with high performance at a lower price remains a serious challenge.

For water splitting, the theoretical voltage is 1.23 V, but the actual working voltage is often as high as 1.8 to 2.6 V. The electrode material has an important influence on the reaction mechanism of the electrode and the reaction rate. Therefore, production and maintenance of an electrolyzer, especially for improving the efficiency of energy conversion and reducing the cost is an imperative.

For hydrogen evolution electrocatalysis in acidic medium, one should firstly select a catalytic material with a potential hydrogen evolution activity (transition metal or non-metal) to confirm the inherent active sites. Subsequently, one needs to optimize the composition ratios, construct a stable structure that exerts its activity most efficiently, and maximize the exposure of active sites. Finally, regulation of the morphology of the electrocatalyst will lead to improving the conductivity and the channel for gas diffusion. The efficient transmission of electrons and the facile

UNIVERSITY of the
WESTERN CAPE

http://etd.uwc.ac.za/

diffusion of gas are also important for reducing the overpotential and increasing the activity for hydrogen evolution.

However, in an alkaline medium, hydrogen evolution at the cathode is due to the charge-induced water molecule dissociation into active hydrogen atoms, which is then adsorbed on the surface of the electrocatalyst and subsequent desorbed to form hydrogen molecules. In acidic medium, the protons are transferred to the cathode to receive electrons adsorbed to the surface of the electrode, and then desorbed to form hydrogen molecules. In alkaline media, the dissociation of water molecules is usually a rate determining step that requires more energy. This is also the reason for the HER efficiency being lower in alkaline media than in acidic media.

Therefore, for HER electrocatalyst, one should consider the ability for absorption and/or desorption of the active hydrogen atoms, and the dissociation efficiency of water molecules. This could be realized by adjusting the composition, structure, morphology and other factors of the electrocatalyst. An ideal electrocatalyst should be beneficial to the dissociation of water molecules and also be facile to the absorption and/or desorption of hydrogen atoms, which are significant to improve the efficiency for water splitting.

UNIVERSITY of the
WESTERN CAPE

1.4.2 Novelty

In this thesis, a new exploration of electrocatalysts for oxygen reduction and hydrogen evolution were carried out with good activity and stability.

(1) PtNiMo ternary alloy electrocatalysts with different atomic ratios were prepared, which demonstrated an alloy structure and high ORR activity in an O_2-saturated 0.1 mol L^{-1} $HClO_4$ aqueous solution. Pt_3Ni_3MoN/C has the highest mass activity of 539.41 mA mg^{-1} Pt, which is 3.49 times higher than that of the

http://etd.uwc.ac.za/

commercial Pt/C (154.46 mA mg^{-1} Pt) and also exhibits excellent stability during the accelerated durability tests. The corresponding mechanism is discussed.

(2) Self-supported S, P co-doped Cu nanowire (Cu_2S-Cu_3P NW) arrays on commercial copper foam were prepared. These acted as HER electrocatalysts in KOH electrolyte, and only required a low overpotential of 150 mV to achieve a current density of 10 mA cm^{-2} and displayed a small Tafel slope of 45 mV dec^{-1}. The activity decrease is ignorable after holding at –20 mA cm^{-2} for 90 h which thus demonstrates excellent stability. This could be due to the nanowire arrays structure and co-doping effects of S and P, which could increase the specific surface area, reduce the charge transfer resistance, facile for mass and electron transfers, and increase the active sites.

(3) Ni-Co-P/NF electrocatalysts are synthesized through two steps, which exhibit remarkably catalytic performance for HER compared to other as-prepared electrocatalysts. It was found that they ensure a large current density of –300 and –1,500 mA cm^{-2} that require small over potentials of –300 and –400 mV, respectively, Tafel slopes of 53 mV dec^{-1}, and also exhibiting excellent stability for HER.

UNIVERSITY of the
WESTERN CAPE

http://etd.uwc.ac.za/

1.5 References

1. Kulkarni A, Siahrostami S, Patel A, Norskov JK. Understanding catalytic activity trends in the oxygen reduction reaction. *Chem. Rev.*, 2018, 118(5), 2302-2312.
2. Yang L, Shui J, Du L, Shao Y, Liu J, Dai L, Hu Z. Carbon-based metal-free ORR electrocatalysts for fuel cells: past, present, and future. *Adv. Mater.*, 2019, 31(13).
3. Xu H, Cheng D, Cao D, Zeng XC. A universal principle for a rational design of single-atom electrocatalysts. *Nature Catal.*, 2018, 1(5), 339-348.
4. Jing S, Lu J, Yu G, Yin S, Luo L, Zhang Z, Ma Y, Chen W, Shen PK. Carbon-encapsulated WO_x hybrids as efficient catalysts for hydrogen evolution. *Adv. Mater.*, 2018, 30(28).
5. Lu JJ, Yin SB, Shen PK. Carbon-encapsulated electrocatalysts for the hydrogen evolution reaction. *Electrochem. Energy Rev.*, 2019, 2, 105-127.
6. Xiang Peng CP, Xuming Zhang, Shuai Li, Kaifu Huo and Paul K. Chu. Recent progress of transition metal nitrides for efficient electrocatalytic water splitting. *Sustain. Energy Fuels*, 2018.
7. Yan Jiao YZ, Kenneth Davey and Shi Zhang Qiao. Activity origin and catalyst design principles for electrocatalytic hydrogen evolution on heteroatom-doped graphene. *Nat. Energy*, 2016, 1.
8. Charlie Tsai a b, Karen Chana,b, Jens K. Nørskov a,b, Frank Abild Pedersen. Theoretical insights into the hydrogen evolution activity of layered transition metal dichalcogenides. *Surface Sci.*, 2015.
9. Zhang L, Wilkinson DP, Liu Y, Zhang J. Progress in nanostructured (Fe or Co)/N/C non-noble metal electrocatalysts for fuel cell oxygen reduction reaction. *Electrochim. Acta*, 2018, 262, 326-336.
10. Zhong X, Wang L, Zhuang Z, Chen X, Zheng J, Zhou Y, Zhuang G, Li X, Wang J. Double nanoporous structure with nanoporous ptfe embedded in graphene nanopores: highly efficient bifunctional electrocatalysts for hydrogen evolution and oxygen reduction. *Adv. Mater. Interfaces*, 2017, 4(5), 1601029.
11. Sharma M, Jung N, Yoo SJ. Toward high-performance Pt-based nanocatalysts for oxygen reduction reaction through organic-inorganic hybrid concepts. *Chem. Mater.*, 2018, 30(1), 2-24.
12. Lim B, Jiang M, Camargo PHC, Cho EC, Tao J, Lu X, Zhu Y, Xia Y. Pd-Pt bimetallic nanodendrites with high activity for oxygen reduction. *Science*, 2009, 324(5932), 1302-1305.

UNIVERSITY of the
WESTERN CAPE

http://etd.uwc.ac.za/

13. Lin R, Cai X, Zeng H, Yu Z. Stability of High-Performance Pt-Based Catalysts for Oxygen Reduction Reactions. *Adv. Mater.*, 2018, 30(17).
14. Ren Q, Wang H, Lu XF, Tong YX, Li GR. Recent progress on MOF-derived heteroatom-doped carbon-based electrocatalysts for oxygen reduction reaction. *Adv. Sci.*, 2018, 5(3).
15. Wang Y, Li J, Wei Z. Recent progress of carbon-based materials in oxygen reduction reaction catalysis. *Chemelectrochem*, 2018, 5(14), 1764-1774.
16. Wu Z, Song M, Wang J, Liu X. Recent progress in nitrogen-doped metal-free electrocatalysts for oxygen reduction reaction. *Catal.*, 2018, 8(5).
17. Chao T, Hu Y, Hong X, Li Y. Design of noble metal electrocatalysts on an atomic level. *Chemelectrochem*, 2019, 6(2), 289-303.
18. Li L, He J, Wang Y, Lv X, Gu X, Dai P, Liu D, Zhao X. Metal-organic frameworks: a promising platform for constructing non-noble electrocatalysts for the oxygen-reduction reaction. *J. Mater. Chem. A*, 2019, 7(5), 1964-1988.
19. Liu M, Zhao Z, Duan X, Huang Y. Nanoscale structure design for high-performance pt-based ORR catalysts. *Adv. Mater.*, 2019, 31(6).
20. Singh SK, Takeyasu K, Nakamura J. Active sites and mechanism of oxygen reduction reaction electrocatalysis on nitrogen-doped carbon materials. *Adv. Mater.*, 2019, 31(13).
21. Tan H, Tang J, Kim J, Kaneti YV, Kang YM, Sugahara Y, Yamauchi Y. Rational design and construction of nanoporous iron- and nitrogen-doped carbon electrocatalysts for oxygen reduction reaction. *J. Mater. Chem. A*, 2019, 7(4), 1380-1393.
22. Zhang C, Zhang W, Zheng W. Transition metal-nitrogen-carbon active site for oxygen reduction electrocatalysis: beyond the fascinations of TM-N-4. *Chemcatchem*, 2019, 11(2), 655-668.
23. Zhang J, Zhao Z, Xia Z, Dai L. A metal-free bifunctional electrocatalyst for oxygen reduction and oxygen evolution reactions. *Nat. Nanotechnol.*, 2015, 10(5), 444-452.
24. Lai L, Potts JR, Zhan D, Wang L, Poh CK, Tang C, Gong H, Shen Z, Lin J, Ruoff RS. Exploration of the active center structure of nitrogen-doped graphene-based catalysts for oxygen reduction reaction. *Energy Environ. Sci.*, 2012, 5(7), 7936-7942.
25. Zhang J, Yang H, Fang J, Zou S. Synthesis and Oxygen Reduction Activity of Shape-Controlled Pt3Ni Nanopolyhedra. *Nano Lett.*, 2010, 10(2), 638-644.
26. Mu S, Xu C, Yuan Q, Gao Y, Xu F, Zhao P. Degradation behaviors of perfluorosulfonic acid polymer electrolyte membranes for polymer electrolyte membrane fuel cells under varied acceleration conditions. *J. Appl. Polym. Sci.*, 2013, 129(3), 1586-1592.

UNIVERSITY of the
WESTERN CAPE

http://etd.uwc.ac.za/

27. Norskov JK, Rossmeisl J, Logadottir A, Lindqvist L, Kitchin JR, Bligaard T, Jonsson H. Origin of the overpotential for oxygen reduction at a fuel-cell cathode. *J. Phys. Chem. B*, 2004, 108(46), 17886-17892.
28. Calle-Vallejo F, Ignacio Martinez J, Rossmeisl J. Density functional studies of functionalized graphitic materials with late transition metals for oxygen reduction reactions. *Phys. Chem. Chem. Phys.*, 2011, 13(34), 15639-15643.
29. Huang J, Du X, Feng Y, Zhao Y, Ding Y. New insights into water oxidation reactions from photocatalysis, electrocatalysis to chemical catalysis: an example of iron-based oxides doped with foreign elements. *Phys. Chem. Chem. Phys.*, 2016, 18(15), 9918-9921.
30. Ding X, Yin SB, An K, Luo L, Shi N, Qiang YH, Pasupathi S, Pollet BG, Shen PK. FeN stabilized FeN@Pt core-shell nanostructures for oxygen reduction reaction. *J. Mater. Chem. A*, 2015, 3(8), 4462-4469.
31. Jing S, Luo L, Yin S, Huang F, Jia Y, Wei Y, Sun Z, Zhao Y. Tungsten nitride decorated carbon nanotubes hybrid as efficient catalyst supports for oxygen reduction reaction. *Appl. Catal., B*, 2014, 147, 897-903.
32. Luo L, Abbo HS, Titinchi SJJ, Tsiakaras P, Yin S. Highly efficient electrocatalysts for oxygen reduction reaction: Nitrogen-doped PtNiMo ternary alloys. *Inter. J. Hydrogen Energy*, 2019, 44(13), 6582-6591.
33. Yan Z, Xie J, Jing J, Zhang M, Wei W, Yin S. MoO_2 nanocrystals down to 5 nm as Pt electrocatalyst promoter for stable oxygen reduction reaction. *Inter. J. Hydrogen Energy*, 2012, 37(21), 15948-15955.
34. Yin S, Cai M, Wang C, Shen PK. Tungsten carbide promoted Pd-Fe as alcohol-tolerant electrocatalysts for oxygen reduction reactions. *Energy Environ. Sci.*, 2011, 4(2), 558-563.
35. Yin SB, Luo L, Jing SY, Zhu QQ, Qiang YH. Effect of intermittent microwave heating on the performance of catalysts for oxygen reduction reaction. *Acta Phys. Chim. Sin.*, 2012, 28(1), 85-89.
36. Zhang X, Lyu D, Mollamahale YB, Yu F, Qing M, Yin S, Zhang X, Tian ZQ, Shen PK. Critical role of iron carbide nanodots on 3D graphene based nonprecious metal catalysts for enhancing oxygen reduction reaction. *Electrochim. Acta*, 2018, 281, 502-509.
37. Hasche F, Oezaslan M, Strasser P. Activity, stability, and degradation mechanisms of dealloyed $PtCu_3$ and $PtCo_3$ nanoparticle fuel cell catalysts. *Chemcatchem*, 2011, 3(11), 1805-1813.
38. Mittermeier T, Weiss A, Gasteiger HA, Hasche F. Monometallic palladium for oxygen reduction in PEM fuel cells: particle-size effect, reaction mechanism, and voltage cycling stability. *J. Electrochem. Soc.*, 2017, 164(12), F1081-F1089.

UNIVERSITY of the
WESTERN CAPE

http://etd.uwc.ac.za/

39. Tamizhmani G, Dodelet JP, Guay D. Crystallite size effects of carbon-supported platinum on oxygen reduction in liquid acids. *J. Electrochem. Soc.*, 1996, 143(1), 18-23.
40. Jiang R, Tung SO, Tang Z, Li L, Ding L, Xi X, Liu Y, Zhang L, Zhang J. A review of core-shell nanostructured electrocatalysts for oxygen reduction reaction. *Energy Storage Mater.*, 2018, 12, 260-276.
41. Wang JX, Inada H, Wu L, Zhu Y, Choi Y, Liu P, Zhou W-P, Adzic RR. Oxygen reduction on well-defined core-shell nanocatalysts: particle size, facet, and Pt shell thickness effects. *J. Amer. Chem. Soc.*, 2009, 131(47), 17298-17302.
42. Wang YJ, Zhao N, Fang B, Li H, Bi XT, Wang H. Carbon-supported Pt-based alloy electrocatalysts for the oxygen reduction reaction in polymer electrolyte membrane fuel cells: Particle size, shape, and composition manipulation and their impact to activity. *Chem. Rev.*, 2015, 115(9), 3433-3467.
43. Rauf M, Wang J-W, Zhang P, Iqbal W, Qu J, Li Y. Non-precious nanostructured materials by electrospinning and their applications for oxygen reduction in polymer electrolyte membrane fuel cells. *J. Power Sources*, 2018, 408, 17-27.
44. Srinu A, Peera SG, Parthiban V, Bhuvaneshwari B, Sahu AK. Heteroatom engineering and Co-doping of N and P to porous carbon derived from spent coffee grounds as an efficient electrocatalyst for oxygen reduction reactions in alkaline medium. *ChemistrySelect*, 2018, 3(2), 690-702.
45. Wan X, Chen W, Yang J, Liu M, Liu X, Shui J. Synthesis and active site identification of Fe-N-C single-atom catalysts for the oxygen reduction reaction. *Chemelectrochem*, 2019, 6(2), 304-315.
46. Dai CHaL. Carbon-based metal-free catalysts for electrocatalysis beyond the orr. *Angew. Chem. Int. Ed.*, 2016, 55, 11736 – 11758.
47. Qu L, Liu Y, Baek J-B, Dai L. Nitrogen-doped graphene as efficient metal-free electrocatalyst for oxygen reduction in fuel cells. *ACS Nano*, 2010, 4(3), 1321-1326.
48. Wei Q, Tong X, Zhang G, Qiao J, Gong Q, Sun S. Nitrogen-doped carbon nanotube and graphene materials for oxygen reduction reactions. *Catal.*, 2015, 5(3), 1574-1602.
49. Xiong D, Li X, Fan L, Bai Z. Three-dimensional heteroatom-doped nanocarbon for metal-free oxygen reduction electrocatalysis: A review. *Catal.*, 2018, 8(8).
50. Yang S, Feng X, Wang X, Muellen K. Graphene-based carbon nitride nanosheets as efficient metal-free electrocatalysts for oxygen reduction reactions. *Angew. Chem. Inter. Ed.*, 2011, 50(23), 5339-5343.
51. Escalera-López D, Griffin R, Isaacs M, Wilson K, Palmer RE, Rees NV. Electrochemical sulfidation of WS_2 nanoarrays: Strong dependence of hydrogen

UNIVERSITY of the
WESTERN CAPE

http://etd.uwc.ac.za/

evolution activity on transition metal sulfide surface composition. *Electrochem. Commun.*, 2017, 81, 106-111.

52. Feng X, Bo X, Guo L. CoM(M=Fe,Cu,Ni)-embedded nitrogen-enriched porous carbon framework for efficient oxygen and hydrogen evolution reactions. *J. Power Sources*, 2018, 389, 249-259.
53. Seh ZW, Kibsgaard J, Dickens CF, Chorkendorff IB, Norskov JK, Jaramillo TF. Combining theory and experiment in electrocatalysis: Insights into materials design. *Science*, 2017, 355(6321).
54. Toth P, Jacobsson D, Ek M, Wiinikka H. Real-time, in situ, atomic scale observation of soot oxidation. *Carbon*, 2019, 145, 149-160.
55. Anantharaj S, Ede SR, Sakthikumar K, Karthick K, Mishra S, Kundu S. Recent trends and perspectives in electrochemical water splitting with an emphasis on sulfide, selenide, and phosphide catalysts of Fe, Co, and Ni: A review. *ACS Catal.*, 2016, 6(12), 8069-8097.
56. Tee SY, Win KY, Teo WS, Koh LD, Liu S, Teng CP, Han MY. Recent progress in energy-driven water splitting. *Adv. Sci.*, 2017, 4(5), 1600337.
57. Wang W, Xu X, Zhou W, Shao Z. Recent progress in metal-organic frameworks for applications in electrocatalytic and photocatalytic water splitting. *Adv. Sci.*, 2017, 4(4), 1600371.
58. de Souza RF, Padilha JC, Goncalves RS, de Souza MO, Rault-Berthelot J. Electrochemical hydrogen production from water electrolysis using ionic liquid as electrolytes: Towards the best device. *J. Power Sources*, 2007, 164(2), 792-798.
59. Wang Y, Mi Y, Redmon N, Holiday J. Understanding electrocatalytic activity enhancement of bimetallic particles to ethanol electro-oxidation. 1. Water adsorption and decomposition on Pt_nM (n) 2, 3, and 9; M) Pt, Ru, and Sn). *J. Phys. Chem. C*, 2010, 114, 317–326.
60. Spacil HS, Tedmon Jr. CS. Electrochemical dissociation of water vapor in solid oxide electrolyte cells I. Thermodynamics and cell characteristics. *J. Electrochem. Soc.*, 1969, 116(12), 1618-1626.
61. Jing S, Zhang L, Luo L, Lu J, Yin S, Shen PK, Tsiakaras P. N-doped porous molybdenum carbide nanobelts as efficient catalysts for hydrogen evolution reaction. *Appl. Catal., B*, 2018, 224, 533-540.
62. Zheng Y, Anthony VYJ, Qiao SZ. The hydrogen evolution reaction in alkaline solution: From theory, single crystal models, to practical electrocatalysts. *Angew. Chem. Int. Ed.*, 2018, 57, 7568-7579.

UNIVERSITY of the
WESTERN CAPE

http://etd.uwc.ac.za/

63. Zhang L, Lu J, Yin S, Luo L, Jing S, Brouzgou A, Chen J, Shen PK, Tsiakaras P. One-pot synthesized boron-doped RhFe alloy with enhanced catalytic performance for hydrogen evolution reaction. *Appl. Catal., B*, 2018, 230, 58-64.
64. Wang J, Xu F, Jin H, Chen Y, Wang Y. Non-noble metal-based carbon composites in hydrogen evolution reaction: Fundamentals to applications. *Adv. Mater.*, 2017, 29(14).
65. Rather RA, Singh S, Pal B. Core–shell morphology of Au-TiO_2@graphene oxide nanocomposite exhibiting enhanced hydrogen production from water. *J. Ind. Eng. Chem.*, 2016, 37, 288-294.
66. Brad AJ, Faulkner LR, *Electrochemical methods: Fundamentals and applications*. 1980: Wiley. 669-676.
67. Yan Y, Xia B, Xu Z, Wang X. Recent development of molybdenum sulfides as advanced electrocatalysts for hydrogen evolution reaction. *ACS Catal.*, 2014, 4(6), 1693-1705.
68. Greeley J, Jaramillo TF, Bonde J, Chorkendorff IB, Norskov JK. Computational high-throughput screening of electrocatalytic materials for hydrogen evolution. *Nat. Mater.*, 2006, 5(11), 909-913.
69. Norskov JK, Bligaard T, Logadottir A, Kitchin JR, Chen JG, Pandelov S, Norskov JK. Trends in the exchange current for hydrogen evolution. *J. Electrochem. Soc.*, 2005, 152(3), J23-J26.
70. Parsons R. The rate of electrolytic hydrogen evolution and the heat of adsorption of hydrogen. *Trans. Faraday Soc.*, 1958, 54(0), 1053-1063.
71. Esposito DV, Hunt ST, Kimmel YC, Chen JG. A new class of electrocatalysts for hydrogen production from water electrolysis: Metal monolayers supported on low-cost transition metal carbides. *J. Am. Chem. Soc.*, 2012, 134(6), 3025-33.
72. Durst J, Simon C, Hasché F, Gasteiger HA. Hydrogen oxidation and evolution reaction kinetics on carbon supported Pt, Ir, Rh, and Pd electrocatalysts in acidic media. *J. Electrochem. Soc.*, 2014, 162(1), F190-F203.
73. Palaniappan R, Botte GG. Effect of ammonia on Pt, Ru, Rh, and Ni cathodes during the alkaline hydrogen evolution reaction. *J. Phys. Chem. C*, 2013, 117(34), 17429-17441.
74. Smiljanic M, Rakocevic Z, Maksic A, Strbac S. Hydrogen evolution reaction on platinum catalyzed by palladium and rhodium nanoislands. *Electrochim. Acta*, 2014, 117, 336-343.
75. Štrbac S, Smiljanić M, Rakočević Z. Electrocatalysis of hydrogen evolution on polycrystalline palladium by rhodium nanoislands in alkaline solution. *J. Electroanal. Chem.*, 2015, 755, 115-121.

UNIVERSITY of the
WESTERN CAPE

http://etd.uwc.ac.za/

76. Cameron L. Bentley CA, Mathias Smialkowski, Minkyung Kang,Tsvetan Tarnev, Bernd Marler,Patrick R. Unwin, Ulf-Peter Apfel, Wolfgang Schuhmann. Local surface structure and composition control the hydrogen evolution reaction on iron nickel sulfides. *Angew. Chem. Inter. Ed.*, 2017, 12679.
77. Miao M, Pan J, He T, Yan Y, Xia BY, Wang X. Molybdenum carbide-based electrocatalysts for hydrogen evolution reaction. *Chem.*, 2017, 23(46), 10947-10961.
78. Sun B, Yang S, Guo Y, Xue Y, Tian J, Cui H, Song X. Fabrication of molybdenum and tungsten oxide, sulfide, phosphide ($Mo_xW_{1-x}O_2$/$Mo_xW_{1-x}S_2$/$Mo_xW_{1-x}P$) porous hollow nano-octahedrons from metal-organic frameworks templates as efficient hydrogen evolution reaction electrocatalysts. *J. Colloid Interface Sci.*, 2019, 547, 339-349.
79. Huang B, Zhou N, Chen X, Ong WJ, Li N. Insights into the electrocatalytic hydrogen evolution reaction mechanism on two-dimensional transition-metal carbonitrides (MXene). *Chem.*, 2018, 24(69), 18479-18486.
80. Song D, Wang H, Wang X, Yu B, Chen Y. $NiSe_2$ nanoparticles embedded in carbon nanowires as highly efficient and stable electrocatalyst for hydrogen evolution reaction. *Electrochim. Acta*, 2017, 254, 230-237.
81. Wu X, Han S, He D, Yu C, Lei C, Liu W, Zheng G, Zhang X, Lei L. Metal organic framework derived Fe-doped $CoSe_2$ incorporated in nitrogen-doped carbon hybrid for efficient hydrogen evolution. *ACS Sustainable Chem. Eng.*, 2018, 6(7), 8672-8678.
82. Jiang P, Chen J, Wang C, Yang K, Gong S, Liu S, Lin Z, Li M, Xia G, Yang Y, Su J, Chen Q. Tuning the activity of carbon for electrocatalytic hydrogen evolution via an iridium-cobalt alloy core encapsulated in nitrogen-doped carbon cages. *Adv. Mater.*, 2018, 30(9).
83. Gao K, Wang B, Tao L, Cunning BV, Zhang Z, Wang S, Ruoff RS, Qu L. Efficient metal-free electrocatalysts from N-doped carbon nanomaterials: Mono-doping and Co-doping. *Adv. Mater.*, 2019, 31(13).
84. Li MZaY. Recent advances in heterogeneous electrocatalysts for the hydrogen evolution reaction. *J. Mater. Chem. A*, 2015, 3, 14942.
85. Lyu Y, Wang R, Tao L, Zou Y, Zhou H, Liu T, Zhou Y, Huo J, Jiang SP, Zheng J, Wang S. In-situ evolution of active layers on commercial stainless steel for stable water splitting. *Appl. Catal., B*, 2019, 248, 277-285.
86. Zou X, Zhang Y. Noble metal-free hydrogen evolution catalysts for water splitting. *Chem. Soc. Rev.*, 2015, 44, 5148.

UNIVERSITY of the
WESTERN CAPE

http://etd.uwc.ac.za/

CHAPTER 2 Physico-Chemical Characterization

This chapter focuses on interpreting the methods and equipment employed for the physico-chemical characterization of the as-prepared electrocatalysts.

2.1 X-ray Powder Diffraction (XRD)

X-ray powder diffraction (XRD) spectra are used to qualitatively analyze samples whereby the X-ray diffraction phenomenon characterizes the structure of the as-prepared materials. The position and intensity of the diffraction peak can be used to analyze the phase composition, content, lattice parameters, and alloy degree. All of which are simple and effective.

Herein, XRD measurements were carried out using a D8 Advance X-ray diffractometer (BRUKER AXS, Germany), using Cu Ka radiation (λ_{Ka} = 0.15406 nm), operating at 40 kV and 30 mA. The 2q angular regions between 20° and 90° were finely scanned at 5° min^{-1} to obtain crystal sizes and lattice parameters according to the Scherrer equation and Vegard's law.[1,2]

$$D = \frac{0.9\lambda}{B\cos\theta} \quad (1)$$

$$a_{fcc} = \frac{\sqrt{2}\lambda}{\sin\theta} \quad (2)$$

Where D is the crystal size, a is the lattice parameter, λ_{Ka} is 0.15406 nm, θ is the angle of the diffraction peak, and B is the half-width of the diffraction peak of the corresponding crystal plane.

http://etd.uwc.ac.za/

2.2 X-ray Photoelectron Spectroscopy (XPS)

X-ray photoelectron spectroscopy (XPS) is an advanced analytical technique used in microscopic analysis of electronic materials and components on a material's surface. It can be used to measure the inner electron binding energy of atoms and their chemical shift, and provide information on the molecular structure and valence state. as well as information on the elemental composition, content of the compound, chemical state, molecular structure, and chemical bond. It can provide general chemical information, and give information on surfaces, micro-areas and depth distribution as well.

Therefore, XPS was used to analyze the composition and surface chemical states of various elements in different electrocatalysts, which could provide more information for us to further understand the mechanism of improving catalytic performance. XPS measurements were obtained using an ESCALAB 250 Xi (Thermo Fisher Scientific, USA) with an Al X-ray source operated at 150 W. Survey spectra were collected at a pass energy (PE) of 100.0 eV over the binding energy range of 0 to 1350 eV.

UNIVERSITY of the
WESTERN CAPE

2.3 BET Specific Surface Area

BET is an abbreviation for the BET specific surface area test method, which is named after the famous BET theory. BET is an acronym for three scientists (Brunauer, Emmett, and Teller), who derived the multi-molecular-layer adsorption formula from the classical statistical theory. The BET equation has become the theoretical basis for

http://etd.uwc.ac.za/

particle surface adsorption science. It is widely used in particle surface adsorption and data processing of related testing instruments.

The BET specific surface area test can be used to measure the specific surface area, pore volume, pore size distribution and nitrogen adsorption/desorption curve of the investigated particles. It plays an important role in studying the properties of the particle samples. The specific surface area and pore size distribution of the substrates were obtained using an ASAP 2420 (Micrometeritics Co., USA), by analyzing N_2 adsorption/desorption data at 77 K.

2.4 Scanning Electron Microscope (SEM)

Field emission scanning electron microscopy (FESEM) is a type of electron microscope. It has ultra-high resolution and can be used to perform the secondary electron image, reflection electron image observation and image processing of various solid sample's surface morphology. It has a high-performance x-ray energy spectrometer, which can simultaneously perform qualitative and semi-quantitative analysis of micro-area line and/or mapping elements on the surface of the samples, and analyze the morphology and chemical compositions. Scanning electron microscopy (SEM) measurements and elemental mapping analysis (EDS) were performed by a FE-SEM SU8220 (Hitachi Corp., Japan) to characterize the morphologies and compositions of the as-prepared materials.

UNIVERSITY of the
WESTERN CAPE

http://etd.uwc.ac.za/

2.5 Transmission Electron Microscope (TEM)

Transmission electron microscopy (TEM) functions by using electron beams and to project these into a sample. The different density components in the sample will emit corresponding electrons, which will display different images, thus distinguishing different components of the investigated samples. Scanning transmission electron microscopy (STEM) and energy dispersive X-ray spectroscopy (EDX) measurements were carried out using a TITAN ETEM G2 80-300 (FEI Co., USA) microscope at an accelerating voltage of 200 kV to obtain information on the structure and particle size distribution of the as-prepared electrocatalysts. High-resolution STEM and electron energy-loss spectroscopy (EELS) mapping were performed using a FEI TITAN 80–300 electron microscope (300 kV) equipped with a probe corrector (CEOS) and a high-angle annular dark field (HAADF) detector.

UNIVERSITY of the
WESTERN CAPE

The samples for TEM characterization were prepared as follows, a small amount of electrocatalyst was placed in a centrifuge tube followed by adding a few milliliters of ethanol, and the suspension of a known concentration was ultrasonically dispersed after which the suspension was dropped onto the copper mesh containing a carbon film, and then allowed to dry naturally for further characterization.

http://etd.uwc.ac.za/

2.6 References

1. Ding X, Yin SB, An K, Luo L, Shi N, Qiang YH, Pasupathi S, Pollet BG, Shen PK. FeN stabilized FeN@Pt core-shell nanostructures for oxygen reduction reaction. *J. Mater. Chem. A*, 2015, 3(8), 4462-4469.
2. Lu QY, Yang B, Zhuang L, Lu JT. Pattern recognition on the structure-activity relationship of nano Pt-Ru catalysts: Methodology and preliminary demonstration. *J. Phys. Chem. B*, 2005, 109(18), 8873-8879.

UNIVERSITY of the
WESTERN CAPE

http://etd.uwc.ac.za/

CHAPTER 3 Enhancement of ORR via the Introduction of the Acid-Resistant Refractory Mo and Regulating the Near-Surface Pt Content

This work focuses on the study of the Mo regulating PtNiMo ternary alloys as efficient electrocatalysts for the oxygen reduction reaction and the corresponding mechanism for oxygen reduction is discussed. Results described in this section come from the submitted article for publication.

3.1 Introduction

Proton exchange membrane fuel cells (PEMFCs) have the advantages of high efficiency and environmental benignity for hydrogen and oxygen conversion. However their commercialization is hindered by the high cost and poor stability of electrocatalysts.[1-3] In particular, the oxygen reduction reaction (ORR) at the cathode is critical for PEMFCs due to the sluggish oxygen reduction kinetics.[4-7] Although fruitful developments have been achieved, the development of more active and stable electrocatalysts remains a major challenge.

In order to address these problems, researchers have developed low platinum containing electrocatalysts,[8] non-noble metal electrocatalysts,[9] and non-metallic electrocatalysts.[10] In terms of structure, they can be divided into nanoframes,[11-13] core-shell structures,[14-16] and alloy structures.[17] Compared with other structures, the lattice shrinkage effect and surface electron coordination effect in the alloy structure reduces the Pt-Pt atomic spacing and increases the overlap of electron states

UNIVERSITY of the WESTERN CAPE
http://etd.uwc.ac.za/

on Pt. This has the net effect to thus down shift the *d*-band center of Pt and further reduce the over strong binding to oxygenated intermediate species and thereby improving the ORR activity.[18; 19] Furthermore, the alloy structure is easier to synthesize and can be produced on a large scale.

It is found that Fe, Co, Ni and Pd as well as modified Pt alloys have good oxygen reduction activity, due to the influence of the lattice shrinkage effect and surface electron coordination effect in the alloy electrocatalyst.[20] The reaction activation energy is reduced and the atomic spacing of Pt-Pt is also reduced, to thus improve the oxygen reduction activity.[21] However, Fe, Co, Ni and other metals in the alloy will inevitably dissolve in the acidic solution, thus deteriorating the stability. In particular, the dissolved Fe^{2+} will adversely affect the proton exchange membrane under the action of H_2O_2, an intermediate product of oxygen reduction.[22; 23] Based on the above reasons, Adzic *et al.* synthesized a kind of NiN@Pt core-shell structure electrocatalyst and evaluated it for oxygen reduction. The results show that the introduced nitrogen element can form covalent bonds with Ni, and the Ni_4N nuclear nanoparticles generated by the reaction between NH_3 and Ni at high temperature have stable structures. In addition, this core-shell can also regulate the oxygen reduction activity of platinum on the surface layer.[24] Huang *et al.* found that the Mo doped PtNi octahedron displayed a relatively higher activity and stability. This is believed to be due to the introduction of Mo atoms which not only forms ultra-high oxygen reduction active sites on the electrocatalyst's surface, but also stabilizes the surface atoms. The oxide of Mo on the surface can stabilize the adjacent Pt sites and prevent

UNIVERSITY of the
WESTERN CAPE
http://etd.uwc.ac.za/

loss of Ni under the platinum layer, thus improving the stability.[25; 26] However, the thermodynamics of the Mo-doped PtNi octahedron structure is unstable since molybdenum doping can only modify the surface atoms, and has limited influence on the inner layer atoms. During long-term testing, once the Pt and Ni atoms modified by Mo on the surface are dissolved or migrated, the unmodified nickel atoms on the inner layer will inevitably be destroyed, resulting in the disappearance of high index crystal planes in the octahedron and the formation of spherical particles. This in turn leads to the decline of catalytic activity. Therefore, it is vitally important to balance the activity and stability of the synthesized catalytic materials.

Herein we describe the synthesis of nitrogen-doped PtNiMo alloy electrocatalysts (PtNiMoN) with different atomic ratios by impregnation reduction followed by annealing in a NH_3 atmosphere (Figure 3.1). Electrochemical tests showed that the alloy formed by Mo and PtNi has higher activity and stability than the traditional PtNi alloy electrocatalyst. In addition, the content of Pt in PtNiMoN/C alloy nanoparticles was adjusted to further optimize catalytic performance. The results indicate that the electrocatalyst with a Pt:Ni:Mo atomic ratio of 3:3:1, named as Pt_3Ni_3MoN/C, possessed the optimal performance, considering the balance between activity and stability. Specifically, it showed mass activity of 900 mA mg^{-1} Pt at 0.90 V *vs*. RHE in O_2-saturated 0.1 mol L^{-1} $HClO_4$ aqueous solutions, which is 3.75-fold higher compared with the commercial Pt/C electrocatalyst (240 mA mg^{-1} Pt). After 30k accelerated durability tests (ADTs), the mass activity (MA) of Pt_3Ni_3MoN/C is still 690 mA mg^{-1} Pt, which activity remains ~75%, while the Pt/C merely retains ~44%.

UNIVERSITY of the
WESTERN CAPE
http://etd.uwc.ac.za/

This is attributed to the fact that the acid-resistant refractory Mo or its oxide in alloy electrocatalysts can effectively prevent the migration and dissolution of Pt and Ni atoms, thus reducing the loss of highly active sites. Moreover, the NiN formed by nitrogen doping can slow down the corrosion of nickel in acid solution and thus be conducive to maintain catalytic activity.

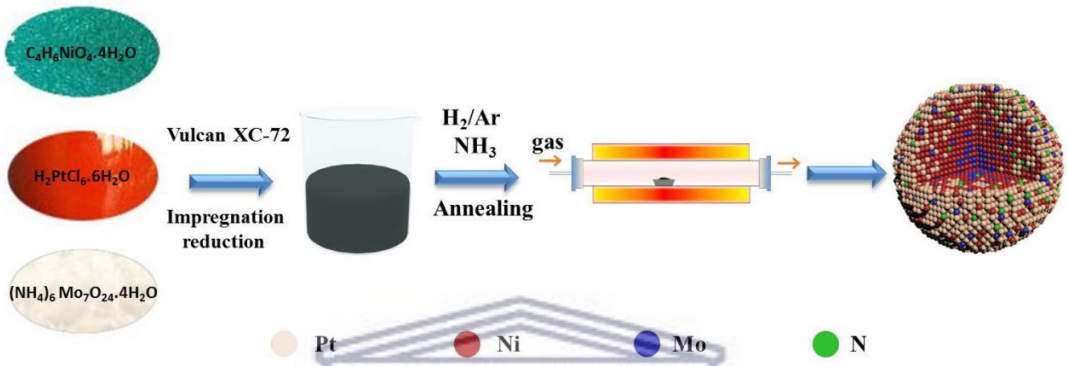

Figure 3.1 Schematic diagram for the synthesis of PtNiMo alloy electrocatalysts.

UNIVERSITY of the
WESTERN CAPE

3.2 Experimental

3.2.1 Electrocatalysts Preparation

Ternary PtNiMo alloy electrocatalysts (40wt% of total metal loading with different atomic ratios) were prepared by reducing the Pt, Ni and Mo precursors with $NaBH_4$ in the presence of the carbon support, followed by calcination at high temperature. In a typical synthesis of PtNiMoN/C electrocatalysts: i) Chloroplatinic acid (H_2PtCl_6•$6H_2O$), ii) nickel acetate ($C_4H_6NiO_4$•$4H_2O$), iii) Ammonium molydate tetrahydrate ($(NH_4)_6$ Mo_7O_{24}•$4H_2O$) and iv) Vulcan XC-72 were added to deionized water, and then untrasonicated and stirred to form a uniform slurry. Afterwards, the

http://etd.uwc.ac.za/

reducing agent $NaBH_4$ is added to the slurry drop by drop. After several hours, the product was filtered, washed and dried, using a vacuum oven (70 ^oC for 24 h) and then ground into a powder. This sample was heated to 380 ^oC (heating rate: 10 ^oC min^{-1}) in a tubular furnace oven under H_2/Ar (5% H_2). After holding at this temperature for 30 min, the material was heated to 500 ^oC (heating rate: 10 ^oC min^{-1}) under a flow of NH_3 and kept for 2 h. The obtained products are denoted as Pt_3Ni_5MoN/C, Pt_3Ni_3MoN/C, Pt_3NiMoN/C and PtNiN/C, respectively. In addition, the benchmark electrocatalyst is the commercial Pt/C (TKK) with Pt content of 46.7 wt%.

3.2.2 Electrocatalysts Characterization

The crystal structure of the synthesized ternary PtNiMo alloy was confirmed by XRD using a D8 Advance X-ray diffract meter (BRUKER AXS, Germany), equipped with Cu $K\alpha$ radiation (λ = 15406 nm). Accelerating voltage and the applied current were 40 kV and 30 mA. The 2θ scanning range is from 30° to 90° with a speed of 5° min^{-1} to obtain lattice parameters according to the Vagary's law. Scanning transmission electron microscopy (STEM) and energy dispersive X-ray spectroscopy (EDS) measurements were characterized by an environmental spherical aberration corrected scanning transmission electron microscope (Titan ETEM G2 80-300, FEI Company, and America) to obtain information about structure and particle size distribution of the as-prepared electrocatalysts. The elemental content was quantified by inductively coupled plasma optical emission spectroscopy (ICP-OES, Thermo

UNIVERSITY of the
WESTERN CAPE

http://etd.uwc.ac.za/

Fisher iCAP 7400, USA). X-ray photoelectron spectroscopy (XPS) data was recorded by an ESCALAB-250i instrument (Thermo Fisher, USA), using a monochromatic Al-Kα radiation source. Survey spectra were collected at a pass energy (PE) of 100.0 eV over the binding energy range of 0~1350 eV.

Electrochemical measurements were conducted using a bipotentiostat WD-20 BASIC (Pine Research Instrumentation, USA) in a thermostatically-controlled standard three-electrode cell at 25 ^{o}C, employing a platinum foil and Ag/AgCl as the counter electrode and reference electrode, respectively. The Ag/AgCl was calibrated against a reversible hydrogen electrode (RHE) as reported.[27] A rotating disk electrode (RDE) with a surface area of 0.196 cm^2 was used as the substrate for the electrocatalyst thin films in the electrochemical measurements. The thin film electrocatalyst layer was prepared as the working electrode as follows: A mixture containing 5.0 mg electrocatalyst, 1.96 mL ethanol and 0.04 mL Nafion® solution (5.0 wt%) was dispersed in an ultrasonic bath for 15 min to obtain a uniform dispersion ink. Then, 10 μL of this ink was placed on a glassy carbon electrode and dried by a rotary drying method. The estimated electrocatalyst's loading for the home-made electrocatalysts and commercial Pt/C are the same (0.127 mg cm^{-2}) in this work. The prepared electrocatalysts were activated by cyclic voltammetry (CV) experiments in N_2-saturated 0.1 mol L^{-1} $HClO_4$ aqueous solutions with the scan rate of 50 mV s^{-1}. ORR activities for all the electrocatalysts were measured by the linear sweep voltammetry (LSV) method in O_2-saturated 0.1 mol L^{-1} $HClO_4$ aqueous solutions scanned from 0 to 1.1 V *vs*. RHE at a rotating speed of 1,600 rpm with a scan rate of 5

UNIVERSITY of the WESTERN CAPE

http://etd.uwc.ac.za/

mV s^{-1}. To eliminate any capacitive current contribution, the background current was also measured by the LSV program under the same condition in N_2-saturated 0.1 mol L^{-1} $HClO_4$ aqueous solutions. In addition, the uncompensated resistance of the system was about 30 Ω, measured via high frequencies AC impedance in O_2-saturated 0.1 mol L^{-1} $HClO_4$ aqueous solutions. The result was similar to some reports in the same type of electrolyte. The potentials were corrected by using the following equation:

$$E_{iR\text{-}correction} = E_{applied} - iR \qquad (1)$$

Where *i* is the ORR measured current and *R* is the uncompensated resistance of system. The accelerated durability tests (ADT) were conducted by the CV method between 0 and 1.1 V *vs*. RHE in O_2-saturated 0.1mol L^{-1} $HClO_4$ aqueous solutions.

3.3 Results and Discussions

3.3.1 Physico-Chemical Characterization

UNIVERSITY of the
WESTERN CAPE

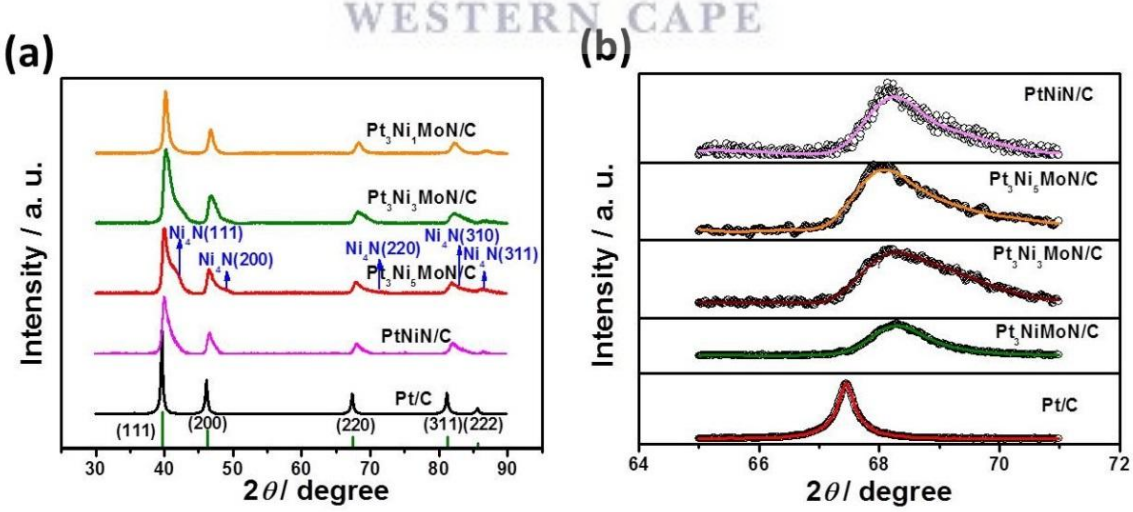

Figure 3.2 (a) XRD curves of the as-prepared samples with a scan rate of 5 min^{-1}. (b) Curve fitting for (220) diffraction peaks in part (a).

http://etd.uwc.ac.za/

As shown in Figure 3.2a, the 2θ values of 39.763°(111), 46.243°(200), 67.469°(220), 81.264°(311) and 85.712°（222）indicate the characteristic diffraction peaks of polycrystalline Pt (PDF#70-2057). Compared with the Pt/C, the characteristic diffraction peaks of other electrocatalysts offset to a higher angle, indicating the shrinkage of lattice spacing. This could be due to the incorporation of the smaller atomic radius of Ni and Mo atoms into the Pt lattice. The 2θ values of 41.784°(111), 48.650°(200), 71.401°(220), 81.503°(310) and 85.948° (311) are assigned to the Ni_4N (PDF#36-1300), which confirms that Ni forms Ni_4N nanoparticles with NH_3 at high temperature.[24] To precisely obtain the degree of shrinkage, the Gauss function was employed to fit the Pt(220) diffraction peaks in Figure 3.2b. From the fitted curves, the peak maximum (θ_{max}) position can be identified and the lattice parameters (α) of the samples can be further calculated by Vagary's law:[28]

UNIVERSITY of the
WESTERN CAPE

$$\alpha = \frac{\sqrt{2}\lambda_{k\alpha 1}}{\sin\theta_{max}} \quad (2)$$

Where $\lambda_{k\alpha 1}$ = 0.15406 nm (Cu Kα radiation). The lattice parameters of Pt_3Ni_5MoN/C, Pt_3Ni_3MoN/C, Pt_3NiMoN/C and PtNiN/C are 3.90, 3.89, 3.88 and 3.89 Å, respectively, which are smaller to the commercial Pt/C (3.92 Å). The difference of lattice shrinkages is believed to be caused by the different ratios of Ni and Mo in the lattice. It will increase the overlap of Pt electronic states, giving rise to decrease the *d*-band center of Pt that weakness the over strong binding to oxygenated intermediate species and it is facile for re-freshing the active sites.[29;

http://etd.uwc.ac.za/

30] The structural parameters of the as-prepared samples obtained from XRD are summarized in Table 3.1.

Table 3.1 Structural parameters of the samples extracted from X-ray powder diffraction.

Name	**2-theta (degree) (220) faced**	**Lattice parameter (Å) *α***
Pt_3Ni_5MoN/C	67.91	3.90
Pt_3Ni_3MoN/C	68.19	3.89
Pt_3NiMoN/C	68.32	3.88
PtNiN/C	68.15	3.89
Pt/C	67.45	3.92

A TEM image (Figures 3.3a and 3.4a) shows that the spherical Pt_3Ni_3MoN nanoparticles at about 6.58 nm are evenly distributed on the carbon carriers. The 0.225 and 0.196 nm of interplanar spacing in Figures 3.3b and 3.3c correspond to the (111) and (200) crystal facets of Pt alloys. In addition, EDS mappings (Figures 3.3d-j) and line profiles (Figure 3.5) are effective tools for elucidating the composition and structure of nanoparticles. It can be seen from Figures 3.3f-j that the Pt, Ni and Mo atoms are uniformly dispersed over the alloy, and indeed, the nitrogen atoms can also be observed. The possible reason for this is that the metal nitride is formed by heating under the NH_3 atmosphere.[31] Furthermore, combined with XRD and XPS patterns (Figure 3.6), it is safe to infer that the metal nitride is nickel nitride. The line profiles of Pt_3Ni_5MoN/C, Pt_3Ni_3MoN/C, and Pt_3NiMoN/C nanoparticles further proves the compositions of nanoparticles, indicating a typical platinum-rich alloy structure.

UNIVERSITY of the
WESTERN CAPE

http://etd.uwc.ac.za/

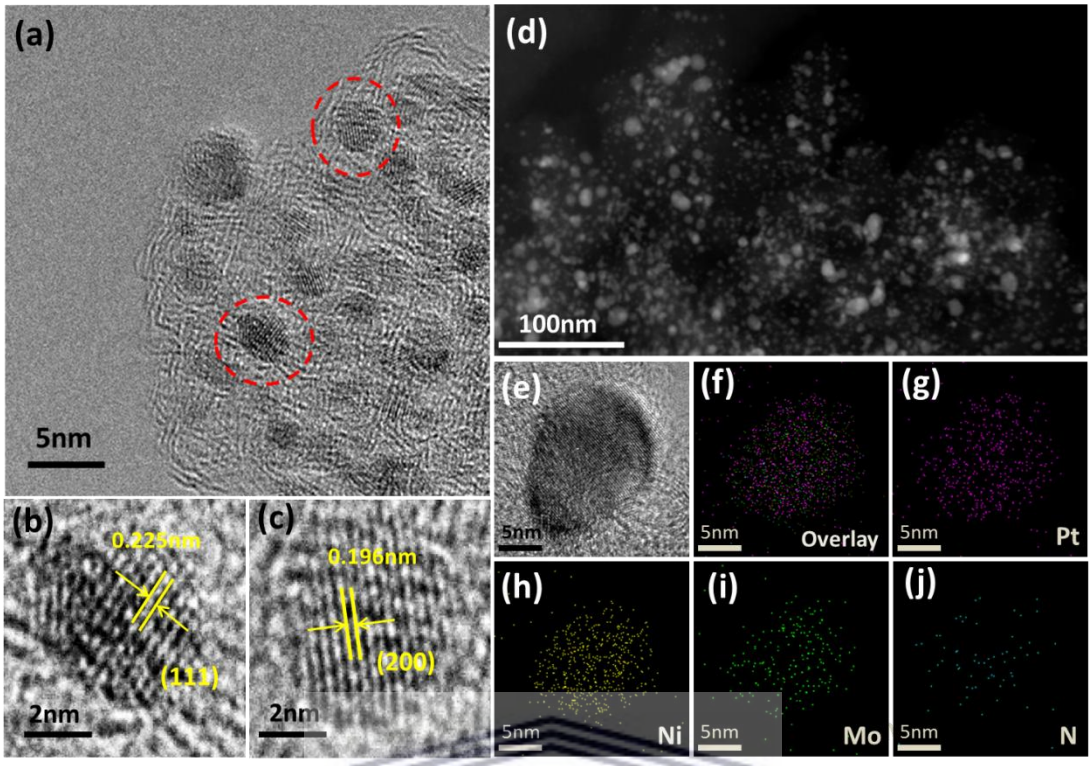

Figure 3.3 (a-c) TEM and HRTEM images of Pt_3Ni_3MoN/C, (d) HAADF-STEM image, (e) HRTEM image of a Pt_3Ni_3MoN alloy nanoparticle, (f) Overlapped mapping image of (g) Pt, (h) Ni, (i) Mo and (j) N elements.

UNIVERSITY of the
WESTERN CAPE

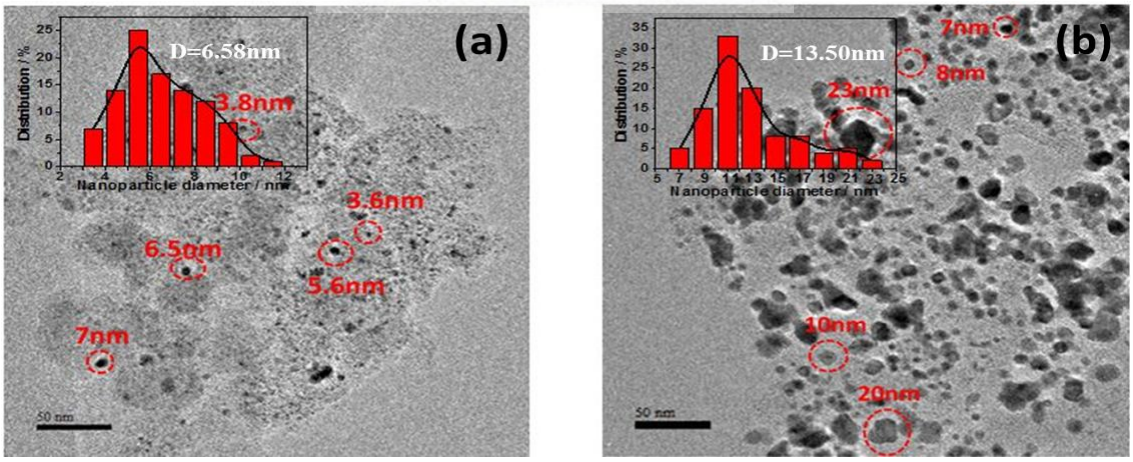

Figure 3.4 (a) A TEM image of Pt_3Ni_3MoN/C and the corresponding distribution map of particle size before testing, (b) A TEM image of Pt_3Ni_3MoN/C and the corresponding distribution map of particle size after 30k CV cycles testing.

http://etd.uwc.ac.za/

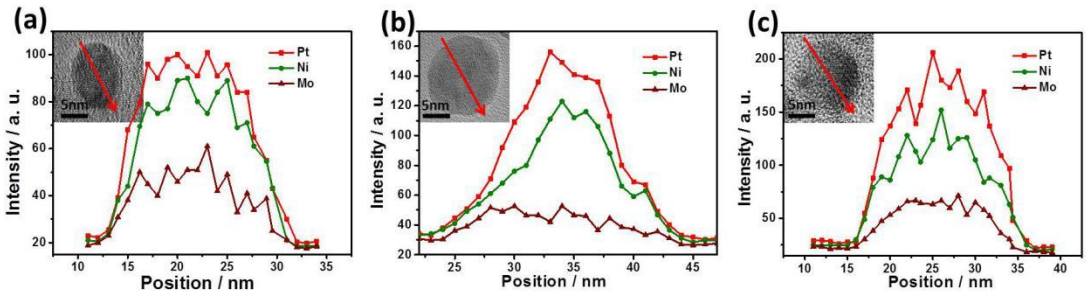

Figure 3.5 (a–c) Line profiles of Pt, Ni and Mo for Pt_3Ni_5MoN/C, Pt_3Ni_3MoN/C, and Pt_3NiMoN/C nanoparticles. The red arrows indicate the directions of the line profiles.

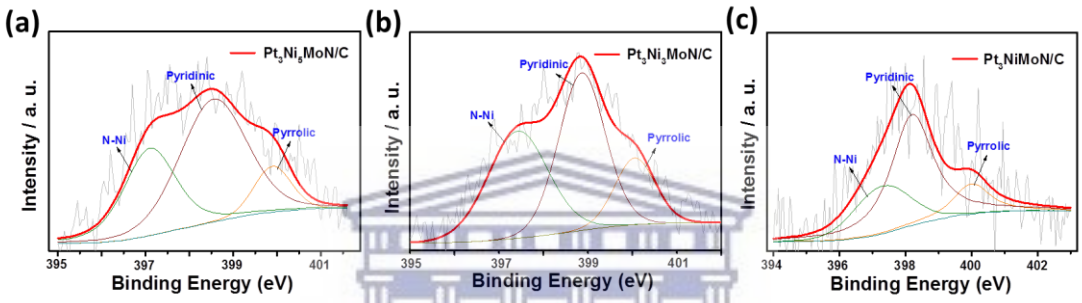

Figure 3.6 (a-c) XPS peaks of N1s in Pt_3Ni_5MoN/C, Pt_3Ni_3MoN/C, and Pt_3NiMoN/C nanoparticles, respectively.

UNIVERSITY of the
WESTERN CAPE

The surface composition and micro-structure of the synthesized electrocatalysts are characterized by XPS. As shown in Figure 3.7a, the O1s peaks for all the prepared electrocatalysts and Pt/C can be observed. This phenomenon is due to the nature of the metal nanoparticles, which are easily oxidized by oxygen in the air. Moreover, the peaks of Pt4f and Ni2p can be seen in Figure 3.7a, while the peaks of N1s and Mo3d are inconspicuous, which may be due to the lower content of N and Mo elements than that of Pt and Ni in the electrocatalysts. Another reason is that Mo is deeply

http://etd.uwc.ac.za/

embedded in the core due to the different adsorption enthalpy of H_2 in the process of metal segregation.

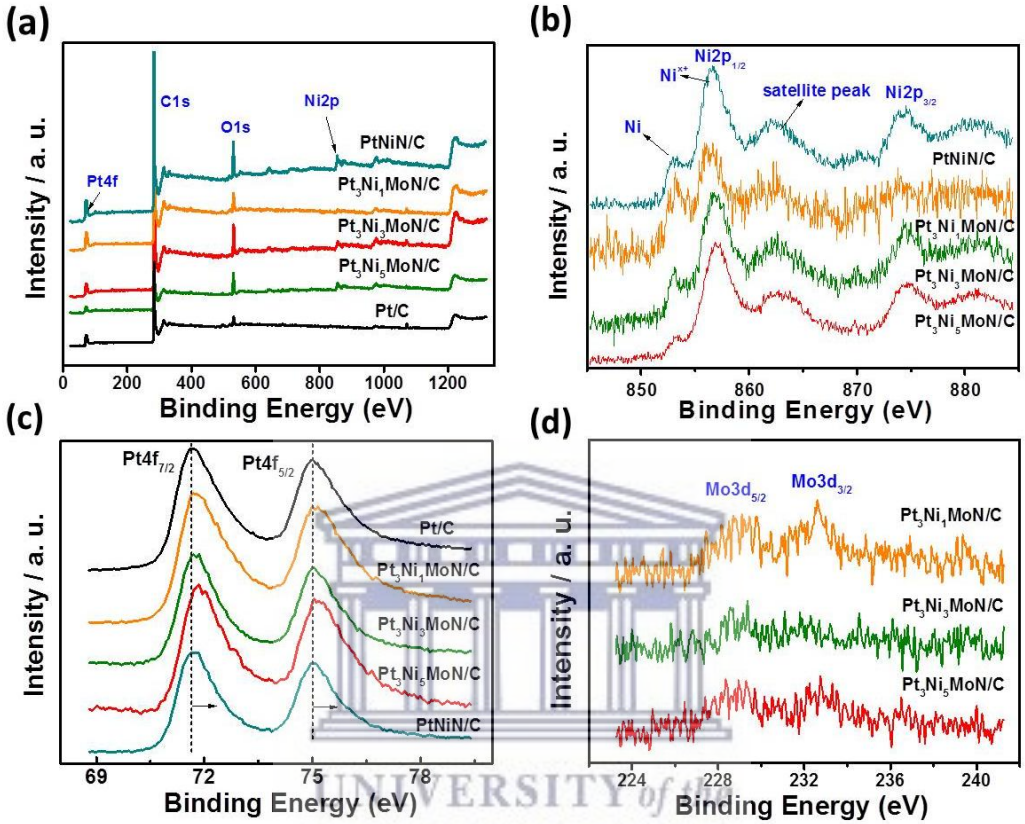

UNIVERSITY of the
WESTERN CAPE

Figure 3.7 (a) XPS spectra of the investigated materials: (b) Ni2p, (c) Pt4f, and (d) Mo3d.

These peaks at 853.18 and 856.72 eV in Figure 3.7b correspond to Ni and Ni^{2+} and the latter could be an oxide. As displayed in Figure 3.7c, the Pt_{4f} orbit of PtNiMo ternary alloys moves to a higher binding energy compared with Pt/C, which will lower the *d*-band center of Pt and thus improve the catalytic activity for ORR.[32] Furthermore, as illustrated in Figure 3.7d, it can be detected that even the peak intensity of Mo is weaker than that of Pt and Ni elements, it further confirms that the

http://etd.uwc.ac.za/

Mo atoms are successfully introduced into the alloy. Figures 3.6a-c are N1s peaks of Pt_3Ni_5MoN/C, Pt_3Ni_3MoN/C, and Pt_3NiMoN/C. Clearly, the nitrogen element in the synthesized samples exists in the form of Ni-N, pyridine N and pyrrole N, and the pyridine N is the main component. As reported, the pyridine N has a positive effect on improving the oxygen reduction activity, which could also enhance the interactions between the nanoparticles and the support materials.[33]

The atomic ratios of each component in the prepared electrocatalysts were quantified by ICP-OES. As shown in Table 3.2, the atomic ratios of Pt:Ni:Mo are different from the nominal ratios in the as-prepared electrocatalysts, which may be due to the fact that during the filtration step, it will inevitably loose parts of metals and supports, thus affecting the real atomic ratios in the obtained samples.

UNIVERSITY of the
WESTERN CAPE

http://etd.uwc.ac.za/

Table 3.2 Contents and atomic ratios of Pt to Ni to Mo in all the investigated samples.

Name	**$\eta_{Pt}/\omega t\%$ (nominal)**	**$\eta_{Ni}/\omega t\%$ (nominal)**	**$\eta_{Mo}/\omega t\%$ (nominal)**	**Pt:Ni:Mo Atomic ratios (nominal)**	**$\eta_{Pt}/\omega t\%$ (real)**	**$\eta_{Ni}/\omega t\%$ (real)**	**$\eta_{Mo}/\omega t\%$ (real)**	**Pt:Ni:Mo Atomic ratios (real)**
Pt_3Ni_5MoN/C	24%	12%	4%	3:5:1	21%	11%	1.1%	1:2:0.2
Pt_3Ni_3MoN/C	27%	8%	5%	3:3:1	28.5%	8.8%	1.4%	1:1:0.2
Pt_3NiMoN/C	31.5%	3%	5.5%	3:1:1	33%	3.5%	1.5%	2.5:1:0.5
PtNiN/C	30.6%	9.4%		1:1	31.2%	9.3%		1:1

UNIVERSITY of the
WESTERN CAPE

http://etd.uwc.ac.za/

3.3.2 The Effect of Mo on the ORR Kinetics

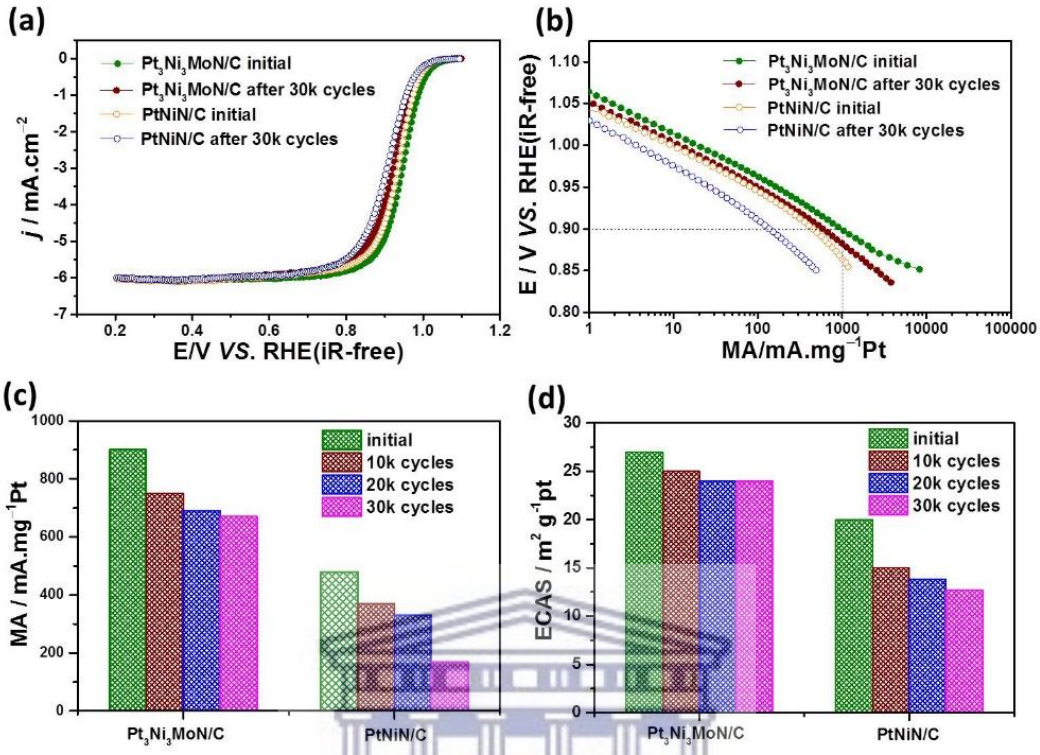

Figure 3.8 (a) ORR polarization curves of Pt_3Ni_3MoN/C and PtNiN/C in O_2-saturated 0.1 mol L^{-1} $HClO_4$ aqueous solutions before and after ADT, 25°C, scan rate 5 mV s^{-1}, rotating rate 1,600 rpm; (b) Comparison of MA before and after 30k cycles; (c) Comparison of MA during the ADT at 0.90 V; (d) Comparison of ECSA during the ADT.

UNIVERSITY of the
WESTERN CAPE

To investigate the effect of Mo on improving the ORR activity and stability, we synthesized Pt_3Ni_3MoN/C and PtNiN/C ternary alloy electrocatalysts and evaluated their performance for the ORR. In general, the Pt_3Ni_3MoN/C showed better ORR activity and stability than the PtNiN/C. As show in Figure 3.8a, the half wave potential $E_{1/2}$ of Pt_3Ni_3MoN/C is 0.95 V, higher than PtNiN/C (0.93 V). It indicates that the introduction of Mo could enhance the ORR activity. After 30k cycles, its $E_{1/2}$ reduces to 0.93 V. The variation of $E_{1/2}$ (20 mV) is smaller than that of PtNiN/C (30

http://etd.uwc.ac.za/

mV), proving the Mo plays an important role in improving the ORR stability. The kinetic current (I_k) for the ORR on the electrode is further analyzed by the aid of Koutecky-Levich equation:[34]

$$\frac{1}{I} = \frac{1}{I_k} + \frac{1}{I_d} \quad (3)$$

Where I is the measured current and I_d is the diffusion limited current. The mass activities (MA) of Pt_3Ni_3MoN/C and PtNiN/C at 0.90 V are 900 and 480 mA mg^{-1} Pt (Figures 3.8b-c). After 30k potential sweeping cycles, the MA of Pt_3Ni_3MoN/C still remains at 670 mA mg^{-1} Pt, only a 25% drop compared with the initial activity. The MA of PtNiN/C is 170 mA mg^{-1} Pt after 30k cycles, representing attenuation up to 64%. By comparing the above evaluation parameters before and after ADT, it can be inferred that the introduction of the Mo does improve the catalytic activity and stability.

UNIVERSITY of the
WESTERN CAPE

ECSA is one of the important criteria to evaluate the catalytic activity and stability. As shown in Figure 3.8d, the Pt_3Ni_3MoN/C has little change in ECSA calculated by CO-stripping voltammograms (Figure 3.10), while PtNiN/C has a large change in ECSA in the stability test, which further proves that the Pt_3Ni_3MoN alloy possesses better stability than the electrocatalysts without Mo. The Mo element plays a significant role in enhancing the catalytic activity and stability for ORR. Possible reasons are as follows:

i) When Mo atoms are embedded into the PtNi alloy system, the electron density of Pt will further increase because of the weaker electronegativity of Mo (2.16) than

http://etd.uwc.ac.za/

that of Pt (2.28). As a result, the *d*-band center of the Pt downshift is facile to the desorption of oxygenated intermediate species, re-exposing the adsorbed active sites and improving the ORR catalytic activity.[35]

ii) Considering that Mo itself has highly unsaturated 4d orbitals and it is combined with Pt with strong electronegativity, the unsaturated 4d orbitals of Mo will further increase, which is in favor of the adsorption of O_2 on Mo atoms. It also makes up the decreased adsorption of O_2 on Pt atoms.[36]

iii) The acid-resistant refractory Mo or its oxide in alloy electrocatalysts can effectively prevent the migration and dissolution of Pt and Ni atoms, reducing the loss of highly active sites.[37]

3.3.3 The Regulation of Near-Surface Pt Content in PtNiMoN Alloy

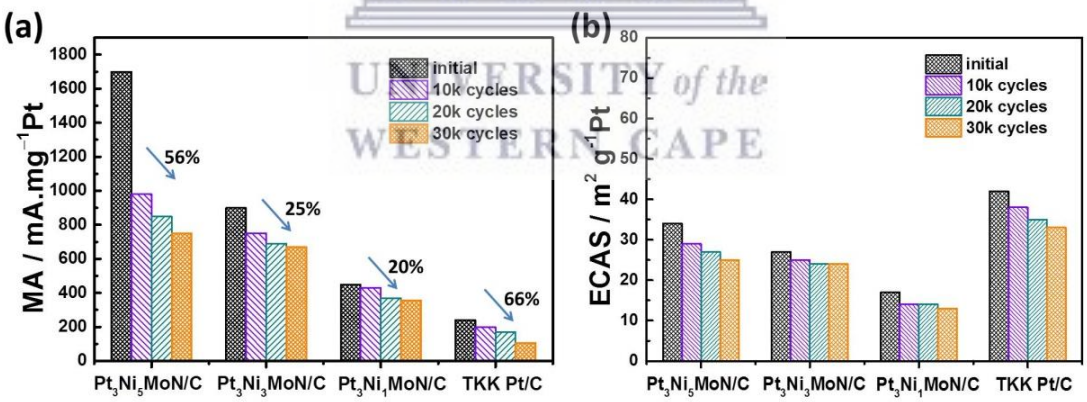

Figure 3.9 (a) Comparison of MA during ADT at 0.90 V; (b) Comparison of ECSA during ADT.

In order to further optimize the ORR catalytic performance and balance the catalytic activity and stability, the near-surface Pt content is regulated and the corresponding electrochemical results are shown in Figure 3.11. As shown in Table 3.3, the half-

http://etd.uwc.ac.za/

wave potentials ($E_{1/2}$) of Pt_3Ni_5MoN/C, Pt_3Ni_3MoN/C, Pt_3NiMoN/C, and Pt/C are 0.96, 0.95, 0.95 and 0.94 V before the ADT test. After 30k cycles, their $E_{1/2}$ decrease to 0.93, 0.93, 0.94 and 0.90 V, respectively. It means that the stability of PtNiMoN alloy is better than that of the commercial Pt/C. The MAs during the ADT for Pt_3Ni_5MoN/C, Pt_3Ni_3MoN/C, Pt_3NiMoN/C and Pt/C are summarized in Table 3.4 and shown in Figure 3.9a. Their initial MAs are 1,700, 900, 450 and 240 mA mg^{-1} Pt, while their MAs become 750, 670, 356 and 105 mA mg^{-1} Pt after 30k cycles, declines 56%,25%,20% and 66%, respectively.

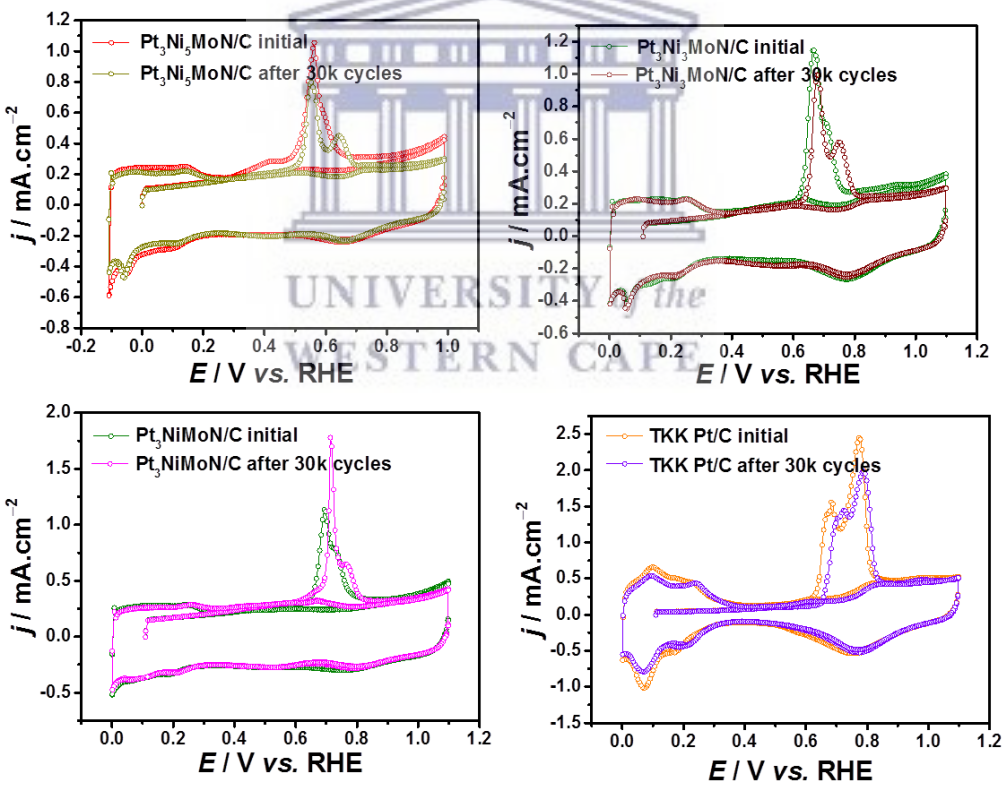

Figure 3.10 (a-d) CO stripping before and after ADT, by maintaining the potential at 0.15 V for 15 min in CO and 30 min in aqueous solutions saturated with N_2 and acidified with $HClO_4$ (0.10 mol L^{-1}), 20 mV s^{-1}.

http://etd.uwc.ac.za/

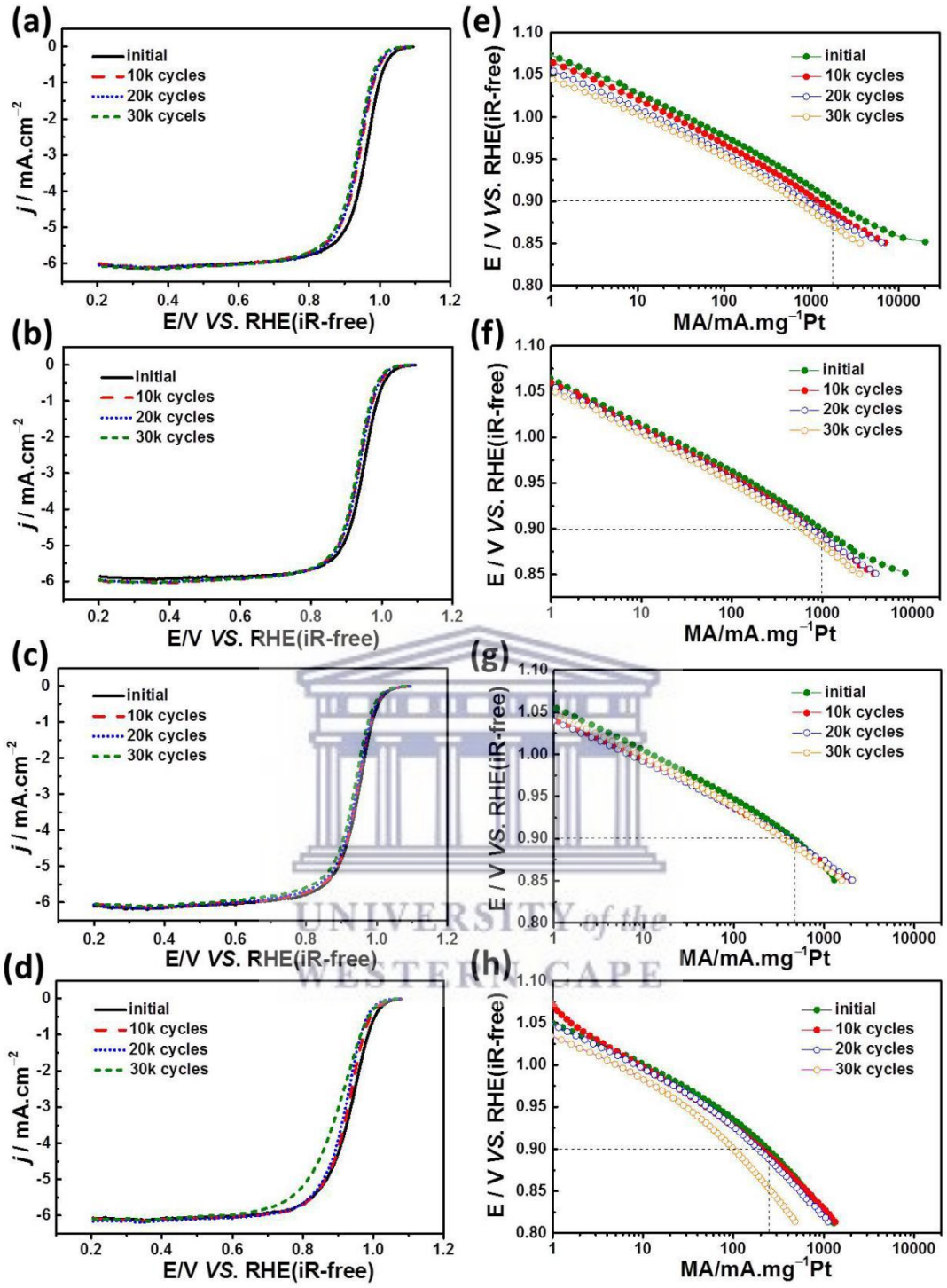

Figure 3.11 (a-d) ORR polarization curves of Pt_3Ni_5MoN/C, Pt_3Ni_3MoN/C, Pt_3NiMoN/C and TKK Pt/C in O_2-saturated 0.1 mol L^{-1} $HClO_4$ aqueous solutions before and after ADT, 25ºC, scan rate 5 mV s^{-1}, rotating rate 1,600 rpm. (e-h) MAs for Pt_3Ni_5MoN/C, Pt_3Ni_3MoN/C, Pt_3NiMoN/C compared with Pt/C before and after 30k cycles.

http://etd.uwc.ac.za/

Table 3.3 Half-wave potentials ($E_{1/2}$) of Pt_3Ni_5MoN/C, Pt_3Ni_3MoN/C, Pt_3NiMoN/C, and TKK Pt/C.

Name	**Initial $E_{1/2}$ (V)**	**After 30k cycles $E_{1/2}$ (V)**
Pt_3Ni_5MoN/C	0.960	0.930
Pt_3Ni_3MoN/C	0.950	0.930
Pt_3NiMoN/C	0.945	0.935
TKK Pt/C	0.94	0.900

Table 3.4 Mass activities for the prepared samples at 0.9 V.

Name	**Initial ($mA.mg^{-1}Pt$)**	**10k cycles ($mA.mg^{-1}Pt$)**	**20k cycles ($mA.mg^{-1}Pt$)**	**30k cycles ($mA.mg^{-1}Pt$)**
Pt_3Ni_5MoN/C	1700	980	850	750
Pt_3Ni_3MoN/C	900	750	690	670
Pt_3NiMoN/C	450	430	370	356
TKK Pt/C	240	200	170	105

Clearly, the catalytic activity improved with the decrease of Pt content in a certain range, while their stability sharply decreases. In general, the fast degradation of catalytic activity occurs in the initial stage at the ADT, mainly due to the high surface energy of the small alloy nanoparticles, facile to causing the Ostwald ripening and agglomeration (Figure 3.4b).[34] In addition, during the long-term test of the electrocatalyst, especially after the 30k CV cycles test, the Ni atoms and/or its nitrides are inevitably dissolved in acidic solution, especially in electrochemical environmental conditions. These behaviors will lead to the decrease of ECSA (Figure 3.9b) and a change of electronic structure of metal particles, and thus affect the catalytic activity. Specifically, the initial MA of Pt_3Ni_5MoN/C is up to 1,700 mA mg^{-1} Pt, while decreased by 56% after 30k cycles durability tests. It is possible that a small amount of platinum cannot protect nickel in the alloy during the long-term stability

UNIVERSITY of the WESTERN CAPE

http://etd.uwc.ac.za/

test, which tends to dissolve in acids. Although Pt_3NiMoN/C decays only by 20% after 30k cycles, the lower atomic utilization of Pt leads to the poor catalytic activity. Consequently, an appropriate Pt content in the nanoparticles can not only prevent Ni atoms losing in the long-term activity of the electrocatalyst, but also improve the utilization rate of platinum atoms and thus improve the catalytic performance.

3.4 Conclusion

In this work, nitrogen-doped PtNiMo ternary alloys were synthesized by impregnation reduction followed by annealing at high temperatures. The introduction of acid-resistant Mo atoms in the alloy not only stabilizes the near-surface Pt atoms, enhancing the catalytic stability, but also changes the electronic structure of adjacent Pt atoms and thus promote the desorption of oxide intermediates. The doped N can form Ni_4N with Ni at high temperature and is stabilized in the electrocatalyst to thus improve stability. Furthermore, the pyridine N and pyrrole N can also be treated by annealing the carbon substrate in an NH_3 atmosphere. It has been confirmed that they possess a promoting effect on oxygen reduction. By adjusting the near-surface Pt atom's content to balance the activity and stability, Pt_3Ni_3MoN/C shows the best activity and stability. Its initial activity is 3.75 times than that of commercial Pt/C. In addition, after 30k accelerated durability tests the activity still remains 75%. This electrocatalyst with good activity and stability is simple to manufacture and can be produced on large scale, thus providing a new potential possibility for the commercialization of PEMFCs.

UNIVERSITY of the
WESTERN CAPE
http://etd.uwc.ac.za/

3.5 References

1. Ding X, Yin SB, An K, Luo L, Shi N, Qiang YH, Pasupathi S, Pollet BG, Shen PK. FeN stabilized FeN@Pt core-shell nanostructures for oxygen reduction reaction. *J. Mater. Chem. A*, 2015, 3(8), 4462-4469.
2. Gatalo M, Bele M, Ruiz-Zepeda F, Sest E, Sala M, Kamsek AR, Maselj N, Galun T, Hodnik N, Gaberscek M. A double-passivation water-based galvanic displacement method for reproducible gram-scale production of high-performance platinum-alloy electrocatalysts. *Angew. Chem., Int. Ed.*, 2019, 58(38), 13266-13270.
3. Wang DL, Xin HL, Hovden R, Wang HS, Yu YC, Muller DA, Disalvo FJ, Abruna HD. Structurally ordered intermetallic platinum-cobalt core-shell nanoparticles with enhanced activity and stability as oxygen reduction electrocatalysts. *Nat. Mater.*, 2013, 12(1), 81-87.
4. Debe MK. Electrocatalyst approaches and challenges for automotive fuel cells. *Nature*, 2012, 486(7401), 43-51.
5. Stamenkovic VR, Fowler B, Mun BS, Wang GF, Ross PN, Lucas CA, Markovic NM. Improved oxygen reduction activity on $Pt_3Ni(111)$ via increased surface site availability. *Science*, 2007, 315(5811), 493-497.
6. Zheng Y, Li YF, Wu T, Zhao CH, Zhang WQ, Zhu JX, Li ZP, Chen J, Wang JC, Yu B, Zhang JJ. Controlling crystal orientation in multilayered heterostructures toward high electro-catalytic activity for oxygen reduction reaction. *Nano Energy*, 2019, 62, 521-529.
7. Zhu YM, Liu X, Jin SG, Chen HJ, Lee W, Liu ML, Chen Y. Anionic defect engineering of transition metal oxides for oxygen reduction and evolution reactions. *J. Mater. Chem. A*, 2019, 7(11), 5875-5897.
8. Xiong Y, Xiao L, Yang Y, Disalvo FJ, Abruna HD. High-loading intermetallic Pt_3Co/C core-shell nanoparticles as enhanced activity electrocatalysts toward the oxygen reduction reaction (ORR). *Chem. Mater.*, 2018, 30(5), 1532-1539.
9. Singh D, Mamtani K, Bruening CR, Miller JT, Ozkan US. Use of H_2S to probe the active sites in FeNC catalysts for the oxygen reduction reaction (ORR) in acidic media. *ACS Catal.*, 2014, 4(10), 3454-3462.

UNIVERSITY of the
WESTERN CAPE

http://etd.uwc.ac.za/

10. Gu DG, Ma RG, Zhou Y, Wang FF, Yan K, Liu QA, Wang JC. Synthesis of nitrogen-doped porous carbon spheres with improved porosity toward the electrocatalytic oxygen reduction. *ACS Sustainable Chem. Eng.*, 2017, 5(11), 11105-11116.
11. Niu ZQ, Becknell N, Yu Y, Kim D, Chen C, Kornienko N, Somorjai GA, Yang PD. Anisotropic phase segregation and migration of Pt in nanocrystals en route to nanoframe catalysts. *Nat. Mater.*, 2016, 15(11), 1188-1194.
12. Luo SP, Tang M, Shen PK, Ye SY. Atomic-scale preparation of octopod nanoframes with high-index facets as highly active and stable catalysts. *Adv. Mater.*, 2017, 29(8), 1601687.
13. Wang K, Sriphathoorat R, Luo SP, Tang M, Du HY, Shen PK. Ultrathin PtCu hexapod nanocrystals with enhanced catalytic performance for electro-oxidation reactions. *J. Mater. Chem. A*, 2016, 4(35), 13425-13430.
14. Ma YB, Miao LQ, Guo WH, Yao XZ, Qin F, Wang ZX, Du HD, Li J, Kang FY, Gan L. Modulating surface composition and oxygen reduction reaction activities of Pt-Ni octahedral nanoparticles by microwave-enhanced surface diffusion during solvothermal synthesis. *Chem. Mater.*, 2018, 30(13), 4355-4360.
15. Yang JH, Yang J, Ying JY. Morphology and lateral strain control of Pt nanoparticles via core-shell construction using alloy AgPd core toward oxygen reduction reaction. *ACS Nano*, 2012, 6(11), 9373-9382.
16. Xu H, Ni K, Li XK, Zhu S, Fan GH. Comparative studies of leached Pt-Fe and Pt-Co catalysts for CO oxidation reactions. *Chin. J. Catal.*, 2017, 38(7), 1261-1269.
17. Wang DL, Yu YC, Xin HL, Hovden R, Ercius P, Mundy JA, Chen H, Richard JH, Muller DA, Disalvo FJ, Abruna HD. Tuning oxygen reduction reaction activity via controllable dealloying: A model study of ordered Cu_3Pt/C intermetallic nanocatalysts. *Nano Lett.*, 2012, 12(10), 5230-5238.
18. Stamenkovic VR, Mun BS, Mayrhofer KJJ, Ross PN, Markovic NM. Effect of surface composition on electronic structure, stability, and electrocatalytic properties of Pt-transition metal alloys: Pt-skin versus Pt-skeleton surfaces. *J. Am. Chem. Soc.*, 2006, 128(27), 8813-8819.

UNIVERSITY of the
WESTERN CAPE

http://etd.uwc.ac.za/

19. Hu YJ, Wu P, Yin YJ, Zhang H, Cai CX. Effects of structure, composition, and carbon support properties on the electrocatalytic activity of Pt-Ni-graphene nanocatalysts for the methanol oxidation. *Appl. Catal., B*, 2012, 111, 208-217.
20. Liu ML, Zhao ZP, Duan XF, Huang Y. Nanoscale structure design for high-performance Pt-Based ORR catalysts. *Adv. Mater.*, 2019, 31(6), 1802234.
21. Shao M, Chang Q, Dodelet JP, Chenitz R. Recent advances in electrocatalysts for oxygen reduction reaction. *Chem. Rev.*, 2016, 116(6), 3594-657.
22. Cao BF, Neuefeind JC, Adzic RR, Khalifah PG. Molybdenum nitrides as oxygen reduction reaction catalysts: Structural and electrochemical studies. *Inorg. Chem.*, 2015, 54(5), 2128-2136.
23. Hu Y, Jensen JO, Zhang W, Cleemann LN, Xing W, Bjerrum NJ, Li QF. Hollow spheres of iron carbide nanoparticles encased in graphitic layers as oxygen reduction catalysts. *Angew. Chem., Int. Ed.*, 2014, 53(14), 3675-3679.
24. Kuttiyiel KA, Sasaki K, Choi Y, Su D, Liu P, Adzic RR. Nitride stabilized PtNi core-shell nanocatalyst for high oxygen reduction activity. *Nano Lett.*, 2012, 12(12), 6266-6271.
25. Jia QY, Zhao ZP, Cao L, Li JK, Ghoshal S, Davies V, Stavitski E, Attenkofer K, Liu ZY, Li MF, Duan XF, Mukerjee S, Mueller T, Huang Y. Roles of Mo surface dopants in enhancing the ORR performance of octahedral PtNi nanoparticles. *Nano Lett.*, 2018, 18(2), 798-804.
26. Huang XQ, Zhao ZP, Cao L, Chen Y, Zhu EB, Lin ZY, Li MF, Yan AM, Zettl A, Wang YM, Duan XF, Mueller T, Huang Y. High-performance transition metal-doped Pt_3Ni octahedra for oxygen reduction reaction. *Science*, 2015, 348(6240), 1230-1234.
27. Jing SY, Luo L, Yin SB, Huang F, Jia Y, Wei Y, Sun ZH, Zhao YM. Tungsten nitride decorated carbon nanotubes hybrid as efficient catalyst supports for oxygen reduction reaction. *Appl. Catal., B*, 2014, 147, 897-903.
28. Lu QY, Yang B, Zhuang L, Lu JT. Pattern recognition on the structure-activity relationship of nano Pt-Ru catalysts: Methodology and preliminary demonstration. *J. Phys. Chem. B*, 2005, 109(18), 8873-8879.

UNIVERSITY of the
WESTERN CAPE

http://etd.uwc.ac.za/

29. Shen XC, Dai S, Pan YB, Yao LB, Yang JL, Pan XQ, Zeng J, Peng ZM. Tuning electronic structure and lattice diffusion barrier of ternary Pt–In–Ni for both improved activity and stability properties in oxygen reduction electrocatalysis. *ACS Catal.*, 2019, 9(12), 11431-11437.
30. Strasser P, Koh S, Anniyev T, Greeley J, More K, Yu CF, Liu ZC, Kaya S, Nordlund D, Ogasawara H, Toney MF, Nilsson A. Lattice-strain control of the activity in dealloyed core-shell fuel cell catalysts. *Nat. Chem.*, 2010, 2(6), 454-460.
31. Ando T, Izhar S, Tominaga H, Nagai M. Ammonia-treated carbon-supported cobalt tungsten as fuel cell cathode catalyst. *Electrochim. Acta*, 2010, 55(8), 2614-2621.
32. Liu J, Lan JZ, Yang LY, Wang F, Yin J. PtM (M = Fe, Co, Ni) bimetallic nanoclusters as active, methanol-tolerant, and stable catalysts toward the oxygen reduction reaction. *ACS Sustainable Chem. Eng.*, 2019, 7(7), 6541-6549.
33. Chisaka M. Creation of oxygen reduction reaction active sites on titanium oxynitride without increasing the nitrogen doping level. *Phys. Chem. Chem. Phys.*, 2018, 20(23), 15613-15617.
34. Choi DS, Robertson AW, Warner JH, Kim SO, Kim H. Low-temperature chemical vapor deposition synthesis of Pt-Co alloyed nanoparticles with enhanced oxygen reduction reaction catalysis. *Adv. Mater.*, 2016, 28(33), 7115-7122.
35. Liu Y, Wen C, Guo Y, Lu GZ, Wang YQ. Modulated CO oxidation activity of M-doped ceria (M = Cu, Ti, Zr, and Tb): Role of the pauling electronegativity of M. *J. Phys. Chem. C*, 2010, 114(21), 9889-9897.
36. Zhao YG, Liu JJ, Zhao YH, Wang F. Composition-controlled synthesis of carbon-supported Pt-Co alloy nanoparticles and the origin of their ORR activity enhancement. *Phys. Chem. Chem. Phys.*, 2014, 16(36), 19298-19306.
37. Dionigi F, Weber CC, Primbs M, Gocyla M, Bonastre AM, Spori C, Schmies H, Hornberger E, Kuhl S, Drnec J, Heggen M, Sharman J, Dunin-Borkowski RE, Strasser P. Controlling near-surface Ni composition in octahedral PtNi(Mo) nanoparticles by Mo doping for a highly active oxygen reduction reaction catalyst. *Nano Lett.*, 2019, 19(10), 6876-6885.

UNIVERSITY of the
WESTERN CAPE

http://etd.uwc.ac.za/

CHAPTER 4 Investigation of Cu_2S-Cu_3P Nanowire Arrays Self-Supported on Copper Foam for HER

This chapter focuses on the studying of the Cu_2S-Cu_3P nanowire arrays self-supported on copper foam as efficient electrocatalysts for hydrogen evolution, and the corresponding mechanism for hydrogen evolution discussed. The work in this chapter comes from an article from the author entitled "S, P co-doped Cu nanowire arrays as boosting electrocatalysts for hydrogen evolution, *Energy Technology*, 2019, 1800993, DOI: 10.1002/ente.201800993".

4.1 Introduction

Hydrogen with clean and sustainable properties is an ideal source of energy and is not considered to produce any greenhouse gases.[1] Conventional industrial hydrogen steam reforming processes still consume fossil fuels and produce low purity hydrogen.[2] In contrast, electrolyzed water is considered to be a simple and effective method for hydrogen production.[3] Noble metals (e.g. platinum group) with high activity for hydrogen evolution, suffer from their relative rarity and high cost of production, limits their wider application.[4, 5] Many efforts have been undertaken to search for more low-cost and efficient non-precious metal electrocatalysts.[6]

Cu is one of the most abundant elements found in the earth. In recent years, Cu-based electrocatalysts have emerged as potentially low-cost and efficient candidates for hydrogen evolution reaction (HER). Transition metal chalcogenides (TMCs) have been extensively studied as HER electrocatalysts for their lower prices and noble-metal-

UNIVERSITY of the WESTERN CAPE

http://etd.uwc.ac.za/

like electronic structures.[7] Copper sulfides have been additionally found to possess potential applications in water splitting.[8] It has subsequently been proved that the unsaturated sulfur atoms on the edges of the exposed surface, possessed more rapid electron transfer pathways, smaller optical band gaps and thus had better redox reactions which play a crucial role in HER.[9] In addition, copper sulfide has a unique anisotropic structure that provides a large number of permeation channels for the diffusion of electrolytes.[10] Due to these intrinsic superior attributes, copper sulfides may thus be considered suitable for hydrogen evolution.

On the other hand, transition-metal phosphides (TMPs), including Ni_2P,[11] CoP,[12] and FeP[13] are also important for their low electrical resistance and have been intensively studied as electrocatalysts. As a semiconducting (p-type) material,[14] Cu_3P nanowires and nanotubes possessing good conductivity, have been successfully applied in electrocatalytic H_2 generation. Hou *et al*. reported on the cedar-like Cu_3P nanoarrays, which possessing a large roughness factor which resulted in a high electrochemical active surface area, while the Cu_3P core character facilitated charge transfer.[15] However, further investigations are required to improve its performance in order to meet the needs for practical applications. In the past, double element doped material has proved to be more competitive than single element doped material in terms of electrocatalysts. Patel *et al*. proved that P and S heteroatom synergism of carbon could lower the activation energy for the benzyl alcohol oxidation reaction and showed better catalytic performance than the only P-doped carbon electrocatalyst.[16] Dou *et al*. found that S and P co-doped atoms not only

UNIVERSITY of the
WESTERN CAPE
http://etd.uwc.ac.za/

destroyed the electron permeability of sp^2 carbon in graphene and enhanced the electrocatalytic activity for oxygen reduction, but also interacted with each other to provide favorable synergetic effects of S and P.[17]

Furthermore, during the electrochemical measurements and practical applications, binders such as Nafion and PTFE are needed to immobilize the electrocatalysts on the surface of electrodes. This in turn, may block the active sites and thereby inhibit mass diffusion which would result in a decrease in catalytic efficiency. The self-supported nanowire arrays electrode without any binder will favor the active material to grow directly on the current collector which might address this problem. In addition, the nanoarray structures with a large specific surface area will expose more active sites and promote mass diffusion which is beneficial for the adsorption and transport of reactive substances and products.[18] Furthermore, the self-supported structure will prevent the electrocatalysts dissolving during the long-term electrocatalysis, which would improve the electrochemical stability of active substances. In combination with the self-supported electrode strategy, the synergistic effect of S and P will potentially be more advantageous in electrocatalytic activity. To date, Cu_2S-Cu_3P nanowire arrays with self-supported structure have seldom been reported.

This work describes the fabrication of self-supported Cu_2S-Cu_3P nanowire (Cu_2S-Cu_3P NW) arrays on commercial copper foam to form $Cu(OH)_2$ NW arrays by liquid-solid reaction and subsequent phosphidation at low temperature. Subsequently, the optimized Cu_2S-Cu_3P NW arrays electrode was investigated for HER, where it demonstrated excellent HER catalytic performance in 1.0 M KOH solution

UNIVERSITY of the WESTERN CAPE

http://etd.uwc.ac.za/

comparable or even superior to the other reported non-noble metal-based HER electrocatalysts under similar conditions.

4.2 Experimental

4.2.1 Materials

All chemicals are analytical grade and used without further purification. NaH_2PO_2, NaOH, $(NH_4)_2S_2O_8$, $Na_2S{\cdot}9H_2O$, copper foam (CF, 1.6 mm) were purchased from Shanghai Macklin Biochemical Co., Ltd. The Cu_2S-Cu_3P NW arrays on copper foam are fabricated by a simple liquid-solid reaction and subsequent phosphidation at low temperature and are illustrated in Scheme 4.1.

4.2.2 Synthesis of $Cu(OH)_2$ NW Arrays

First, $Cu(OH)_2$ NW arrays are prepared by a simple liquid-solid reaction.[19] Typically, copper foam (1 cm × 2 cm) was washed with acetone and deionized water several times, then immersed in an aqueous solution of NaOH (5.0 M), $(NH_4)_2S_2O_8$ (0.13 M), and H_2O (50 mL). After being maintained at 25 °C for 40 min in a water bath, it was rinsed with water, dried in air and produced a light-blue film, described as $Cu(OH)_2$ NW arrays.

4.2.3 Synthesis of Cu_2S-Cu_3P NW Arrays

The $Cu(OH)_2$ NW arrays were immersed in 5.0 M aqueous Na_2S solution at 25 °C for 2 h. Following on this, the arrays were washed several times with water and ethanol respectively and dried in a vacuum oven at 60 °C for 6 h to obtain Cu_2S NW

UNIVERSITY of the WESTERN CAPE
http://etd.uwc.ac.za/

arrays. The Cu_2S NW arrays and NaH_2PO_2 (0.04 g) were placed at the center of a tube furnace and heated to 300 °C with a ramping rate of 2 °C min^{-1} and kept for 60 min under N_2. After natural cooling to room temperature, the resulting black Cu_2S-Cu_3P NW arrays were obtained. Similarly, the separate Cu_2S NW arrays and Cu_3P NW arrays were synthesized under similar conditions. Specifically, the Cu_2S NW arrays were prepared without phosphidation, and Cu_3P NW arrays were prepared without sulfuration.

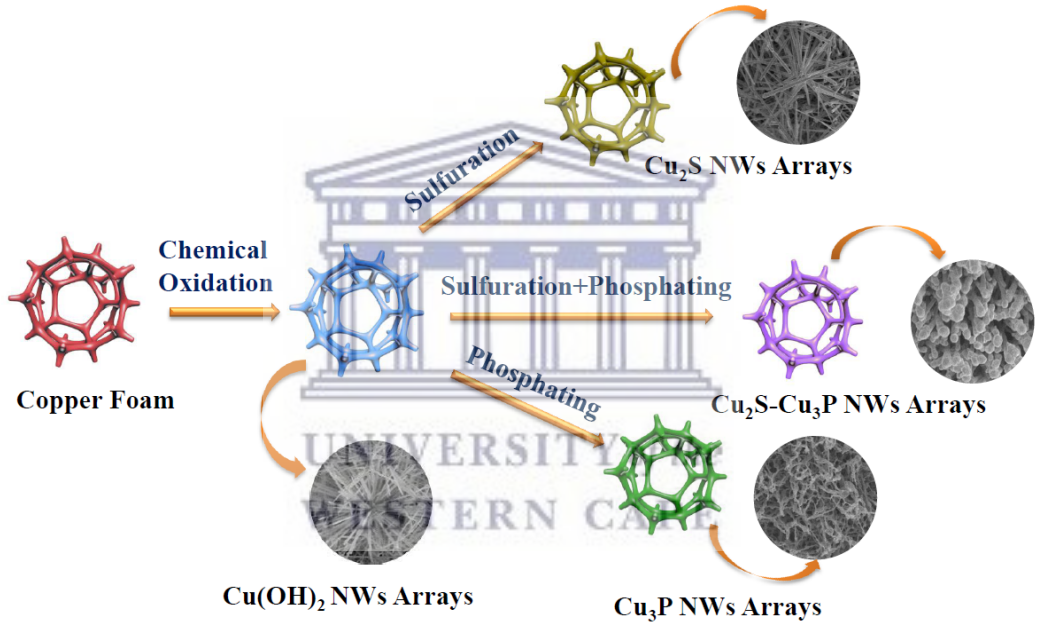

Scheme 4.1 Schematic illustration of the synthesis of Cu_2S-Cu_3P NW arrays on copper foam.

4.2.4 Physico-Chemical Characterization

X-ray powder diffraction (XRD) spectra were obtained using a SmartLab X-ray diffractometer (Rigaku Corp., Japan) employing Cu Kα (1.5406 Å) radiation at 40 kV and 30 mA with a scan rate of 10° min^{-1}. X-ray photoelectron spectroscopy (XPS) measurements were performed on an ESCALAB 250 Xi (ThermoFisher Scientific,

http://etd.uwc.ac.za/

USA) using Al as the exciting source. Scanning electron microscopy (SEM) and X-ray (EDX) images were obtained with a FESEM SU8220 (Hitachi Corp., Japan) operated at 5.0 kV and 10 kV respectively. Transmission electron microscopy (TEM) and HRTEM images were obtained on a Titan ETEM G^2 80-300 (FEI Co., USA) with an accelerating voltage of 200 kV.

All the electrochemical measurements were executed through a standard three-electrode setup (Zahner IM6e, Germany) in 1.0 M KOH aqueous solution. The as-prepared samples were used as working electrodes; a reversible hydrogen electrode (RHE) and a graphite rod were used as reference electrode and counter electrode, respectively. The electrochemical tests were performed by the cyclic voltammetry (CV) method at a scan rate of 10 mV s^{-1} (degassed continuously by N_2 to maintain saturation) after initial stabilization of activities. The electrochemical impedance spectroscopy (EIS) measurements were obtained at frequencies ranging from 100 KHz to 100 Mz. The long-term stability of Cu_2S-Cu_3P NW arrays were determined by the chronoamperometry (CA) method at –10 mA cm^{-2} in 1.0 M KOH aqueous solutions for 75 h. The Tafel plots were calculated by using the Tafel equation: $\eta = a + b \log(j)$, where j is the current density, a is the Tafel constant, and b is the Tafel slope. All electrochemical measurements were carried out at 25 °C, and the current density was normalized by geometric area in this work.

UNIVERSITY of the
WESTERN CAPE

http://etd.uwc.ac.za/

4.3 Results and Discussions

XRD curves of Cu_2S-Cu_3P NW arrays shown in Figure 4.1 illustrate curves of contrasting samples. The peaks at 43.3°, 50.4°, and 74.1° can be ascribed to the copper foam substrate (JCPDS No.70-3039). The patterns illustrate that the $Cu(OH)_2$ NW arrays have five distinct diffraction peaks, which are (020), (021), (002), (130) and (132) for the orthorhombic phase of $Cu(OH)_2$ (Figure 4.1b). After sulfuration, the characteristic peaks can be readily identified into the Cu_2S samples (JCPDS No.89-2670) in Figure 4.1c. As the $Cu(OH)_2$ NW arrays precursor is phosphated (Figure 4.1d), the peaks at 36.0°, 39.0°, 41.5°, 45.1° and 46.1°, corresponding to the (112), (202), (211), (300), and (113) of Cu_3P, represents the hexagonal phase Cu_3P (JCPDS No. 71-2261). In Figure 4.1a, obviously, the Cu_2S-Cu_3P NW arrays display the characteristic diffraction peaks of Cu_2S and Cu_3P, indicating the obtained products are co-doped by sulfur and phosphor.

UNIVERSITY of the
WESTERN CAPE

http://etd.uwc.ac.za/

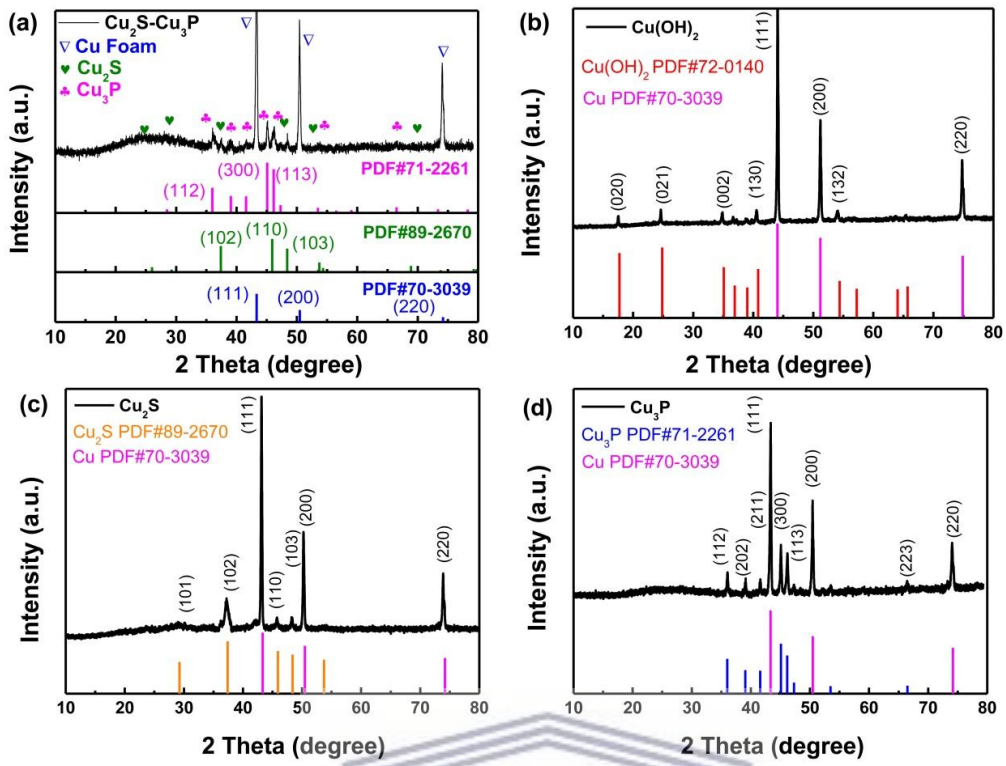

Figure 4.1 XRD curves of the samples with a scan rate of 10° min^{-1}. (a) Cu_2S-Cu_3P NW arrays. (b) $Cu(OH)_2$ NW arrays, (c) Cu_2S NW arrays, (d) Cu_3P NW arrays.

UNIVERSITY of the
WESTERN CAPE

XPS was conducted to further characterize the compositions and surface states of these samples. Clearly, the XPS for Cu_2S illustrates the signals of Cu, S, C, and O elements without impurities (Figure 4.2a). Oxygen appears in all the samples due to the nature of nanomaterials which are easily oxidized when exposed in air.[20] For Cu2p (Figure 4.2b), the peaks at 932.6 and 952.5 eV are ascribed to the $Cu2p_{3/2}$ and $Cu2p_{1/2}$.[21] Two satellite peaks centered at 941.2 and 944.2 eV indicates the presence of the paramagnetic chemical state of Cu^{2+}.[22] There are two characteristic peaks of S2p at 161.85 and 163 eV (Figure 4.2c). Specifically, the peak at 161.85 eV is due to the single sulfur atom bonded with copper while the second peak at 163 eV indicates the binding energy of S2p in the S-S bond.[23] These two peaks of $S2p_{3/2}$

http://etd.uwc.ac.za/

proved that there are two types of sulfur atoms in the Cu_2S crystals, further confirming the successful synthesis of the Cu_2S compound.

After phosphation, the $Cu2p_{3/2}$ and $Cu2p_{1/2}$ peaks shift to 932.75 and 952.55 eV, respectively, which are consistent with the appearance of Cu_3P NW arrays (Figure 4.2d, e). The P2p region (Figure 4.2f) shows two peaks at 129.3 and 130.95 eV, reflecting the binding energy of $P2p_{3/2}$ and $P2p_{1/2}$. The binding energy of 129.3 eV ($P2p_{3/2}$) is due to Cu_3P, the peak at 130.95 eV can be assigned to the phosphorus signal that emanates from the P-Cu bond, while the peak at 133.25 eV is ascribed to oxidized phosphorus species.[24]

UNIVERSITY of the
WESTERN CAPE

http://etd.uwc.ac.za/

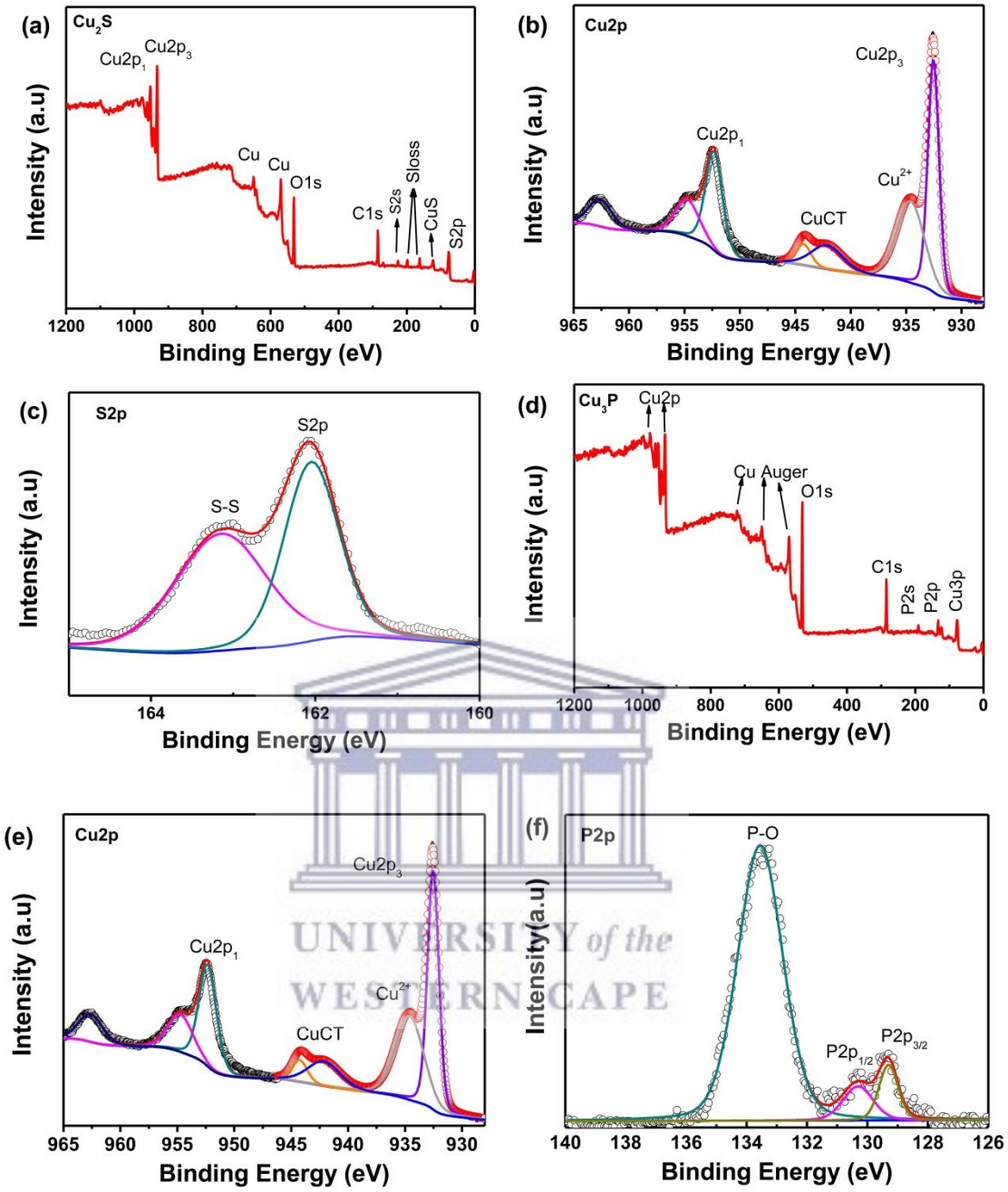

Figure 4.2 (a) XPS summary of Cu_2S NW arrays, the corresponding (b) Cu2p and (c) S2p; (d) XPS summary of Cu_3P NW arrays, the corresponding (e) Cu2p and (f) P2p.

http://etd.uwc.ac.za/

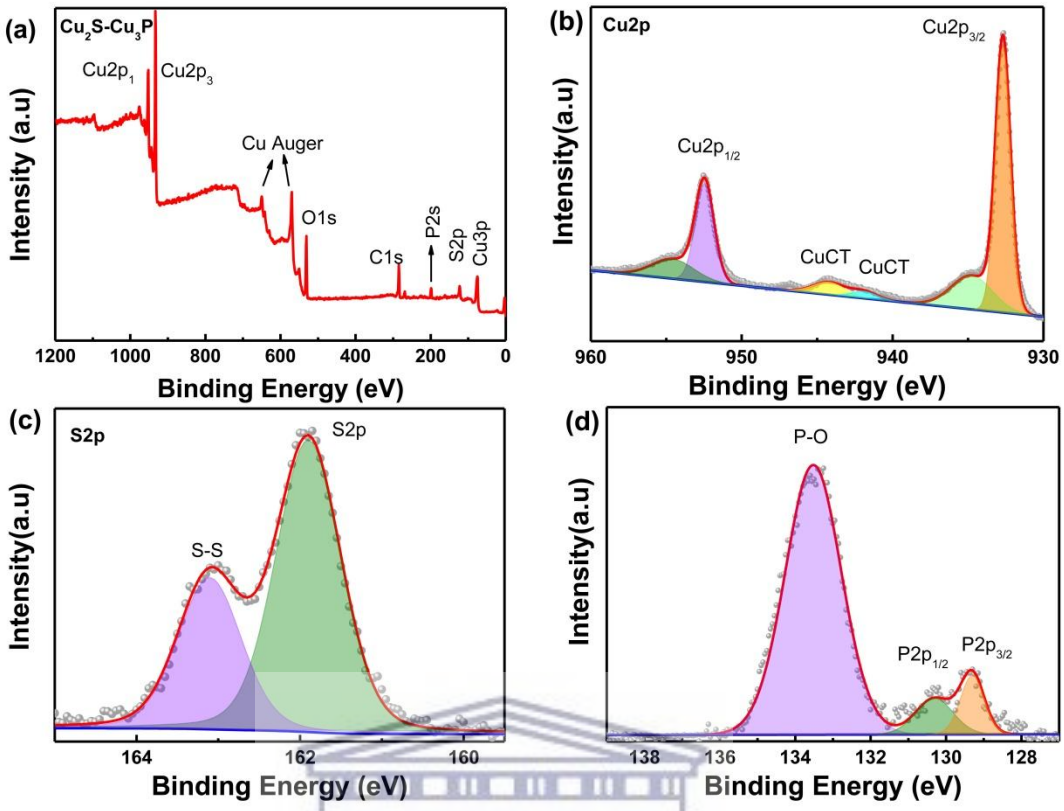

Figure 4.3 (a) XPS summary of Cu_2S-Cu_3P NW arrays, the corresponding (b) Cu2p, (c) S2p and (d) P2p.

UNIVERSITY of the
WESTERN CAPE

The spectra of the Cu_2S-Cu_3P NW arrays show two resolved peaks at 162.2 and 130.95 eV which are assigned to S-Cu and P-Cu species, respectively (Figure 4.3a). For Cu_2S-Cu_3P NW arrays, as compared with Cu_2S and Cu_3P NW arrays, the $Cu2p_{3/2}$ and $Cu2p_{1/2}$ peaks shift to 932.65 and 952.55 eV; the S2p and S-S peaks shift to 162.2 and 163.05 eV; the $P2p_{3/2}$, $P2p_{1/2}$ and P-O peaks shift to 129.75, 130.95 and 134.65 eV, respectively (Figures 4.3b, c, d). Comparison of these results with literatures, allows one to conclude that the positively shifted Cu2p, S2p and P2p represents an electron transfer, indicating that the presence of sulfur and phosphor can greatly promote the water dissociation kinetics of the catalyst.[24] It furthermore suggests

http://etd.uwc.ac.za/

that Cu has a partial positive charge and the S and P have a partial negative charge, thereby implying a transfer of electron density from Cu to S and P.[25] The Cu and basic P, S can thus be considered to act as the hydride-acceptor and proton-acceptor centers, respectively, thus facilitating the hydrogen evolution.[26] Evidently, these results are consistent in confirming that the peaks of Cu_2S and Cu_3P are indeed due to co-doping with phosphide and sulfide.

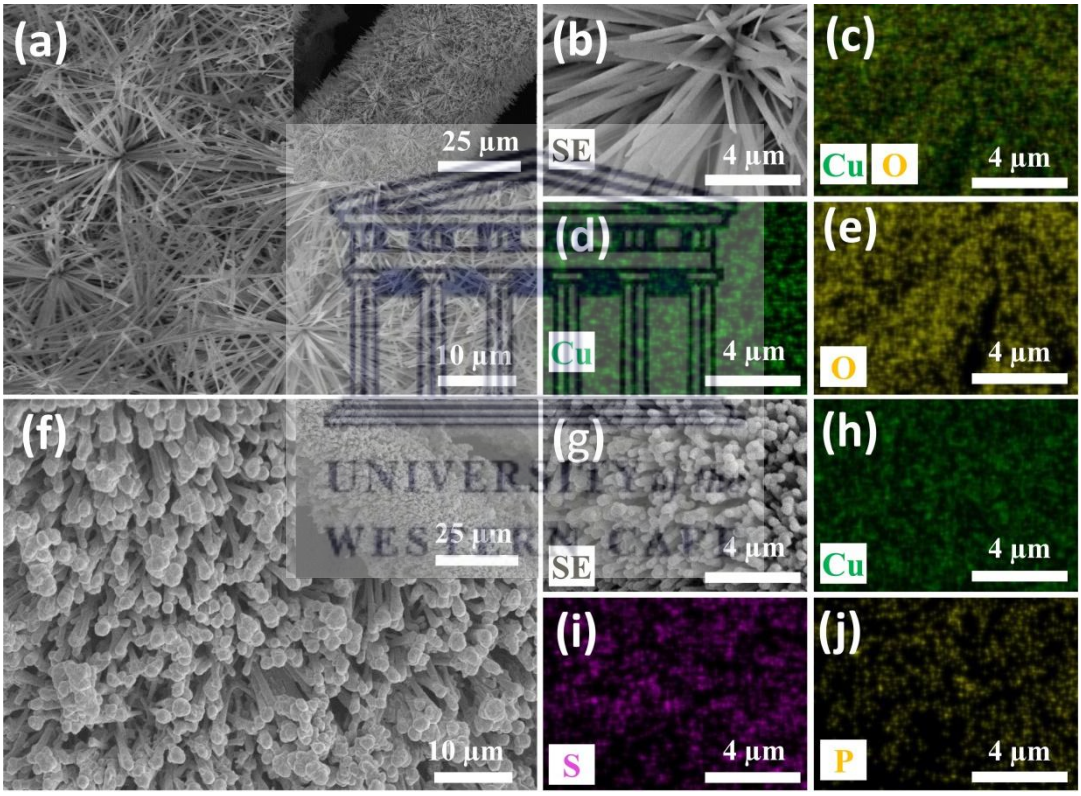

Figure 4.4 (a-e) SEM and EDS images of $Cu(OH)_2$ NW arrays, (f-j) SEM and EDS maps of Cu_2S-Cu_3P NW arrays.

The morphology and structure of the as-prepared samples were investigated by SEM. Apparently, the entire CF surfaces are uniformly covered with $Cu(OH)_2$ nanowires (Figure 4.4a), having a smooth morphology and growing almost vertically

http://etd.uwc.ac.za/

on CF with diameters of about 300~400 nm and thereby demonstrating a self-supported nanostructure. Hou *et al*. concluded that the interaction stress in the twisted octahedral $Cu(OH)_6$ layer causes the lamellar to form $Cu(OH)_2$ nanoribbons under alkaline conditions.[27] In this study, the formation of $Cu(OH)_2$ NW arrays on CF may follow a similar growth mechanism.

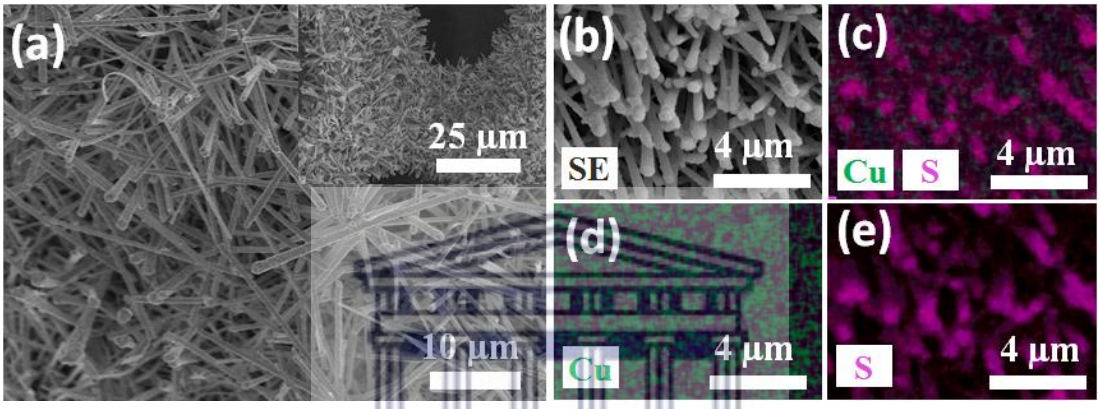

Figure 4.5 SEM and EDS images of Cu2S NW arrays.

UNIVERSITY of the
WESTERN CAPE

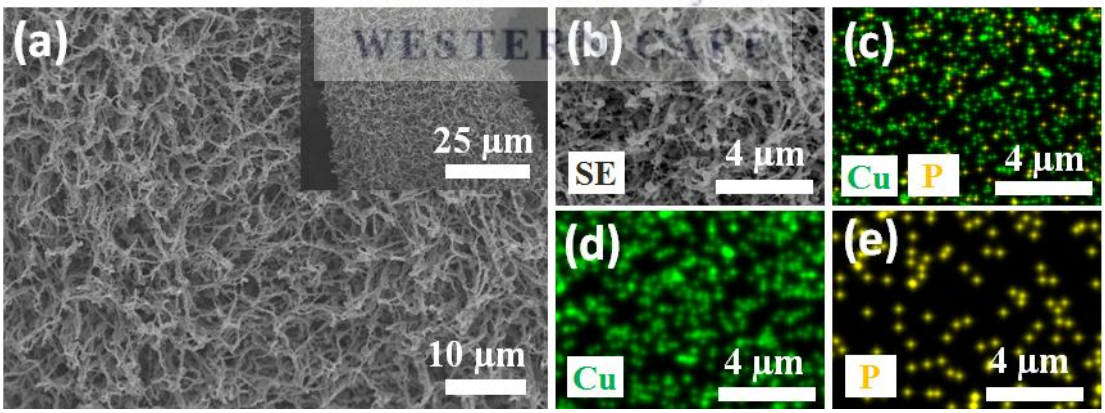

Figure 4.6 SEM and EDS pictures of Cu_3P NW arrays.

Figures 4.4 f-j shows the SEM images of $Cu(OH)_2$ NW arrays after phosphation and sulfuration. The energy dispersive X-ray (EDX) spectra of Cu_2S-Cu_3P NW arrays show that Cu, S and P are uniformly distributed. After co-doping with phosphide and

http://etd.uwc.ac.za/

sulphide, the Cu_2S-Cu_3P NW arrays show no obvious morphological changes, but form a relatively rougher surface with a coarser top similar to the sulfurated or phosphated samples (Figures 4.5, 4.6). The rough structures possibly result from the phosphide and sulphide doping effect as reported,[16] which will increase the specific surface area, facilitate mass transfer and consequently enhance the electrocatalytic activity. After sulfuration, the morphology is still very well preserved (Figures 4.5a, b). On the other hand, sulfuration causes the NW arrays to become slightly deformed with diameters being gradually increased to 0.3~1 μm, and a clear signal of sulfur can be detected in the EDX spectra of Cu_2S NW arrays (Figures 4.5c, e). This suggests that the morphology change occurs through an ion exchange between S^{2-} and OH^-. During the sulfuration process, the tips of needle-like $Cu(OH)_2$ nanowires react with newly supplied S^{2-}, while the bottoms of the nanowires react with diffusion-controlled S^{2-} at a relatively low concentration to form inverted cone-shaped padded nanowires.[28] The essential structure of the nanowires remained after phosphation (Figures 4.6a, c, d). All the nanowire arrays appear to be curled; the heads become larger formed self-assembled chains. The process of changing the $Cu(OH)_2$ NW arrays to Cu_3P NW arrays could be due to the thermal decomposition of NaH_2PO_2, the reduction of $Cu(OH)_2$ NW arrays by PH_3 gas to Cu NW arrays, then Cu catalyzed PH_3 decomposed into elemental phosphorous which reacted with Cu NW arrays to form the Cu_3P NW arrays.[29]

The TEM is used to further observe the morphological and structural properties of Cu_2S-Cu_3P NW arrays. As illustrated in Figure 4.7, the samples with a rough nanowire structure and having the Cu, S, and P evenly distributed in the entire nanowire (Figures 4.7e, f, g), confirm formation of Cu_2S and Cu_3P. High-resolution TEM images of Cu_2S-Cu_3P NW arrays (Figures 4.7b, c), illustrate a lattice spacing of

UNIVERSITY of the
WESTERN CAPE
http://etd.uwc.ac.za/

0.24 and 0.198 nm, corresponding to the (102) and (103) lattice planes of Cu_2S. The lattices with the *d*-spacing of 0.20, 0.217 and 0.292 nm are ascribed to the (300), (211) and (112) planes of Cu_3P,[25] respectively, and confirms the existence of Cu_3P. For transition metal sulfides and phosphides, the active sites of electrocatalysts depend on the quantity of S and P atoms on the exposed surface. Therefore, Cu_2S and Cu_3P on the highly exposed nanowire arrays can provide sufficient electrocatalytic active sites. Meanwhile, the Cu_2S-Cu_3P NW arrays are also favorable for mass diffusion and enhancing the electrocatalytic activity for hydrogen evolution.[30]

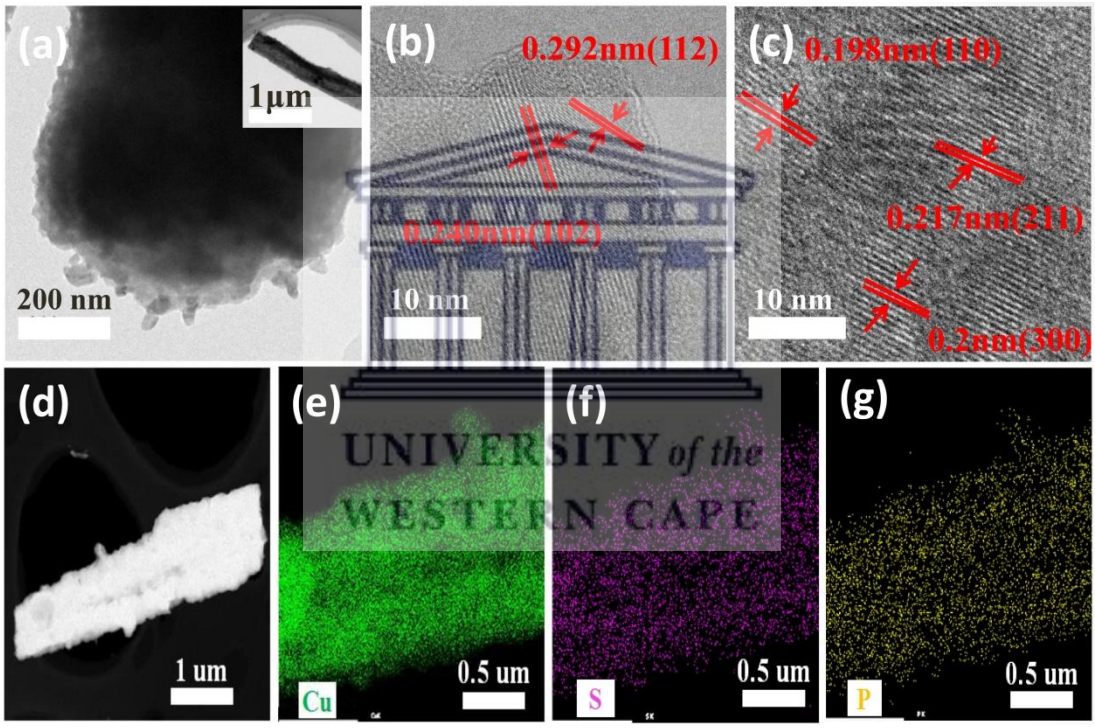

Figure 4.7 (a-c) TEM and HRTEM images of Cu_2S-Cu_3P NW arrays. (d-g) Dark field image and element mapping images of Cu, S and P.

The HER performance of the as-prepared catalysts and that of commercial 20 wt% Pt/C (JM) catalysts were comparatively evaluated in 1.0 M KOH at a scan rate of 10 mV s^{-1}. As seen in Figure 4.8a, Pt/C exhibits the lowest overpotential (η_{10}=33 mV, η_{100}=91 mV) in all the samples. In the remaining five samples, the Cu_2S-Cu_3P NW

http://etd.uwc.ac.za/

arrays exhibit the best catalytic activity for HER, with a small onset potential of 86 mV in alkaline solution. This value is smaller than that of CF (315 mV), $Cu(OH)_2$ (203 mV), Cu_2S (185 mV) and Cu_3P (170 mV). Furthermore, the overpotential at a current density of 10 mA cm^{-2} is another important parameter for water splitting.

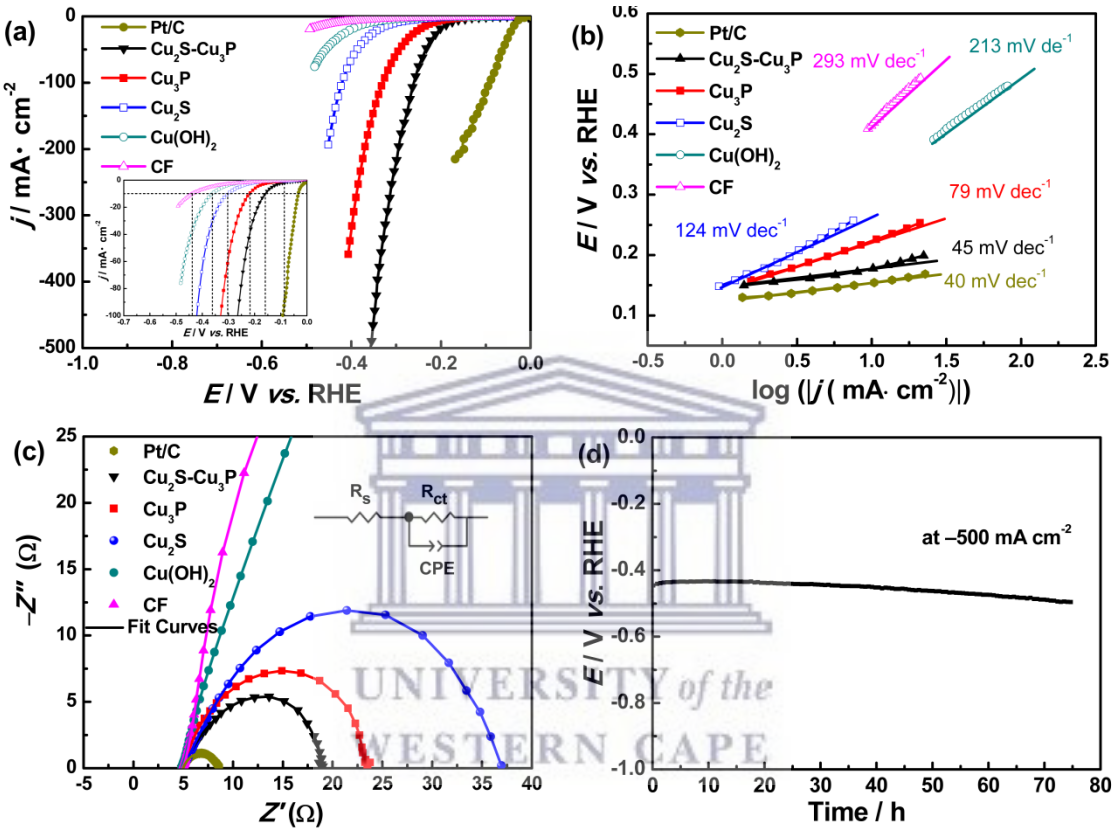

Figure 4.8 Electrochemical measurements of the samples for hydrogen evolution in 1.0 M KOH aqueous solution. (a, b) Polarization curves and the corresponding Tafel plots. (c) Nyquist plots in frequency values from 100 kHz to 100 mHz. (d) The chronopotentiometry curve of Cu_2S-Cu_3P NW arrays holding at –500 mA cm^{-2} for lasting 75 h.

This is ascribed to the fact that 10~20 mA cm^{-2} is usually operated by solar-light coupled HER apparatuses under standard conditions.[5] To achieve this current density, Cu_2S-Cu_3P requires an overpotential of 158 mV, while Cu_3P, Cu_2S, $Cu(OH)_2$, and CF require an overpotential of 217, 300, 361, 437 mV, respectively. Meanwhile,

http://etd.uwc.ac.za/

the cathodic current density increases rapidly with a more negative potential. Interestingly, the Cu_2S-Cu_3P NW arrays can produce a current density of 500 mA cm^{-2} with a potential of 355 mV, which means it possesses the best catalytic activity for hydrogen evolution. This value is much better than the recently reported non-noble metal based HER electrocatalysts, including some Cu-based sulfides and phosphates (Table 4.1).

Table 4.1 Comparison HER activities in 1.0 M KOH aqueous solution for Cu_2S-Cu_3P NW arrays with literatures recently reported.

Electrocatalysts	**Mass loading (mg cm^{-2})**	**Overpotential at 10 mA cm^{-2} (mV)**	**Tafel slope (mV dec^{-1})**	**References**
		HER	**HER**	
Cu_2S-Cu_3PNW/CF	—	**158**	**45**	**This work**
MoS_2/CuS	0.471	290	63	[1]
Cu_3P	0.64	266	107	[31]
graphene-coated Cu NWs	—	252	67	[32]
Cu_3P/CF	—	222	148	[33]
Cu_3P@C	—	203	83	[34]
Ag_2S/CuS	—	200	75	[35]
γ-Cu_2S/CF	—	190	98.9	[36]
Cu_3P/CC	2.05	189	96	[37]
CuS-Au	—	179	75	[38]
CuCo@NC	182	145	79	[39]
Cu_3P-450	—	130	83	[40]
NC/CuCo/$CuCoO_x$	1.5	112	55	[41]

Tafel plots were investigated (Figure 4.8b) to further characterize the HER activity. It was found that the linear portions of the polarization curves fitted well according to the Tafel equation. In line with the linear sweep voltammetry results, the Cu_2S-Cu_3P NW arrays electrode shows the lowest Tafel slope of 45 mV dec^{-1} among all the

UNIVERSITY of the WESTERN CAPE

http://etd.uwc.ac.za/

samples and is thus close to 20% commercial Pt/C (about 40 mV dec^{-1} in Figure 4.8b). The values for Cu_3P, Cu_2S, $Cu(OH)_2$, and CF are 79, 124, 213, and 293 mV dec^{-1}, respectively.

To further study the intrinsic properties of these samples, electrochemical impedance spectroscopy (EIS) was recorded in 0.1 M KOH to examine the catalytic kinetics. Nyquist plots of experimental and fitted data for all catalysts at −0.15 V, by the one-time constant model equivalent circuit, are illustrated in Figure 4.8c. The charge transfer resistance R_{ct} can be acquired by the semicircle of EIS and its lower value corresponds to faster kinetics.[42] Compared with the R_{ct} values of Pt/C (3.60 Ω), CF has the biggest charge transfer resistance of R_{ct} ~812.9 Ω, while R_{ct} for $Cu(OH)_2$ NW arrays is ~187.1 Ω. This is ascribed to its larger surface area as compared with bare CF. After sulfuration and phosphidation, Cu_2S NW arrays and Cu_3P NW arrays have R_{ct} values of ~33.6 and ~18.86 Ω respectively compared to that of Cu_2S-Cu_3P NW arrays which is 14.56 Ω, representing the smallest charge of resistance. This finding is thought to be due to the higher conductive surface resulting from co-doping by phosphor and sulfur which has a synergetic effect in Cu_2S-Cu_3P NW arrays that decreases the charge-transfer resistance at the electrocatalyst/electrolyte interface, fast electron-transfer rate which enhances the corresponding HER activity. In Figure 4.8c, the solution resistances used for *iR*-corrected are 4.98, 4.82, 4.01, 3.99, 4.23, and 4.93 Ω, respectively, corresponding to the Pt/C, Cu_2S-Cu_3P NW arrays, Cu_3P NW arrays, Cu_2S NW arrays, $Cu(OH)_2$ NW arrays and bare CF.

UNIVERSITY of the
WESTERN CAPE
http://etd.uwc.ac.za/

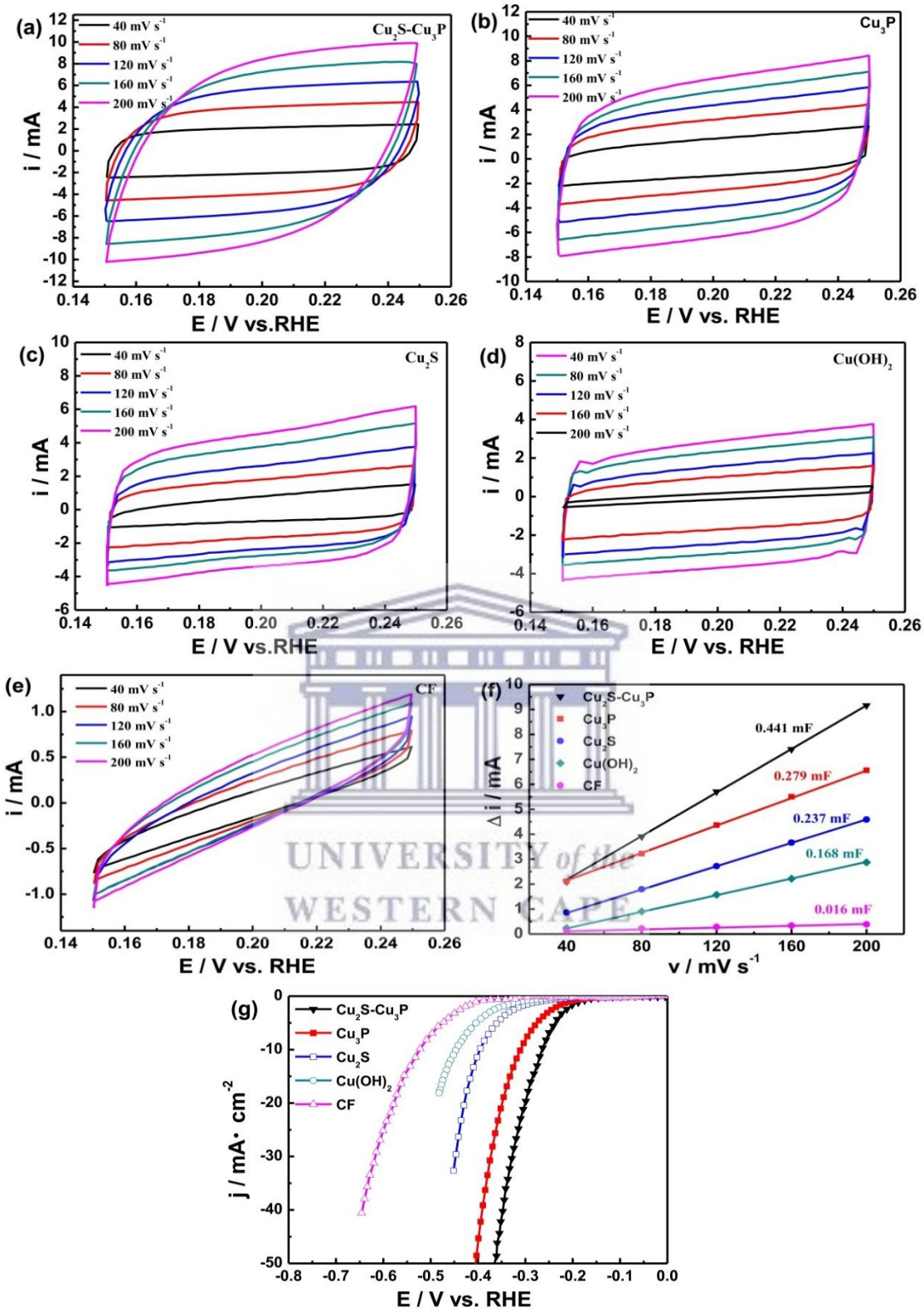

Figure 4.9 (a-e) Double-layer capacitance measurements for determining the electrochemically active surface area for all the electrocatalysts from voltammetry in 1.0 M KOH with different scan rates. (f) The capacitive currents at 0.20 V against the scan rate. (g) HER activities (current density) of the samples are normalized by their ESCA.

http://etd.uwc.ac.za/

To estimate the effective electrochemical surface areas (ECSA) of as-prepared samples, the capacitances of the double layer at the solid/liquid interface of both electrodes were measured. ECSA is proportional to the double-layer capacitance (C_{dl}), which can be calculated from different scan rate cyclic voltammogrames (CVs). In this work, CVs were determined in the region of 0.15~0.25 V, where the current response should be only due to the charging of the double layer (Figures 4.9 a-f). The capacitance of Cu_2S-Cu_3P NW arrays, Cu_3P NW arrays, Cu_2S NW arrays, $Cu(OH)_2$ NW arrays and CF is 44.1, 27.9, 23.7, 16.74 and 1.6 mF cm^{-2}, respectively, thus indicating Cu_2S-Cu_3P NW arrays have a much higher surface roughness than others.[43,44] The electrochemically active surface area of Cu_3P was approximately evaluated by using the electrochemical double-layer capacitance method. Moreover, according to the nitrogen adsorption/desorption isotherms (Figure 4.9g), the Brunauer–Emmett–Teller (BET) specific surface areas are found to be 5.83, 10.52 and 3.72 m^2 g^{-1} of the prepared samples viz., $Cu(OH)_2$, Cu_2S, Cu_3P and Cu_2S-Cu_3P respectively, which is furthermore consistent with the capacitance. Combined with the atomic contents of P and S obtained from XPS (Table 4.2), the percentage of sulfur and phosphorus obtained from the XPS was multiplied by the total surface atomic density to give the active site density (active atom g^{-1}) on the catalyst surface, compared with HER activity (Table 4.2). These results indicate that the high surface area can facilitate exposure of a large fraction of active edge sites, enlarging the contact area with the electrolyte and thus accelerating its

UNIVERSITY of the
WESTERN CAPE

http://etd.uwc.ac.za/

diffusion. These properties will favor excellent activity for electrocatalytic hydrogen evolution.[45]

Table 4.2 HER activity of different electrocatalysts.

Electrocatalysts	**Onset potential (mV)**	**Tafel slope (mV dec^{-1})**	**C_{DL} (mF)**	**ECSA (cm^2)**
Cu_2S-Cu_3P NW arrays	86	45	0.441	11.025
Cu_3P NW arrays	170	79	0.279	6.975
Cu_2S NW arrays	185	124	0.237	5.925
$Cu(OH)_2$ NW arrays	203	213	0.168	4.2
copper foam	315	293	0.016	0.4

Stability is also significant for any good HER electrocatalyst. Figure 4.8d illustrates the chronopotentiometry curve at a constant current density of –500 mA cm^{-2} in 1.0 M KOH aqueous solution. After 75 h of the accelerated durability test, no obvious decrease in the current density was observed in the HER performance. However, there was a slight degradation which could be due to the consumption of protons in the system and the hindrance of the reaction by hydrogen bubbles remaining on the self-supported structure of Cu_2S-Cu_3P NW arrays.[46] SEM characterization further shows that the Cu_2S-Cu_3P NW arrays were retained on the surface of CF without any detachment after the durability test. In addition, all the elements are homogeneously distributed on the prepared sample indicating an excellent structural stability in an alkaline environment (Figure 4.10).

UNIVERSITY of the
WESTERN CAPE

http://etd.uwc.ac.za/

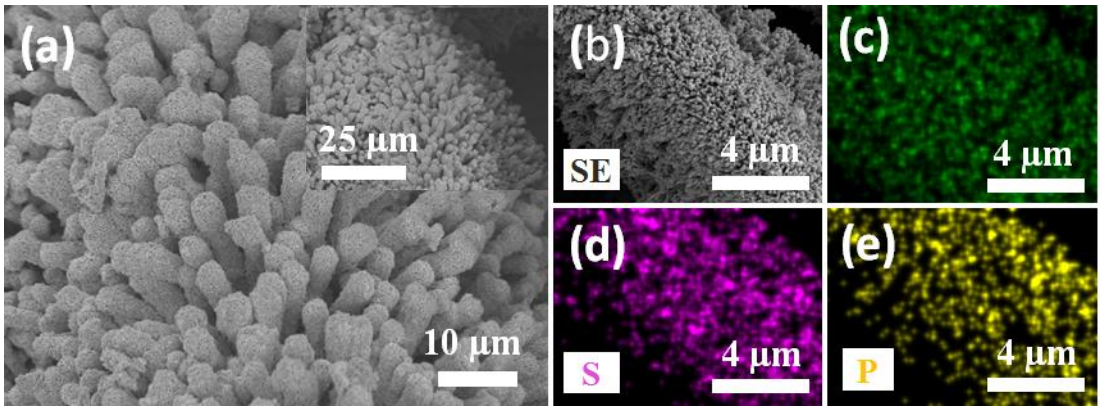

Figure 4.10 SEM and EDS pictures of Cu_2S-Cu_3P NW arrays after the stability test.

The excellent HER catalytic activity and stability of Cu_2S-Cu_3P NW arrays could be attributed to one or more of the following: a) direct integration of Cu_2S-Cu_3P NW arrays onto CF which reflects good mechanical adhesion and high conductivity and thus avoids use of a polymer binder to occupy the catalytic active sites, b) nanowires arrays not only allow fast electron transport (the good intrinsic electrical conductivity of Cu_2S, Cu_3P NW arrays favors fast electron transport along the nanowire), but also increases the catalyst load to further improve the catalytic efficiency, which could efficiently reduce the resistance of the electrode and provide more active sites, enlarge the specific surface area, facilitate mass diffusion and prevent the migration of active materials,[47-49] c) self-supported structures helps prevent dissolution during the long-term electrocatalysis and the synergetic effect between S and P could provide better stability.

UNIVERSITY of the
WESTERN CAPE

http://etd.uwc.ac.za/

4.4 Conclusions

Fabrication of self-supported Cu_2S-Cu_3P NW arrays on CF by liquid-solid reaction and subsequent phosphidation at low temperature can be used directly as an integrated electrode for HER. No binding agents are needed to favor excellent catalytic activity for HER and it only requires a low overpotential of 158 mV to achieve a current density of 10 mA cm^{-2} and furthermore displays a small Tafel slope of 45 mV dec^{-1}. In addition, the activity decrease is ignorable after holding at –500 mA cm^{-2} for a period of 75 h which demonstrates excellent stability.

Possible mechanisms include the unique Cu_2S-Cu_3P NW arrays structures which could efficiently reduce the resistance of the electrode, provide more active sites, enlarge the specific surface area, facilitate mass diffusion and transfer of electrons and prevent the migration of active materials. Considered together with the coexistence of S and P, a synergistic effect might result to further improve the electrochemical performance for hydrogen evolution in alkaline solutions. These results indicate that the as-prepared Cu-based nanowires arrays is a promising non-noble-metal electrocatalyst for hydrogen evolution and hopefully inspire a strong interest by others to develop analogous self-supported nanowires arrays with heteroatomic co-doped molecules as efficient electrocatalysts for hydrogen evolution.

UNIVERSITY of the
WESTERN CAPE

http://etd.uwc.ac.za/

4.5 References

1. Jing SY, Lu JJ, Yu GT, Yin SB, Luo L, Zhang ZS, Ma YF, Chen W, Shen PK. Carbon-encapsulated WO_x hybrids as efficient catalysts for hydrogen evolution. *Adv. Mater.*, 2018, 30(28), 1705979.
2. Wang F, Shifa TA, Zhan X, Huang Y, Liu K, Cheng Z, Jiang C, He J. Recent advances in transition-metal dichalcogenide based nanomaterials for water splitting. *Nanoscale*, 2015, 7(47), 19764-88.
3. Lu JJ, Zhang LS, Jing SY, Luo L, Yin SB. Remarkably efficient PtRh alloyed with nanoscale WC for hydrogen evolution in alkaline solution. *Int. J. Hydrogen Energy*, 2017, 42(9), 5993-5999.
4. Xu GR, Bai J, Yao L, Xue Q, Jiang JX, Zeng JH, Chen Y, Lee JM. Polyallylamine-functionalized platinum tripods: Enhancement of hydrogen evolution reaction by proton carriers. *ACS Catal.*, 2016, 7(1), 452-458.
5. Zhang LS, Lu JJ, Yin SB, Luo L, Jing SY, Brouzgou A, Chen JH, Shen PK, Tsiakaras P. One-pot synthesized boron-doped RhFe alloy with enhanced catalytic performance for hydrogen evolution reaction. *Appl. Catal., B*, 2018, 230, 58-64.
6. Han Y, Wang YG, Chen W, Xu R, Zheng L, Zhang J, Luo J, Shen RA, Zhu Y, Cheong WC, Chen C, Peng Q, Wang D, Li Y. Hollow N-doped carbon spheres with isolated cobalt single atomic sites: Superior electrocatalysts for oxygen reduction. *J. Am. Chem. Soc.*, 2017, 139(48), 17269-17272.
7. Huang J, Zhao S, Chen W, Zhou Y, Yang X, Zhu Y, Li C. Three-dimensionally grown thorn-like Cu nanowire arrays by fully electrochemical nanoengineering for highly enhanced hydrazine oxidation. *Nanoscale*, 2016, 8(11), 5810-4.
8. Yang L, Xie L, Ren X, Wang Z, Liu Z, Du G, Asiri AM, Yao Y, Sun X. Hierarchical $CuCo_2S_4$ nanoarrays for high-efficient and durable water oxidation electrocatalysis. *Chem. Commun.*, 2017, 54(1), 78-81.

UNIVERSITY of the
WESTERN CAPE

http://etd.uwc.ac.za/

9. Jaramillo TF, Jorgensen KP, Bonde J, Nielsen JH, Horch S, Chorkendorff I. Identification of active edge sites for electrochemical H_2 evolution from MoS_2 nanocatalysts. *Science*, 2007, 317(5834), 100-102.
10. Zhang XD, Xie Y. Recent advances in free-standing two-dimensional crystals with atomic thickness: Design, assembly and transfer strategies. *Chem. Soc. Rev.*, 2013, 42(21), 8187-8199.
11. Li Y, Cai P, Ci S, Wen Z. Strongly coupled 3D nanohybrids with Ni_2P/carbon nanosheets as pH-universal hydrogen evolution reaction electrocatalysts. *ChemElectroChem*, 2017, 4(2), 340-344.
12. Liu TT, Xie LS, Yang JH, Kong RM, Du G, Asiri AM, Sun XP, Chen L. Self-standing CoP nanosheets array: A three-dimensional bifunctional catalyst electrode for overall water splitting in both neutral and alkaline media. *Chemelectrochem*, 2017, 4(8), 1840-1845.
13. Guo XS, Feng ZJ, Lv Z, Bu Y, Liu QL, Zhao LQ, Hao CC, Li GC, Lei QQ. Formation of uniform FeP hollow microspheres assembled by nanosheets for efficient hydrogen evolution reaction. *ChemElectroChem*, 2017, 4(8), 2052-2058.
14. Manna G, Bose R, Pradhan N. Semiconducting and plasmonic copper phosphide platelets. *Angew. Chem., Int. Ed.*, 2013, 52(26), 6762-6766.
15. Hou CC, Chen QQ, Wang CJ, Liang F, Lin ZS, Fu WF, Chen Y. Self-supported cedarlike semimetallic Cu_3P nanoarrays as a 3D high-performance janus electrode for both oxygen and hydrogen evolution under basic conditions. *ACS Appl. Mater. Interfaces*, 2016, 8(35), 23037-23048.
16. Patel MA, Luo F, Savaram K, Kucheryavy P, Xie Q, Flach C, Mendelsohn R, Garfunkel E, Lockard JV, He HX. P and S dual-doped graphitic porous carbon for aerobic oxidation reactions: Enhanced catalytic activity and catalytic sites. *Carbon*, 2017, 114, 383-392.
17. Dou S, Shen AL, Ma ZL, Wu JH, Tao L, Wang SY. N, P and S-tridoped graphene as metal-free electrocatalyst for oxygen reduction reaction. *J. Electroanal. Chem.*, 2015, 753, 21-27.

UNIVERSITY of the
WESTERN CAPE

http://etd.uwc.ac.za/

18. Liao JY, Higgins D, Lui G, Chabot V, Xiao XC, Chen ZW. Multifunctional TiO_2-C/MnO_2 core-double-shell nanowire arrays as high-performance 3D electrodes for lithium ion batteries. *Nano Lett.*, 2013, 13(11), 5467-5473.
19. Yuan S, Huang XL, Ma DL, Wang HG, Meng FZ, Zhang XB. Engraving copper foil to give large-scale binder-free porous CuO arrays for a high-performance sodium-ion battery anode. *Adv. Mater.*, 2014, 26(14), 2273-2279.
20. Zhang YC, Qiao T, Hu XY. A Simple hydrothermal route to nanocrystalline CuS. *J. Cryst. Growth*, 2004, 268(1-2), 64-70.
21. Pi MY, Yang T, Wang SX, Chen SJ. One-pot synthesis of insitu carbon-decorated Cu_3P particles with enhanced electrocatalytic hydrogen evolution performance. *J. Mater. Res.*, 2018, 33(5), 546-555.
22. Basu M, Nazir R, Fageria P, Pande S. Construction of CuS/Au heterostructure through a simple photoreduction route for enhanced electrochemical hydrogen evolution and photocatalysis. *Sci. Rep.*, 2016, 6(1), 1-11.
23. Li J, Jiu TG, Tao GH, Wang GJ, Sun CM, Li PD, Fang JF, He L. Manipulating surface ligands of copper sulfide nanocrystals: Synthesis, characterization, and application to organic solar cells. *J. Colloid Interface Sci.*, 2014, 419, 142-147.
24. Wang Z, Du HT, Liu ZA, Wang H, Asiri AM, Sun XP. Interface engineering of a CeO_2-Cu_3P nanoarray for efficient alkaline hydrogen evolution. *Nanoscale*, 2018, 10(5), 2213-2217.
25. Wang R, Dong XY, Du J, Zhao JY, Zang SQ. MOF-derived bifunctional Cu_3P nanoparticles coated by a N,P-codoped carbon shell for hydrogen evolution and oxygen reduction. *Adv. Mater.*, 2018, 30(6), 1703711.
26. Popczun EJ, McKone JR, Read CG, Biacchi AJ, Wiltrout AM, Lewis NS, Schaak RE. Nanostructured nickel phosphide as an electrocatalyst for the hydrogen evolution reaction. *J. Am. Chem. Soc.*, 2013, 135(25), 9267-70.
27. Hou HW, Xie Y, Li Q. Large-scale synthesis of single-crystalline quasi-aligned submicrometer cuo ribbons. *Cryst. Growth Des.*, 2005, 5(1), 201-205.

UNIVERSITY of the
WESTERN CAPE

http://etd.uwc.ac.za/

28. Xia XH, Zhu CR, Luo JS, Zeng ZY, Guan C, Ng CF, Zhang H, Fan HJ. Synthesis of free-standing metal sulfide nanoarrays via anion exchange reaction and their electrochemical energy storage application. *Small*, 2014, 10(4), 766-773.
29. Guan Q, Li W. A novel synthetic approach to synthesizing bulk and supported metal phosphides. *J. Catal.*, 2010, 271(2), 413-415.
30. Yan Y, Xia B, Xu ZC, Wang X. Recent development of molybdenum sulfides as advanced electrocatalysts for hydrogen evolution reaction. *ACS Catal.*, 2014, 4(6), 1693-1705.
31. Wang H, Zhou TT, Li PL, Cao Z, Xi W, Zhao YF, Ding Y. Self-supported hierarchical nanostructured NiFe-LDH and Cu_3P weaving mesh electrodes for efficient water splitting. *ACS Sustainable Chem. Eng.*, 2017, 6(1), 380-388.
32. Manikandan A, Lee L, Wang YC, Chen CW, Chen YZ, Medina H, Tseng JY, Wang ZM, Chueh YL. Graphene-coated copper nanowire networks as a highly stable transparent electrode in harsh environments toward efficient electrocatalytic hydrogen evolution reactions. *J. Mater. Chem. A*, 2017, 5(26), 13320-13328.
33. Hou CC, Chen QQ, Wang CJ, Liang F, Lin Z, Fu WF, Chen Y. Self-supported cedarlike semimetallic Cu_3P nanoarrays as a 3D high-performance janus electrode for both oxygen and hydrogen evolution under basic conditions. *ACS Appl. Mater. Interfaces*, 2016, 8(35), 23037-48.
34. Pi MY, Yang T, Wang SX, Chen SJ. One-pot synthesis of in situ carbon-decorated Cu_3P particles with enhanced electrocatalytic hydrogen evolution performance. *J. Mater. Res.*, 2017, 33(05), 546-555.
35. Ren H, Xu WC, Zhu SL, Cui ZD, Yang XJ, Inoue A. Synthesis and properties of nanoporous A_2S/CuS catalyst for hydrogen evolution reaction. *Electrochim. Acta*, 2016, 190, 221-228.
36. Fan MH, Gao RQ, Zou YC, Wang DJ, Bai N, Li GD, Zou XX. An efficient nanostructured copper(I) sulfide-based hydrogen evolution electrocatalyst at neutral pH. *Electrochim. Acta*, 2016, 215, 366-373.

UNIVERSITY of the
WESTERN CAPE

http://etd.uwc.ac.za/

37. Du HT, Zhang XP, Tan QQ, Kong RM, Qu FL. A Cu_3P-CoP hybrid nanowire array: A superior electrocatalyst for acidic hydrogen evolution reactions. *Chem. Commun.*, 2017, 53(88), 12012-12015.
38. Basu M, Nazir R, Fageria P, Pande S. Construction of CuS/Au heterostructure through a simple photoreduction route for enhanced electrochemical hydrogen evolution and photocatalysis. *Sci. Rep.*, 2016, 6, 34738.
39. Kuang M, Wang Qh, Han P, Zheng GF. Cu, Co-embedded N-enriched mesoporous carbon for efficient oxygen reduction and hydrogen evolution reactions. *Adv. Energy Mater.*, 2017, 7(17), 1700193.
40. Zhu L, Lin H, Li Y, Liao F, Lifshitz Y, Sheng M, Lee ST, Shao M. A rhodium/silicon co-electrocatalyst design concept to surpass platinum hydrogen evolution activity at high overpotentials. *Na.t Commun.*, 2016, 7, 12272.
41. Hou JG, Sun YG, Wu YZ, Cao SY, Sun LC. Promoting active sites in core-shell nanowire array as mott-schottky electrocatalysts for efficient and stable overall water splitting. *Adv. Funct. Mater.*, 2018, 28(4), 1704447.
42. Singh RK, Ramesh R, Devivaraprasad R, Chakraborty A, Neergat M. Hydrogen interaction (electrosorption and evolution) characteristics of Pd and Pd_3Co alloy nanoparticles: An in-situ investigation with electrochemical impedance spectroscopy. *Electrochim. Acta*, 2016, 194, 199-210.
43. Cai P, Huang J, Chen J, Wen Z. Oxygen-containing amorphous cobalt sulfide porous nanocubes as high-activity electrocatalysts for the oxygen evolution reaction in an alkaline/neutral medium. *Angew. Chem. Int. Ed.*, 2017, 56(17), 4858-4861.
44. Zhang G, Wang G, Liu Y, Liu H, Qu J, Li J. Highly active and stable catalysts of phytic acid-derivative transition metal phosphides for full water splitting. *J. Am. Chem. Soc.*, 2016, 138(44), 14686-14693.
45. Chakraborty A, Devivaraprasad R, Bera B, Neergat M. Electrochemical estimation of the active site density on metal-free nitrogen-doped carbon using catechol as an adsorbate. *Phys. Chem. Chem. Phys.*, 2017, 19(37), 25414-25422.

UNIVERSITY of the
WESTERN CAPE

http://etd.uwc.ac.za/

46. Tian JQ, Liu Q, Cheng NY, Asiri AM, Sun XP. Self-supported Cu_3P nanowire arrays as an integrated high-performance three-dimensional cathode for generating hydrogen from water. *Angew. Chem., Int. Ed.*, 2014, 53(36), 9577-9581.
47. Joo SH, Choi SJ, Oh I, Kwak J, Liu Z, Terasaki O, Ryoo R. Ordered nanoporous arrays of carbon supporting high dispersions of platinum nanoparticles. *Nature*, 2001, 412, 169.
48. Oyama ST, Gott T, Zhao H, Lee YK. Transition metal phosphide hydroprocessing catalysts: A review. *Catal. Today*, 2009, 143(1-2), 94-107.
49. Zhou WJ, Wu XJ, Cao XH, Huang X, Tan CL, Tian J, Liu H, Wang JY, Zhang H. Ni_3S_2 nanorods/Ni foam composite electrode with low overpotential for electrocatalytic oxygen evolution. *Energy Environ. Sci.*, 2013, 6(10), 2921.

UNIVERSITY of the
WESTERN CAPE

http://etd.uwc.ac.za/

CHAPTER 5 Bimetallic Ni-Co Phosphide Nanosheets Self-Supported on Nickel Foam as High-Performance Electrocatalyst for Hydrogen Evolution Reaction

This chapter focuses on studying the bimetallic Ni–Co phosphide nanosheets self-supported on nickel foam which were used as efficient electrocatalysts for the hydrogen evolution reaction, and the corresponding mechanism for hydrogen evolution is presented. The work in this chapter comes from an article from the author entitled "Bimetallic Ni–Co phosphide nanosheets self-supported on nickel foam as high-performance electrocatalyst for hydrogen evolution reaction, *Electrochimica Acta*, 2019**,** 317, 191-198".

5.1 Introduction

UNIVERSITY of the
WESTERN CAPE

The issues concerning the energy crisis and environmental pollution caused by fossil fuels are becoming increasingly serious and thus it is important to search for clean and renewable energy sources as alternatives to fossil fuels. Hydrogen (H_2) is recognized as one of the more environmentally friendly and earth abundant source of energy and is not associated greenhouse gas emissions.[1] To realize commercial utilization of H_2, a renewable pathway to produce H_2 in a cost-effective route is of great importance, since this would have a profound influence on the energy consumption in the future. Electrochemical water splitting driven by an external renewable source of power such as intermittent solar and wind energy, is a sustainable and ideal way for producing H_2. The process of electrochemical water splitting ($2H_2O \rightarrow O_2 + 2H_2$) consists of the

http://etd.uwc.ac.za/

hydrogen evolution reaction (HER) at the cathode and the oxygen evolution reaction (OER) at the anode for hydrogen (H_2) and oxygen (O_2) production, respectively.[2] To achieve a high water splitting efficiency, an optimal electrocatalyst to minimize the overpotential to drive HER and OER is required. The platinum group metals (PGMs) (e.g., Pt, Rh, Ir, Ru and Pd) are the most active benchmark electrocatalysts for HER. However, the relatively high cost and scarcity, seriously hinder their further large-scale application.[3] Therefore, significant efforts have been devoted over the last decade to synthesize highly efficient and stable HER electrocatalysts with inexpensive and earth-abundant elements. Among these are the transition metal (e.g. Cu, Fe, Ni, Co, W and Mo) compounds, including carbides,[4,5] borides,[6] selenides,[7,8] nitrides,[9,10] phosphides,[11] oxides[12,13] and sulfides.[14,15] These have been extensively studied and possess tremendous potential as promising HER electrocatalysts. Specifically, transition metal phosphides show high HER catalytic activity, such as cobalt phosphides (CoP, Co_2P),[16] nickel phosphides (NiP, Ni_2P),[17] iron phosphides (FeP),[18] molybdenum phosphides (MoP),[19] and copper phosphides (Cu_3P).[20] Feng *et al*.[21] fabricated Co_2P nanocrystals as efficient HER electrocatalysts, which exhibited an overpotential of 150 mV at –10 mA cm^{-2}, a Tafel slope of 55 mV dec^{-1} in 0.5 M H_2SO_4 media. Liu *et al*. [22] synthesized CP@Ni-P as HER electrocatalyst with an overpotential of 117 mV at –10 mA cm^{-2} and a Tafel slope of 85.4 mV dec^{-1} in 1.0 M KOH alkaline solution.

As is well known, most of the electrocatalysts in the initial stage are in powder form. In order to fabricate the HER electrode, they need to be coated onto a conductive substrate

UNIVERSITY of the WESTERN CAPE

http://etd.uwc.ac.za/

with Nafion, PTFE or other polymeric binders. These binders are able to bury parts of active sites and thus decrease the catalytic activity. Meanwhile, the H_2 bubbles generated during the hydrogen evolution process on the surface of electrocatalysts are able to easily detach part of the electrocatalyst on the substrate surface, thus lowering the catalytic activity.[23-25] Thus, in order to improve the stability and activity as well as reduce the use of binders, current collectors such as nickel foam, carbon paper and titanium plate are used. The 3D nickel foam (NF) with a large surface area, high conductivity and stability is being considered as a promising candidate to act as supporting substrate. Zhang *et al*. [26] fabricated Ni-Co-P/NF as HER electrocatalyst *via* electrodeposition. They found that Ni-Co-P/NF required a small overpotential of 107 mV to achieve a current density of –10 mA cm^{-2} in 1.0 M KOH media, and it exhibited a large Tafel slope (62 mV dec^{-1}). They ascribe their results to the fact that the tested material presented amorphous film morphology with low specific surface area, thus exposing a reduced amount of active sites. Wang *et al*. [27] also synthesized Ni-Co-P/NF *via* hydrothermal and calcination methods that led to a novel nanobrushed structure, containing only the NiCoP (JCPDS no. 71-2336) phase which could explain the required large overpotential of 156 mV at –10 mA cm^{-2} toward HER in 1.0 M KOH alkaline media. Shen *et al*. [28] fabricated Ni-Co-P/NF by electrodeposition, having a dense-packed spheres morphology and it required overpotentials of about 110 mV to achieve a current density of –10 mA cm^{-2} in 1.0 M KOH and exhibiting a large Tafel slope (62 mV dec^{-1}). All data were obtained at a low current density (less than –40 mA cm^{-2}). Lu *et al*. [29] obtained Ni–Co–P/C_{60} powder by the solvothermal and phosphatizing method which had an overpotential of 97 mV at –10

UNIVERSITY of the WESTERN CAPE

http://etd.uwc.ac.za/

mA cm^{-2} and fast charge-transfer kinetics (about 50 Z′/ohm). While, the Ni–Co–P/C_{60} powder has an agglomeration and with a big size (＞100 nm). This has the advantage to reduce exposure of active sites and decrease the HER activity which in our view might be the reason it only displayed activity at low current density (less than –50 mA cm^{-2}). In practical applications, HER or OER performance, it is more important that these operate at large current density values.

Hence, considering the excellent catalytic potential of bimetallic Ni–Co phosphides, highly HER performing bimetallic Ni–Co phosphides self-supported on NF with a novel morphology were synthesized. Firstly, the bimetallic Ni-Co/NF electrode was fabricated using the electrodeposition method at room-temperature. Then, the bimetallic phosphide Ni-Co-P/NF was synthetized by low-temperature phosphorization, which lead to a unique structure of nanosheets randomly dispersed on a villiform 3D integrated framework. Impressively, it exhibited a low overpotential of 85 mV (to deliver a current density of –10 mA cm^{-2} in 1.0 M KOH medium) and with excellent durability. Moreover, this assembly also exhibits low overpotential values of 210 and 350 mV to deliver large current densities of −500 and −1,500 mA cm^{-2}, and with a low Tafel slop of 46 mV dec^{-1}. The synergistic effect between the active phases and the unique morphology of Ni-Co-P/NF electrode could overwhelmingly strengthen the catalytic activity toward HER in alkaline media, as compared with other non-noble metal electrocatalysts.

UNIVERSITY of the
WESTERN CAPE

http://etd.uwc.ac.za/

5.2 Experimental

5.2.1 Materials

Potassium hydroxide (KOH), hydrochloric acid (HCl), cobalt acetate tetrahydrate ($C_4H_6CoO_4 \cdot 4H_2O$), nickel chloride hexahydrate ($NiCl_2 \cdot 6H_2O$), ammonium chloride (NH_4Cl), sodium hypophosphite ($NaHPO_2 \cdot H_2O$), and anhydrous ethanol (C_2H_5OH) were obtained from Macklin reagents Co., Ltd. All chemicals were used directly without further purification, and deionized water was lab-made. Ni foams (1.0 cm × 1.0 cm) were cleaned by sonication successively in 20% HCl, C_2H_5OH, and deionized water (15 min each) to remove the surface oxides.

5.2.2 Preparation of Ni-Co/NF, Co/NF and Ni/NF

1.5 mM $C_4H_6CoO_4 \cdot 4H_2O$, 1.5 mM $NiCl_2 \cdot 6H_2O$ and 0.10 g NH_4Cl were dissolved in 250 mL of deionized water under vigorous stirring for 30 min and the as obtained solution was transferred to a 500 mL electrolytic cell. Experiments were carried out under a constant current density of –10 mA cm^{-2} for 30 min, using a standard electrochemical workstation equipped with a three-electrode system. A piece of Ni foam (1.0 cm × 1.0 cm) was used as the working electrode, and graphite rod and reversible hydrogen electrode (RHE) were used as the counter and reference electrode, respectively and were immersed in the electrolyte kept at 25 °C in a water bath. Finally, the as-obtained Ni-Co/NF electrocatalyst was washed with deionized water and C_2H_5OH (ethanol) several times, and then dried at 60 °C in a vacuum drying oven

UNIVERSITY of the
WESTERN CAPE

http://etd.uwc.ac.za/

for 6 h. For comparison, the Co/NF and Ni/NF precursors were also prepared by the same procedure without $NiCl_2 \cdot 6H_2O$ and $C_4H_6CoO_4 \cdot 4H_2O$.

5.2.3 Preparation of Ni-Co-P/NF, Co-P/NF and Ni-P/NF

To obtain the Ni-Co-P/NF bimetallic phosphides electrode, the Ni-Co/NF precursor and $NaH_2PO_2 \cdot H_2O$ were placed at two separate positions in a porcelain boat, which was put at the center of a tubular furnace. The weight ratio of Ni-Co/NF and $NaH_2PO_2 \cdot H_2O$ was 1:10, and the porcelain boat located at the upstream side of the furnace. Subsequently, the furnace was purged with nitrogen (N_2 99.999%) for 15 min, then heated to 300 ^oC at a ramping rate of 5 ^oC min^{-1} and maintained at 300 ^oC for 2 h. After natural cooling to room temperature, the obtained sample was denoted as Ni-Co-P/NF. The Co-P/NF and Ni-P/NF were prepared by following the same procedure.

5.2.4 Physico-Chemical Characterization

UNIVERSITY of the
WESTERN CAPE

The crystalline structure of the samples was characterized by X-ray powder diffraction (XRD, Rigaku Corp., Japan) equipped with Cu-Kα radiation (λ=0.15406 nm), operating at a voltage of 40 kV and a current of 30 mA. The microstructure and element composition distribution were characterized by field emission scanning electron microscopy (SEM) and elemental mapping analysis (EDS) (FE-SEM, SU8220, Hitachi Corp., Japan). The electronic structures, surface chemical compositions and states of the samples were studied by X-ray photoelectron spectroscopy (ESCALab 250Xi, ThermoFisher Scientific, USA) with Al Kα radiation. Scanning transmission electron microscopy (STEM), energy dispersive X-ray

http://etd.uwc.ac.za/

spectroscopy (EDX) investigation, high-resolution transmission electron microscopy (HRTEM) and selected area electron diffraction (SAED) were also performed (Titan ETEM G2 80–300-FEI Co., USA) at an accelerating voltage of 200 kV, providing information of the particle size distribution, structure and composition of the electrocatalysts. Contact angles with 1.0 M KOH in deionized water were measured with the sessile drop method using tensiometer (Attension Theta Lite TL-100, Biolin Scientific, Sweden).

The electrochemical tests were performed in a typical computer controlled electrochemical workstation (Zahner IM6e, Germany). The chronopotentiometry (CP) curves were recorded by an electrochemical workstation (PINE, USA) under a constant current of –10 mA cm^{-2} in 1.0 M KOH. The Ni-Co-P grown on NF can be directly used as a working electrode, without employing extra substrates or binders. The geometric area of the working electrode was 1.0 cm^2 (1.0 cm × 1.0 cm). A Pt/C electrocatalyst (mass loading of Pt was 0.05 mg cm^{-2}) was coated on a glassy carbon disk by the aid of Nafion, which was used as the benchmark of HER. It should be noted that, commercial Pt/C is facile to detach from the Ni foam's surface. For this reason, the glassy carbon disk electrode is employed to test the corresponding HER catalytic performance. During the LSV tests, the scan rate was kept at 10 mV s^{-1}. In addition, electrochemical impedance spectroscopy (EIS) measurements were taken with amplitude of 5 mV in a frequency range from 100 kHz to 100 mHz. According to the measurements of high-frequency AC impedance, all potentials were *IR* compensated; where *I* and *R* denote the current and uncompensated ohmic electrolyte resistance. The HER kinetic behavior, of the as-

UNIVERSITY of the WESTERN CAPE

http://etd.uwc.ac.za/

prepared electrocatalysts, was taken using the plots resulted from the Tafel equation ($\eta = b\log(j) + a$; where η denotes the overpotential, b the Tafel slope, and j the current density).[1] The electrochemical active surface areas (ECSAs) were evaluated through the electrochemical double-layer capacitance (C_{dl}) in the potential range from 0.15 to 0.25 V (*vs.* RHE).

5.3 Results and Discussions

The detailed procedure of Ni-Co-P/NF synthesis is schematically represented in Figure 5.1.

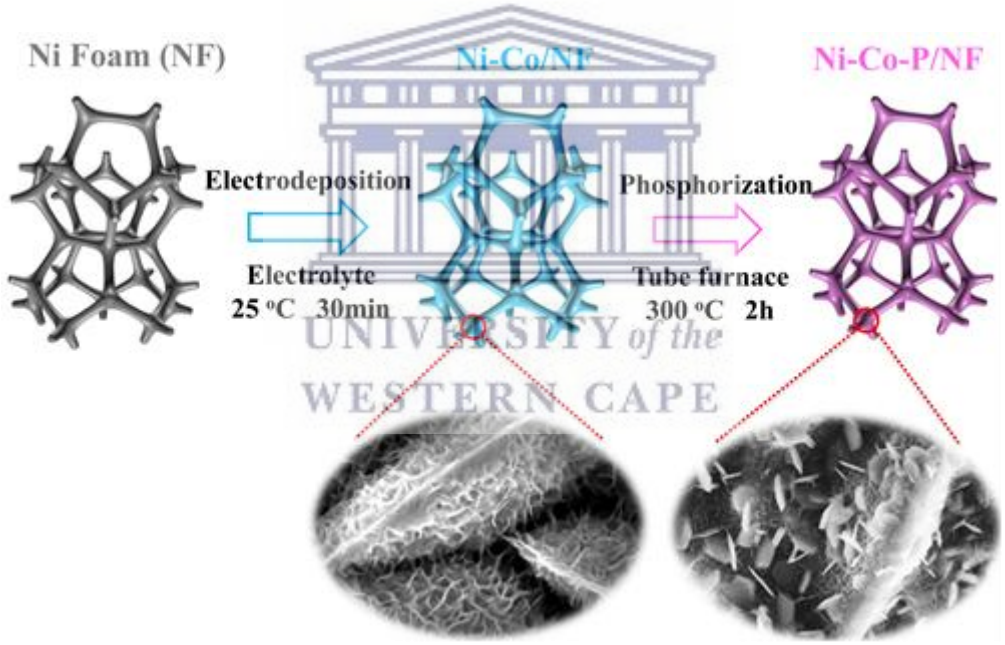

Figure 5.1 Schematic illustration for the synthesis of Ni-Co-P/NF.

In a typical synthesis, the Ni-Co-P/NF electrocatalyst was prepared by electrodeposition followed by low-temperature phosphorylation in a quartz tube furnace, and heated at 300 °C for 2 h with a ramp rate of 10 ^{o}C min^{-1} in a N_2 atmosphere.

http://etd.uwc.ac.za/

The crystal structures of the as-synthesized samples were confirmed by XRD, as shown in Figures 5.2–5.5. Obviously, the peaks at 2θ of 44.53° (111), 51.88° (200) and 76.48° (220) can be assigned to the metallic Ni foam (PDF No.# 70-0989) in all the as-obtained materials. The XRD data (Figure 5.2) shows that Ni-Co-P/NF has three crystal phases, including NiCoP, NiP and Co_2P, respectively. The characteristic peaks of hexagonal-close packed (*hcp*) NiCoP (PDF No.# 71-2336) [30] appeared at 2θ of 40.99°, 47.58°, 54.44°, 54.74°, 55.34°, which indexed to the diffractions of (111), (210), (300), (002) and (211) planes, respectively. Besides, the diffraction peaks at 41.98°, 48.06°, 49.75°, 53.13°, 53.45° indexed to the planes (121), (122), (221), (004) and (213) of NiP (PDF No.# 74-1382) phase. The three obvious peaks appeared at 2θ of 40.96°, 42.06° and 48.76° are deemed as the (210), (202) and (013) planes of Co_2P (PDF No.# 89-3030).

UNIVERSITY of the
WESTERN CAPE

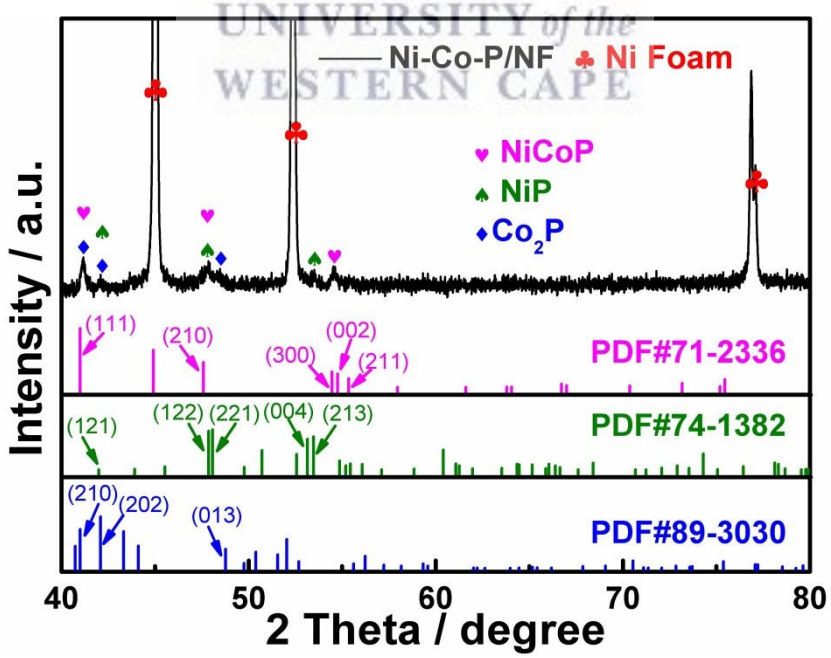

Figure 5.2 XRD pattern of Ni-Co-P/NF electrocatalyst.

http://etd.uwc.ac.za/

The XRD results of Ni-Co/NF and Co/NF precursor (Figures 5.3 & 5.4) indicate that the Ni-Co/NF form a Ni–Co alloy phase, due to the right deviation of the (100) crystal plane in Ni-Co/NF (Figure 5.3b).[31] The XRD result (Figure 5.3a) shows the Ni–Co alloy electrode is constructed with Ni (PDF No.# 70-0989) and Co (PDF No.# 05-0727).

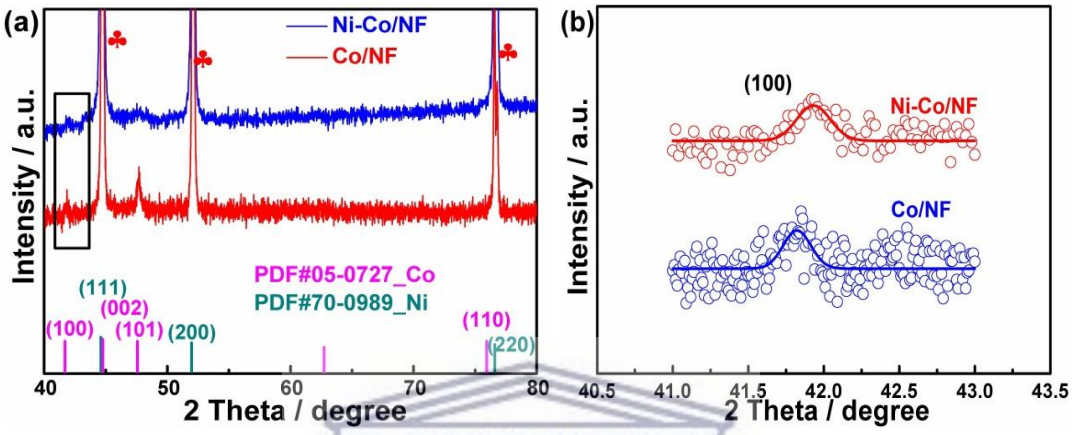

Figure 5.3 (a) XRD pattern of Ni-Co/NF, Co/NF; (b) curve fittings of (100) diffraction peaks in (a) that marked as black frame.

The selected area electron diffraction (SAED) of Ni-Co/NF shown in Figure 5.4a, illustrates that the Ni-Co/NF has a polycrystalline nature. Due to the strong peaks of NF, we replaced the base with a Ti sheet since this assists with the Ni–Co coating being easily peeled off form this base for the XRD test. The (111) and (220) peaks are fitted to a Gaussian line shape (Figure 5.4b), and the position of the peaks can be precisely obtained. The both peaks are between PDF No.# 05-0727 (Co) and PDF No.# 70-0989 (Ni), indicating an alloy structure.[32] The atomic percentage of Ni and Co elements at the surface of Ni-Co/NF are 10.31% and 18.67% respectively, verified by XPS, while the atomic ratio of Ni/Co is about 1:2. Therefore, the Co metal precursor is a significant player for the formation of Ni-Co-P/NF. Meanwhile, Zhang *et al*. [33] showed that the

UNIVERSITY of the
WESTERN CAPE

http://etd.uwc.ac.za/

free Co atom cannot enter the NiCoP crystallite, facile to form a separate Co_2P phase, which agrees with the above XRD results of Ni-Co-P/NF which form mixture phases. Kim *et al.* [34] proved that with an increase of Co , the NiCoP exhibited a better performance than $Ni_{0.8}Co_{1.2}P$ which clearly demonstrates that the synergy between the three phases (NiCoP, NiP and Co_2P) could be favorable for improving the HER performance of Ni-Co-P/NF. By comparing Figures 5.2–5.4, one can conclude that after phosphorization, the Ni–Co alloy precursor is completely transformed to the NiCoP, NiP and Co_2P phases.

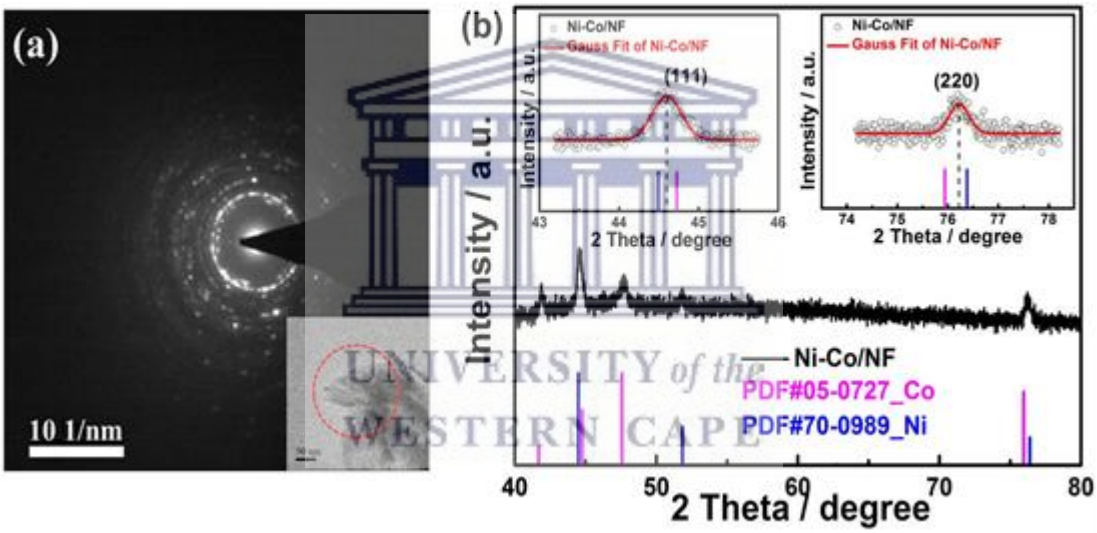

Figure 5.4 (a) SAED pattern and (b) XRD curves for Ni-Co/NF; the XRD with a scan rate of 5° min^{-1}, and the insert picture is shows curve fittings for (111) and (220) diffraction peaks.

For the Co/NF precursors, the Ni foam has also undergone phosphorization as illustrated in Figure 5.5a which shows the Co-P/NF composed of Co_2P (PDF No.# 89-3030) and Ni_2P (PDF No.# 65-9706). For the pure Ni-P/NF composite (Figure 5.5b), six diffraction peaks at 2θ values of 40.84°, 47.44°, 54.49°, 55.14°, 72.89° and 75.09° can be

http://etd.uwc.ac.za/

indexed to diffractions of (111), (210), (002), (211), (311) and (212) planes of standard Ni_2P (PDF No.# 65-9706), indicating the existence of the Ni_2P phase.

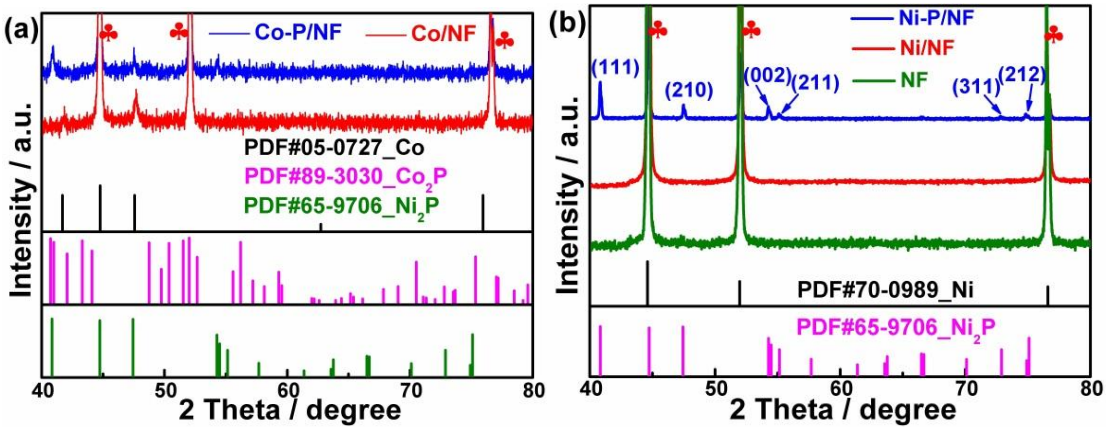

Figure 5.5 (a) XRD pattern of Co-P/NF, Co/NF; (b) XRD pattern of Ni-P/NF, Ni/NF and NF.

The XPS measurements were made to confirm the surface compositions and states of Ni-Co-P/NF and Ni-Co/NF. Figure 5.6a shows the XPS survey spectra confirming the Ni-Co/NF phosphorylation into Ni-Co-P/NF, and the existence of Ni, Co, O and P elements in Ni-Co-P/NF. Figures 5.6(b−f) display the fine scans of Ni2p, Co2p, P2p and O1s, respectively. All XPS data were corrected by C1s peak at 284.8 eV. Similarly, the $Co2p_{3/2}$ and $Co2p_{1/2}$ peaks are centered at 780.83 and 796.59 eV, accompanied by two shake-up satellite peaks (785.70 and 803.35 eV) (displayed in Figure 5.6b),[35] Peaks at 780.83 eV could be ascribed to Co−PO_x with its shakeup satellite peak at 785.70 eV.[36] For Ni2p of Ni-Co-P/NF (Figure 5.6c), the binding energies (BEs) at 855.86 and 873.55 eV belong to $Ni2p_{3/2}$ and $Ni2p_{1/2}$.[37] The fitted $Ni^{2+}2p_{3/2}$ main peak and its satellites are at 855.85 eV and 861.55 eV, while the main $Ni^{2+}2p_{1/2}$ peak and its satellites are at 873.5 and 879.85 eV. The peak at 855.86 eV could be attributed to Ni−PO_x with its shakeup satellite (identified as "Sat.") peak at 861.58 eV.[38] As displayed in Figures 5.6(b & c),

http://etd.uwc.ac.za/

the main peaks of Co2p and Ni2p in Ni-Co-P/NF shift toward lower binding energies, thus the binding energy of $Co2p_{3/2}$, $Co2p_{1/2}$, $Ni2p_{3/2}$ and $Ni2p_{1/2}$ in the Co2p and Ni2p spectra of Ni-Co-P/NF is lower than the ones of Ni-Co/NF. This means that the interaction between nickel-cobalt phosphide is lower than in nickel-cobalt alloy.[27]

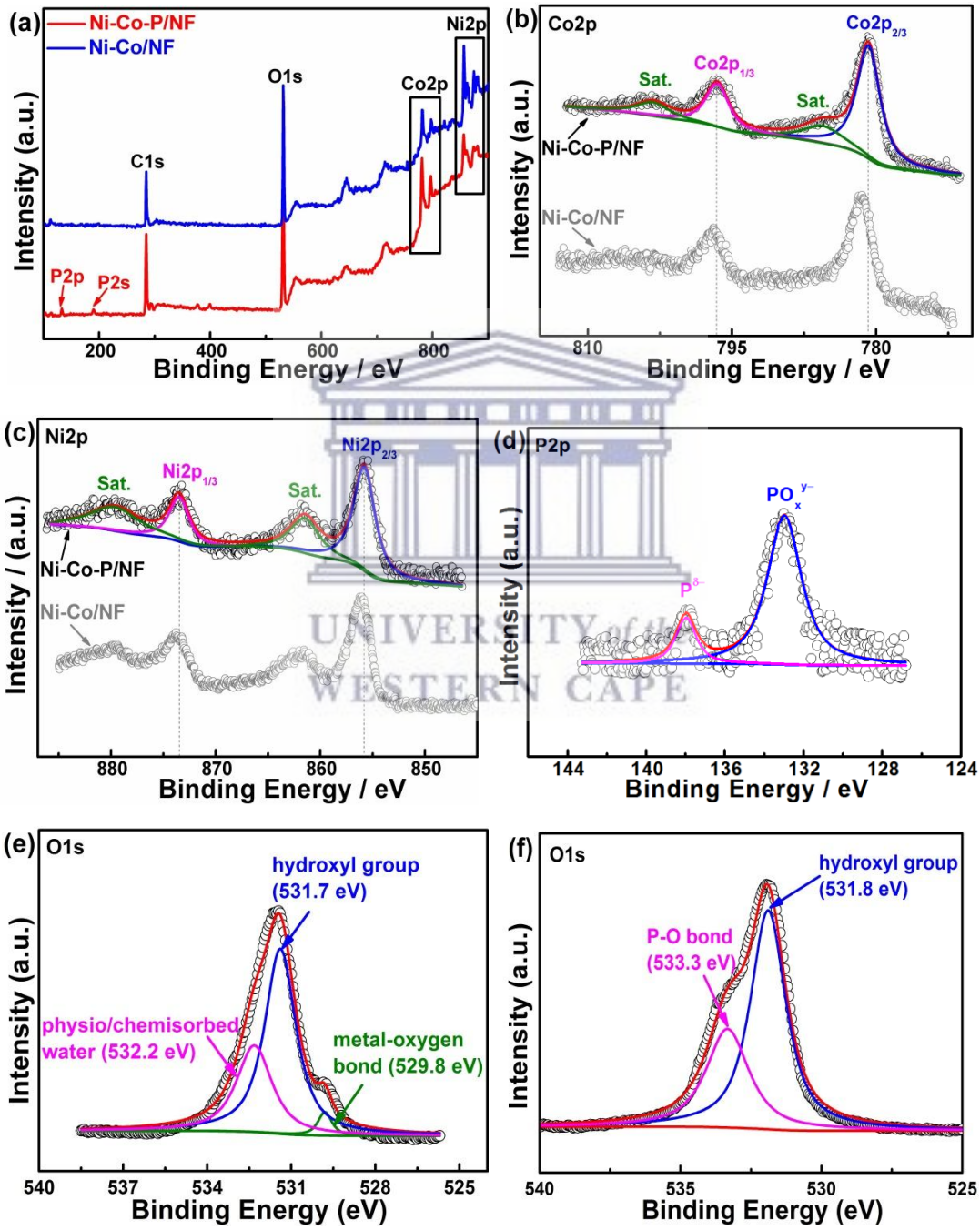

Figure 5.6 (a) XPS summary of Ni-Co-P/NF and Ni-Co/NF, (b) Co2p, (c) Ni2p, (d) P2p and O1s of (e) Ni-Co/NF and (f) Ni-Co-P/NF.

http://etd.uwc.ac.za/

In the high-resolution XPS spectrum of P2p (Figure 5.6d), peaks at 129.00 and 130.18 eV represent $P2p_{3/2}$ and $P2p_{1/2}$ in Ni-Co-P/NF.[39] The binding energy at 129.00 eV corresponds to the formation of metal phosphides, slightly lower than that of P (130.0 eV), which suggests that the P atom is partially negatively charged ($P^{\delta-}$).[40] Furthermore, the other peak at 133.38 eV is attributed to the phosphate species (PO_4^{3-}), probably due to the partial oxidation after long-term exposure to the air.[38]

From the high resolution O1s XPS spectra, Figure 5.6(e) the O1s of Ni-Co/NF can be divided into three peaks. The peak at ~529.8 eV is ascribed to the metal-oxygen bond, the one at ~532.2 eV is due to some oxygen physico/chemisorbed water at the surface and the peak at ~531.8 eV represents the hydroxyl group. However, the O1s XPS spectrum of Ni-Co-P/NF (Figure 5.6f) is divided into two peaks. The peak at ~531.8 eV is ascribed to the hydroxyl group, formed by the thermal decomposition of $NaH_2PO_2 \bullet H_2O$ into H_2O vapor during calcination. The peak at ~533.3 eV could be attributed to the P-O bond, formed by the decomposition of $NaH_2PO_2 \bullet H_2O$ into phosphine (PH_3) vapor during calcination.[41] From the O1s XPS spectrum, it can be concluded that Ni-Co-P/NF is formed by the synergy interaction between NiCo hydroxide and NiCo phosphate. From EIS and LSV results, Ni-Co-P/NF has better activity and conductivity than Ni-Co/NF, which may be attributed to the role of P–O bond of the oxygen inclusion. All the XRD and XPS characterizations demonstrate

UNIVERSITY of the
WESTERN CAPE

http://etd.uwc.ac.za/

formation of bimetallic phosphides and show the successful synthesis of Ni-Co-P/NF electrodes.

In order to further investigate the surface morphology and the hierarchical structure of the as-synthesized samples, SEM images with different magnifications were performed (Figures 5.7–5.12). In Figures 5.7(a–c), the Ni-Co/NF with the villiform 3D integrated framework structure can be clearly noted. After phosphorization, the nanosheets are formed and homogeneously distributed in the framework (Figures 5.8a–5.8c).

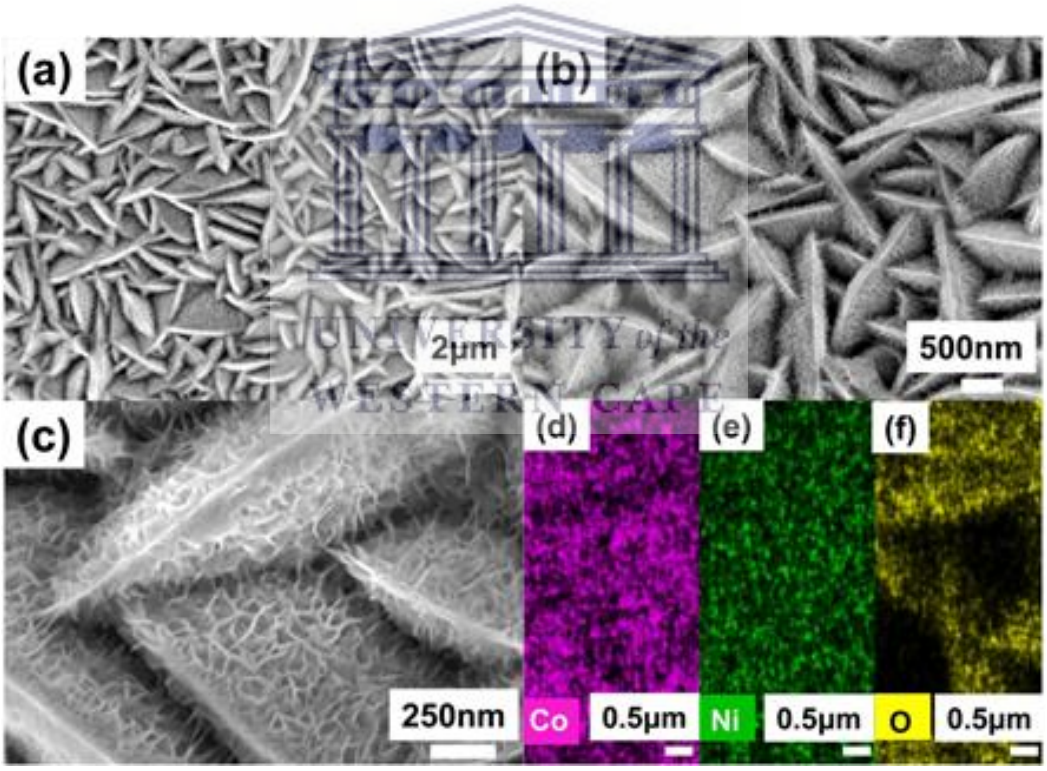

Figure 5.7 SEM (a–c) and EDS (d–f) images of Ni-Co/NF precursor.

http://etd.uwc.ac.za/

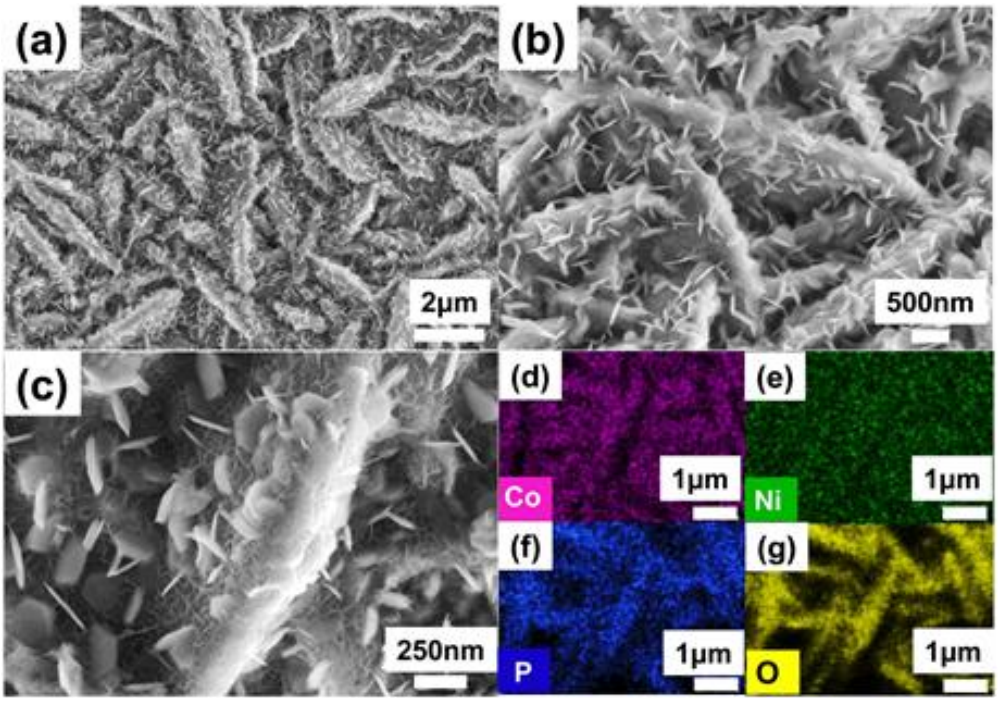

Figure 5.8 SEM (a–c) and EDS (d–g) images of Ni-Co-P/NF.

The above SEM results indicate that the Ni-Co-P/NF electrode is comprised of nanosheet structures, uniformly growing on the villiform 3D integrated framework, which could favor the promotion of catalytic activity. The elemental mapping analysis (EDS) spectra (Figures 5.8d–5.8g) indicate the homogeneous distribution of Ni, Co, O and P in Ni-Co-P/NF. The uniform dispersion of Co, Ni and O elements are also seen in Figures 5.7(d–f).

UNIVERSITY of the
WESTERN CAPE

http://etd.uwc.ac.za/

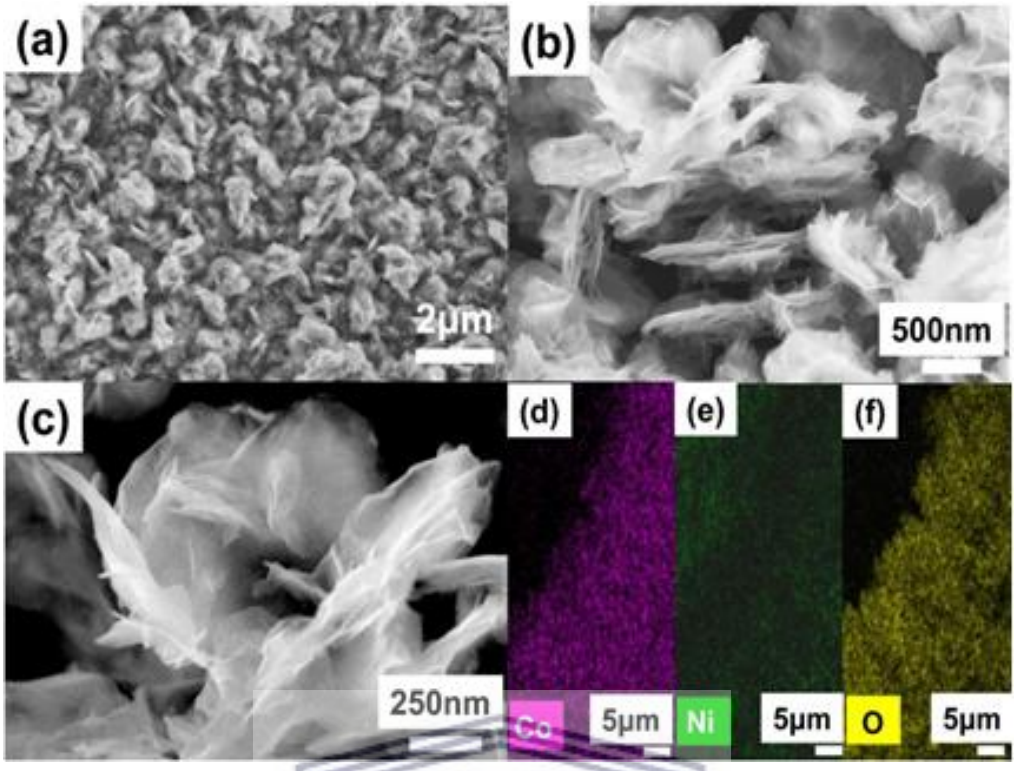

Figure 5.9 SEM (a–c) and EDS (d–f) images of Co/NF electrocatalyst.

UNIVERSITY of the
WESTERN CAPE

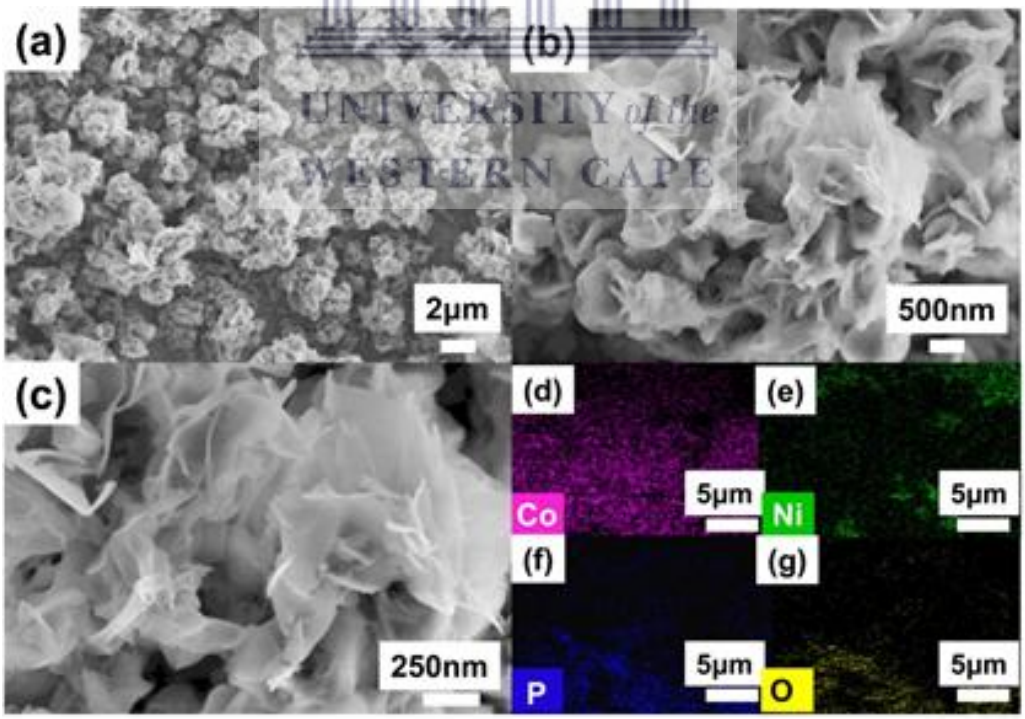

Figure 5.10 SEM (a–c) and EDS (d–g) images of Co-P/NF electrocatalyst.

http://etd.uwc.ac.za/

Furthermore, the surface morphology and hierarchical structure of Co-P/NF, Co/NF, Ni-P/NF and Ni/NF were also characterized by SEM (Figures 5.9–5.12). As displayed in Figures 5.9(a–c) & 5.10(a–c), it can be seen that the Co/NF with amorphous flower-like nanosheets, and after phosphatization is transformed into Co-P/NF, having a fluffy flower-like nanosheet structure. Figures 5.11(a–c) & 5.12(a–c) show that the Ni/NF is comprised of large nanospheres structures assembled from numerous small villous nanoparticles.

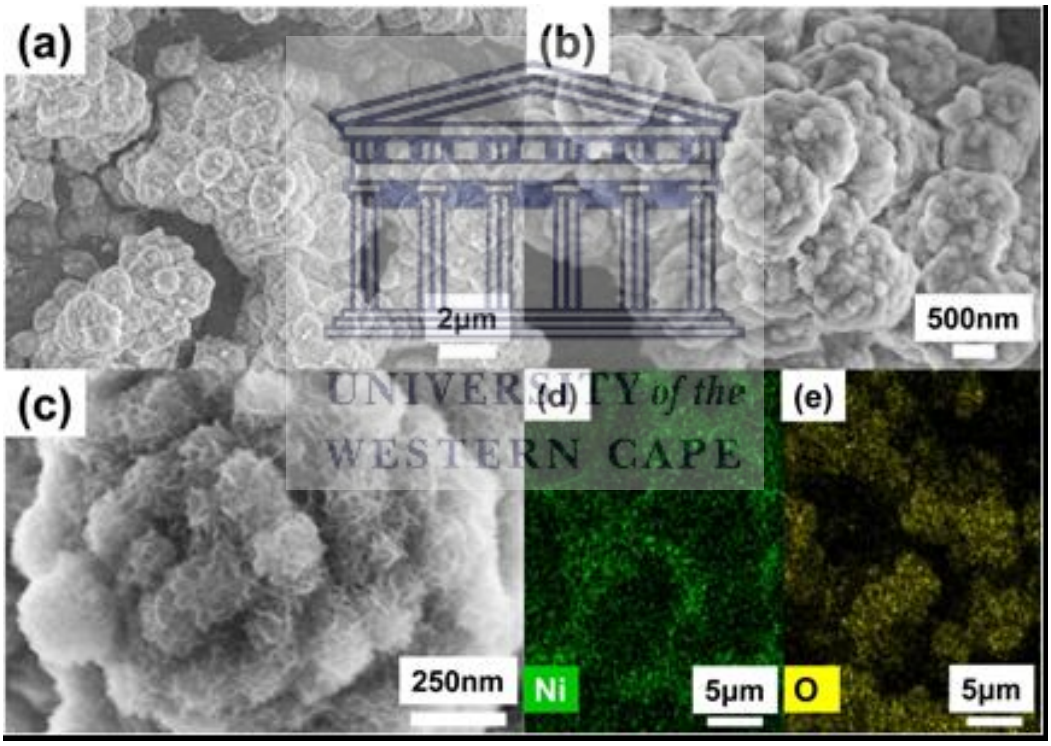

Figure 5.11 SEM (a–c) and EDS (d–e) images of Ni/NF electrocatalyst.

http://etd.uwc.ac.za/

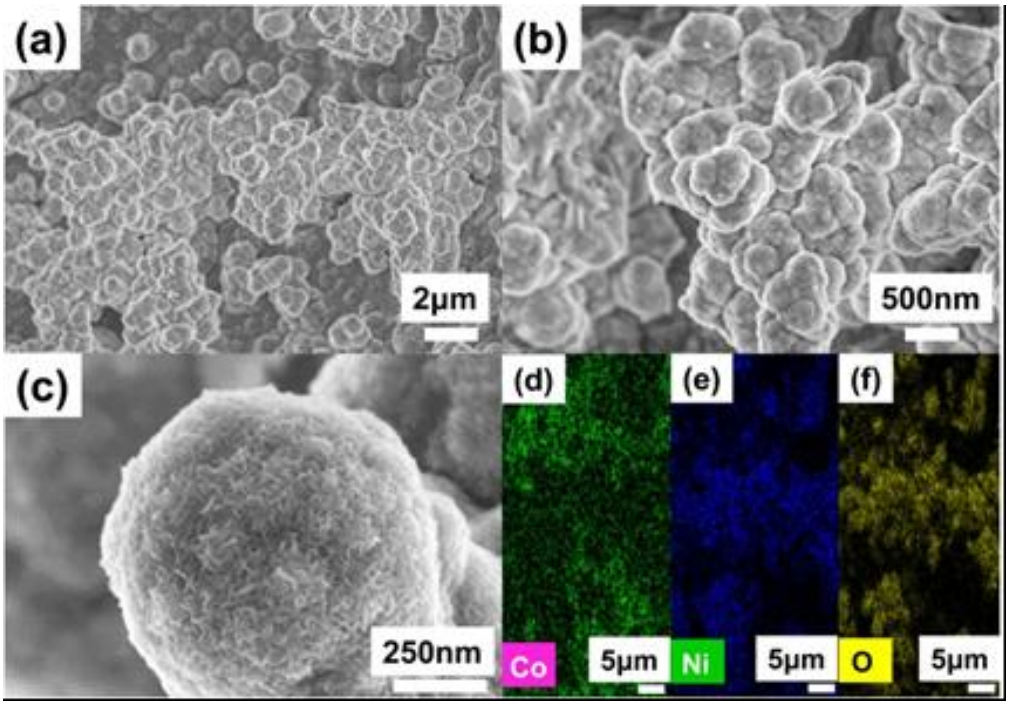

Figure 5.12 SEM (a–c) and EDS (d–f) images of Ni-P/NF electrocatalyst.

For Ni-P/NF, after phosphatizing, forms a wormlike nanosphere morphology which is different from that of Ni/NF. From the above SEM results, reasons for the formation of this particular Ni-Co-P/NF morphology may be due to i) that the villiform 3D integrated framework structure is formed by the interaction of Ni and Co, and ii) the formation of newborn nanosheets after phosphatizing due to Co_2P. The SEM-EDS results of Co/NF, Co-P/NF, Ni/NF and Ni-P/NF (Figures 5.9(d–f) & 5.10(d–g) & 5.11(d–e) & 5.12(d–f)) further confirm the co-existence of (Ni, Co, O), (Ni, Co, P, O), (Ni, O) and (Ni, P, O) elements, respectively, with uniform distribution in the prepared samples.

The morphology and structure of Ni-Co-P/NF were further characterized by TEM (Figure 5.13). The SAED (Figure 5.13b) illustrates the polycrystalline nature of Ni-Co-P/NF. As shown in the high resolution TEM (HRTEM), the lattice fringe of

UNIVERSITY of the
WESTERN CAPE
http://etd.uwc.ac.za/

~0.214 nm corresponds to the (202) facet of the Co_2P phase (Figure 5.13c). Besides, the clear lattice fringe of ~0.22 nm corresponds to the (210) facet of the NiCoP phase (Figure 5.13d), while the lattice fringe of ~0.172 nm corresponds to the (004) facet of NiP phase (Figure 5.13e). Figure 5.13f demonstrate that the lattice fringes of ~0.191, ~0.189 and ~0.186 nm correspond to the (210), (122) and (013) facets of NiCoP, NiP and Co_2P phases, respectively.

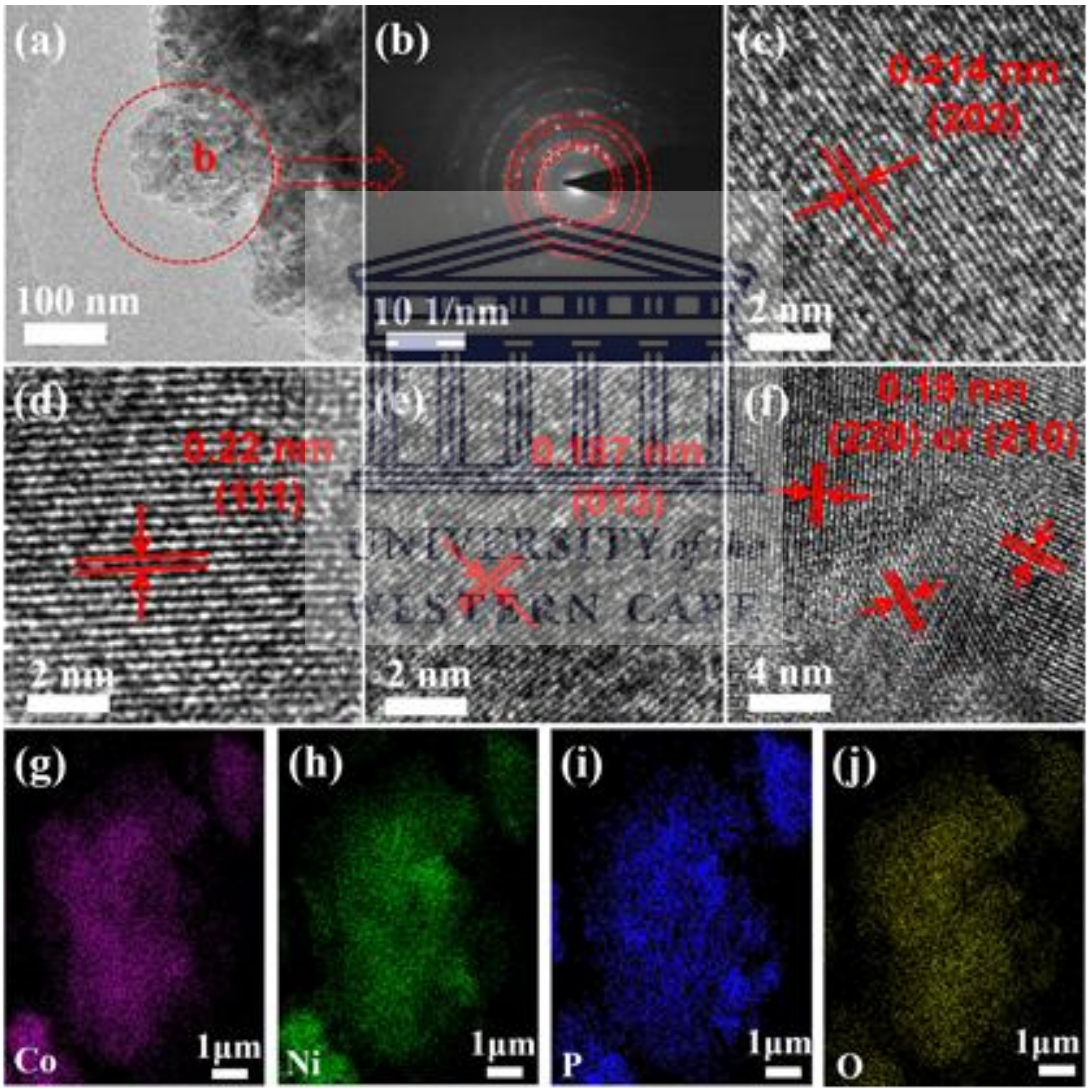

Figure 5.13 (a) TEM image of Ni-Co-P/NF, (b) the corresponding SAED pattern taken from (a), (c–f) HRTEM images, (g–j) the corresponding EDX mappings of Co, Ni, P and O elements.

http://etd.uwc.ac.za/

Obviously, Figures 5.13(a–f) indicate that Ni-Co-P/NF is formed with NiCoP, NiP and Co_2P phases. EDX analysis (Figures 5.13g–5.13j) of Ni-Co-P/NF confirms the uniform distribution of Ni, Co, O and P in Ni-Co-P/NF and the complete formation of bimetallic phosphide compounds. These results are also consistent with the XRD characterization.

Figure 5.14 depicts the hydrogen evolution reaction activity of the as-prepared samples. In order to eliminate the effect of ohmic resistance, all the polarization curves are corrected by *IR* compensation to investigate the intrinsic catalytic behavior. The overpotentials (*vs.* RHE) to deliver current densities of –10, –300, –1500 mA cm^{-2} are labeled as η_{10}, η_{300}, η_{1500}, respectively. The catalytic current density of η_{10} is adopted as a benchmark for comparison.[42]

UNIVERSITY of the
WESTERN CAPE

http://etd.uwc.ac.za/

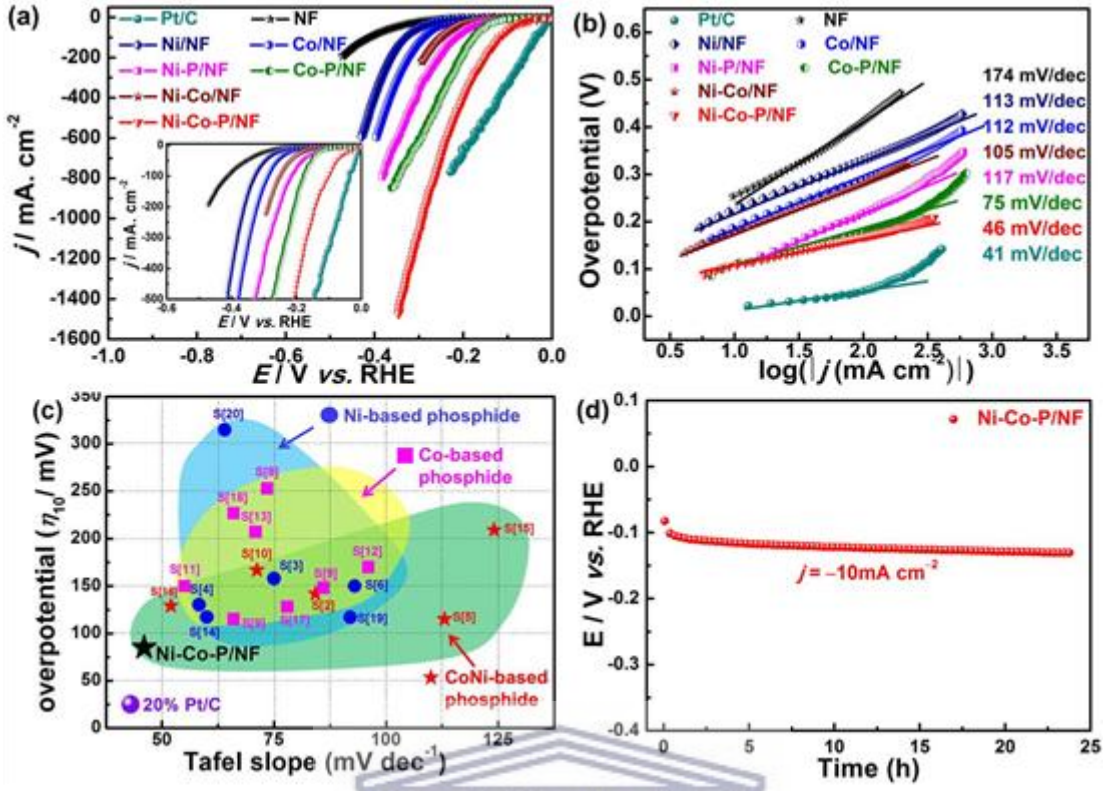

Figure 5.14 Electrochemical measurements of the as-prepared samples for hydrogen evolution in 1.0 M KOH aqueous solution. (a) Polarization curves, (b) corresponding Tafel plots, (c) comparison of the HER activity in 1.0 M KOH aqueous solution for newly reported non-noble metal-based electrocatalysts, (d) chronopotentiometry curve with a constant current at –10 mA cm^{-2}.

UNIVERSITY of the
WESTERN CAPE

The polarization curve recorded for Ni-Co-P/NF (Figure 5.14a) shows 85 mV (η_{10}) of overpotential, which is slightly higher than the observed overpotential for commercial Pt/C (close to zero). On the contrary, the Co-P/NF, Ni-P/NF, Ni-Co/NF, Co/NF, Ni/NF and NF exhibit relatively poor catalytic activity, requiring overpotentials of 96, 107, 144, 185, 224, 253 mV (to deliver –10 mA cm^{-2}), respectively. Remarkably, Ni-Co-P/NF displays a large current density of –500 mA cm^{-2} at 210 mV, while for –1,500 mA cm^{-2} it requires an overpotential of 350 mV. For commercial Pt/C, with an overpotential of 150 mV is required to achieve a current density of –500 mA cm^{-2}. Figure 5.14a indicates that the Ni-Co/NF precursor was

http://etd.uwc.ac.za/

successfully transformed into the bimetallic phosphides (Ni-Co-P/NF), which can significantly improve the HER activity as widely reported. As shown in Figure 5.14b, the catalytic kinetics for HER was evaluated by the Tafel plots, derived according to the Tafel equation. The Ni-Co-P/NF exhibits a Tafel slope of 46 mV dec^{-1}, slightly higher than that of Pt/C (41 mV dec^{-1}), and superior to Co-P/NF (75 mV dec^{-1}), Ni-P/NF (117 mV dec^{-1}), Ni-Co/NF (105 mV dec^{-1}), Co/NF (112 mV dec^{-1}), Ni/NF (113 mV dec^{-1}) and NF (174 mV dec^{-1}). It can be concluded that the bimetallic Ni–Co alloy has better HER activity than single Ni or Co metals, and that the catalytic activity could be improved after phosphatization. More impressively, the optimized Ni-Co-P/NF achieved an unexpectedly low Tafel slop and overpotential, which is much better than those reported for Pt-free phosphate electrocatalysts at η_{10} (Figure 5.14c & Table 5.1; the specific data of Figure 5.14c are listed in Table 5.1). The durability of Ni-Co-P/NF was carried out by keeping the current at –10 mA cm^{-2}, which shows a slight increase in overpotential after working for 24 h (Figure 5.14d), and thus displays good stability.

UNIVERSITY of the
WESTERN CAPE

http://etd.uwc.ac.za/

Table 5.1 Comparison of the HER activity in 1.0 M KOH aqueous solution for several reported non-noble metal-based electrocatalysts (GCE means glassy carbon electrode, CFP means carbon fiber paper, CF means carbon fiber, CNS means carbon nanosheets).

Catalysts	Substrates	η_{10} (mV)	Tafel slope ($mVdec^{-1}$)	references
Ni-Co-P/NF	Ni Foam	85	46	This work
Ni-Fe-P nanosheets	Ni Foam	142	84.24	[43]
Ni–P nanorods	Ni foam	158	75	[44]
Ni/NiP	Ni foam	130	58.5	[45]
CoNiP@NF	Ni foam	155	113	[46]
Ni_2P/NF	Ni foam	150	93	[47]
Pt/C (wt 20%)	GCE	75	111	[48]
Co/CoP-5	GCE	253	73.8	[49]
CoP/NCNHP	GCE	115	66	[50]
CoP/NCP	GCE	148	86	[50]
NiCoP Nanocubes	GCE	167	71.2	[51]
Co_2P nanocrystals	GCE	150	55	[21]
Co_2P@NPG	GCE	170	96	[52]
CoP nanosheets	GCE	111	60	[53]
CoP NS	GCE	207	70.9	[53]
CP@Ni-P	CFP	117	60	[22]
NiCoP/rGO	CFP	209	124	[54]
Co_4Ni_1P NTs	GCE	129	52	[55]
CoP/Ti	Ti foil	128	78	[56]
Ni-P-DF	Copper foil	98	80	[57]
Co-P-DF	Copper foil	227	66	[57]
CF@NPC-CoP	CF	104	61.7	[58]
Ni_2P/CNS	CNS	315	64	[59]

UNIVERSITY of the
WESTERN CAPE

The EIS (Figure 5.15) that fitted with the equivalent circuit was conducted to study the electrode kinetics during the electrocatalytic process. As shown in Figure 5.15, Ni-Co-P/NF provides a charge transfer resistance (about 3.3 Z′/ohm) smaller than Ni-Co/NF and NF, indicating the fastest charge transfer. Besides, the charge-transfer resistance (R_{ct}) corresponds to the diameter of semicircle plotted, and the smaller diameter shows a faster

http://etd.uwc.ac.za/

electron transfer.[60] Figure 5.15 demonstrates an ultrafast Faradaic process, intrinsic metallic behavior and high conductivity of metal phosphides of Ni-Co-P/NF. The XPS data shows that the surface of Ni-Co-P/NF is dominated by phosphate groups, which will affect the surface wettability.[41]

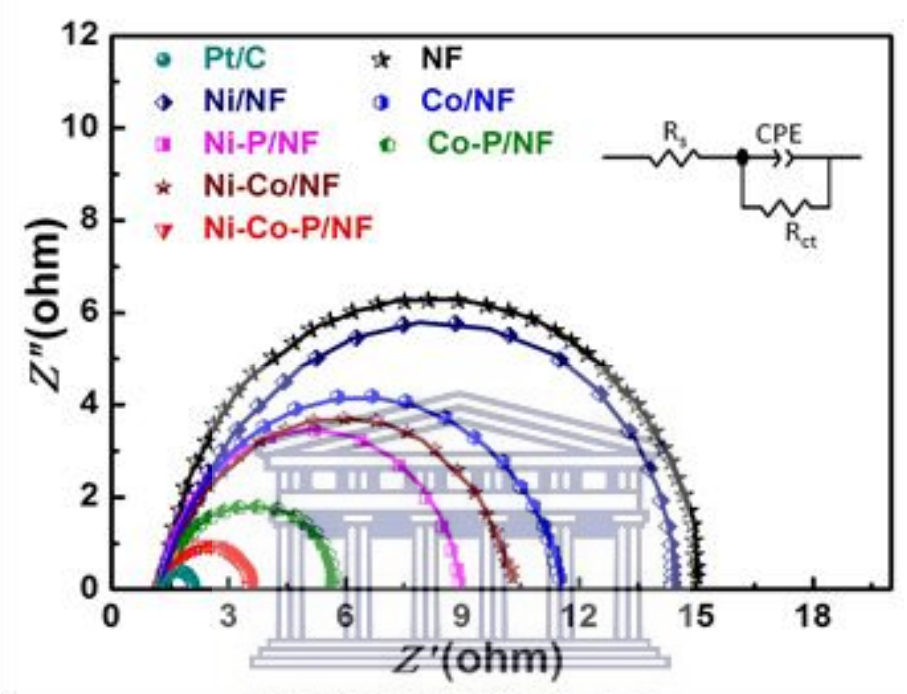

Figure 5.15 Nyquist plots in frequency from 10^5 to 10^2 Hz with a single modulated in 1.0 M KOH aqueous solution for hydrogen evolution reaction.

UNIVERSITY of the
WESTERN CAPE

Moreover, the effective surface areas of the as-prepared samples were estimated by ECSAs, which is positively related to C_{dl}.[61] In Figure 5.16(h), Ni-Co-P/NF exhibits the largest ECSA of 0.402 mF compared with NF (0.020 mF), Ni/NF (0.026 mF), Co/NF (0.043 mF), Ni-Co/NF (0.095 mF), Ni-P/NF (0.131 mF) and Co-P/NF (0.216 mF). The detailed calculation results of ECSA values for all the as-prepared samples are listed in Table 5.2. This result confirms that Ni-Co-P/NF possesses the largest electrochemical surface area among all the electrocatalysts. The large ECSA of Ni-Co-P/NF may be attributed to the Ni–Co phosphides containing abundant active sites for HER.

http://etd.uwc.ac.za/

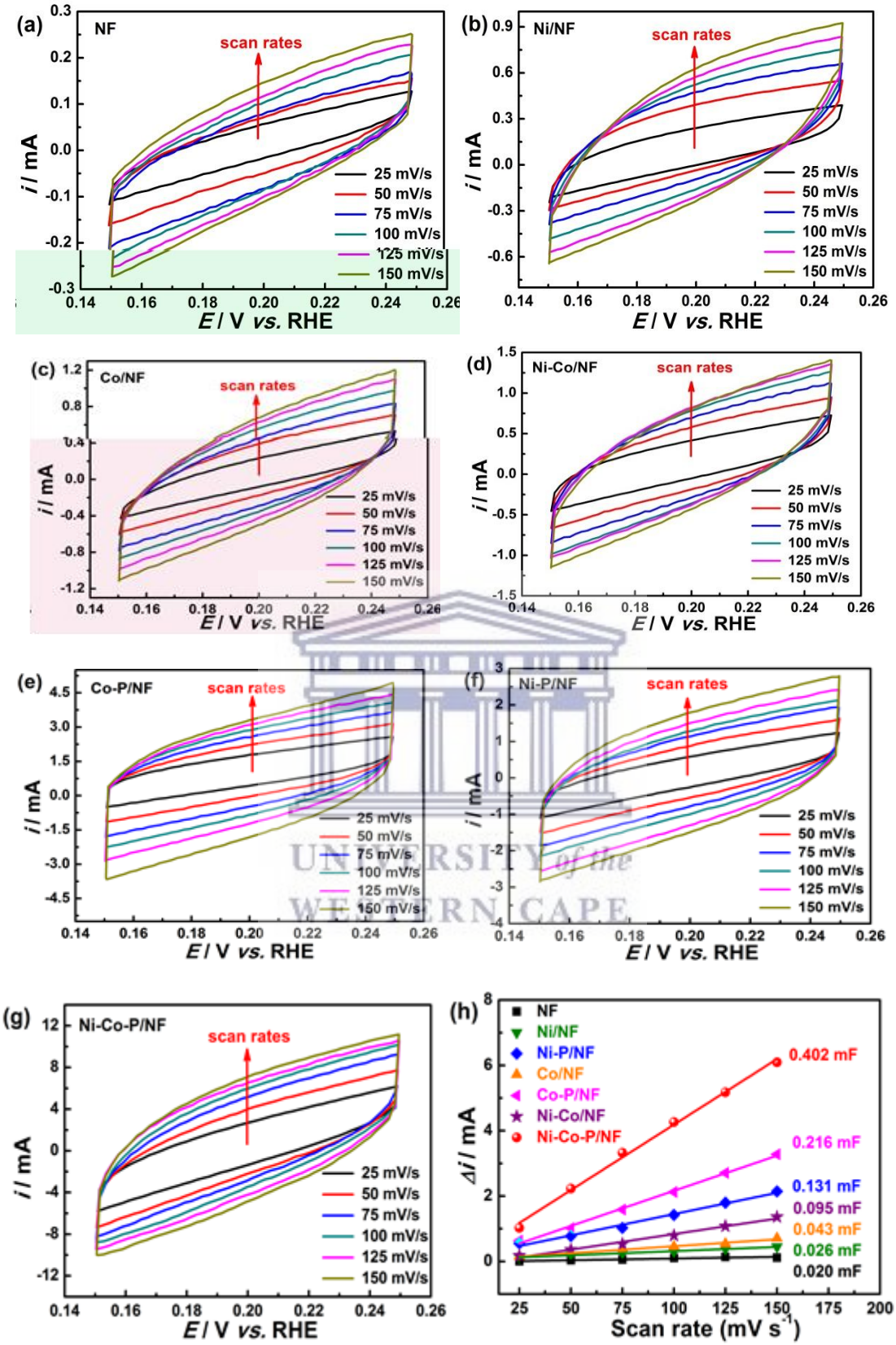

Figure 5.16 (a–g) Double-layer capacitance measurements for determining the ECSAs of all the electrocatalysts from voltammetry curves in 1.0 M KOH with different scan rates. (h) The capacitive currents at 0.20 V against the scan rates.

http://etd.uwc.ac.za/

Table 5.2 The ECSAs, η_{10} and Tafel slopes of all samples.

Sample	C_{dl} mF	C_s mF cm^{-2}	*ECSA* cm^2	η_{10} (mV)	Tafel mV dec^{-1}
NF	0.020	0.04	0.5	297	230
Ni/NF	0.026	0.04	0.65	276	194
Co/NF	0.043	0.04	1.075	250	175
Ni-Co/NF	0.095	0.04	2.375	238	123
Ni-P/NF	0.131	0.04	3.275	227	107
Co-P/NF	0.216	0.04	5.40	214	87
Ni-Co-P/NF	0.402	0.04	10.05	178	60

According to the formula: $j = i/\text{ECSA}$,[61] HER activities (current density) and corresponding Tafel slope of the samples are normalized by their ECSAs (Figure 5.17). As shown in Figure 5.17(a), the normalized HER activity is consistent with the original data. The results show that the Ni-Co-P/NF has a larger current at the same electrochemical surface area, indicating better intrinsic activity.

UNIVERSITY of the
WESTERN CAPE

http://etd.uwc.ac.za/

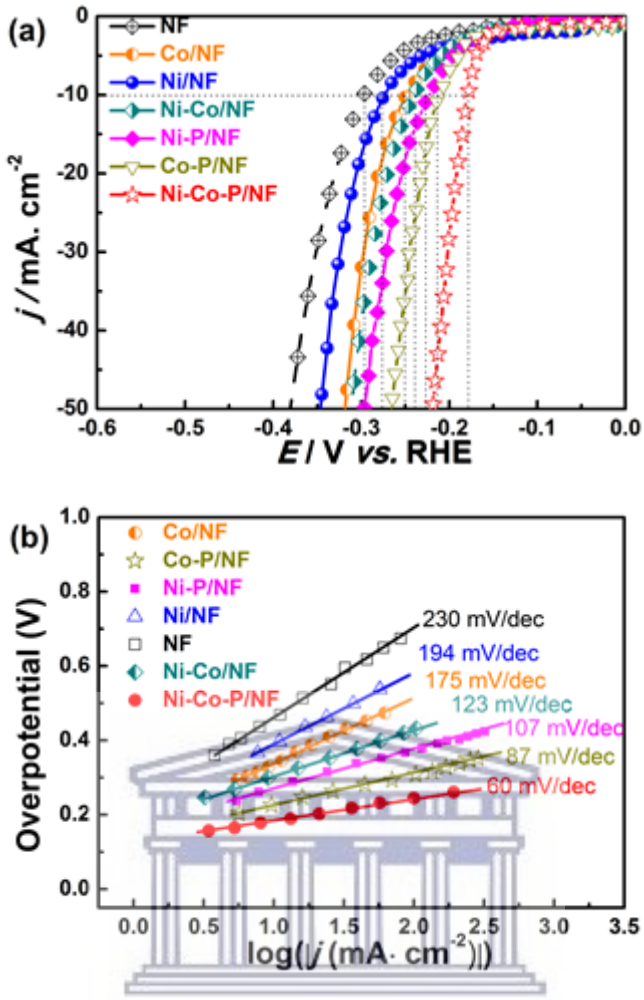

Figure 5.17 (a) The normalized HER activities (current density) by their ESCAs; (b) the corresponding Tafel slopes.

UNIVERSITY of the
WESTERN CAPE

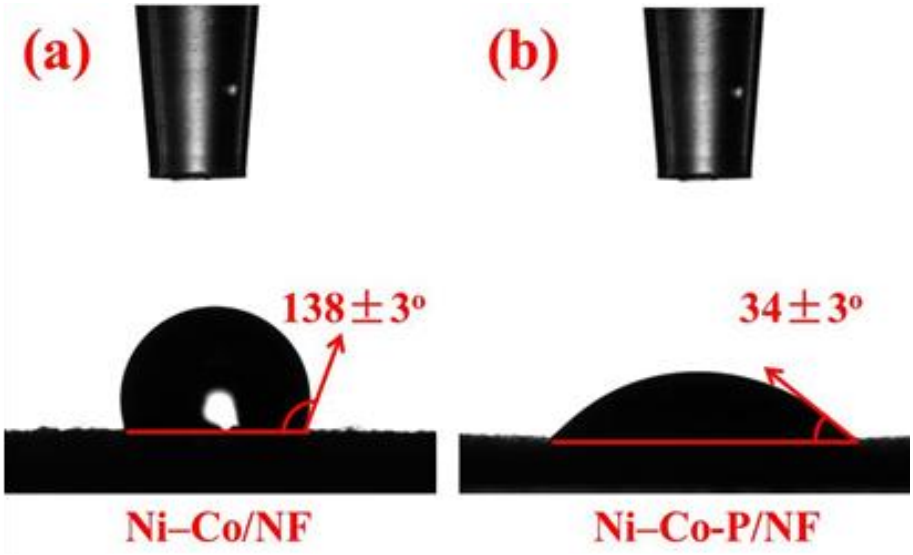

Figure 5.18 The Contact angles of (a) Ni-Co/NF and (b) Ni-Co-P/NF.

http://etd.uwc.ac.za/

Figures 5.18 (a & b) are show the contact angles of Ni-Co/NF and Ni-Co-P/NF electrocatalyst. The Ni-Co-P/NF has much smaller contact angle 34 ± 3° than the Ni-Co/NF (138 ± 3°), indicating an enhanced compatibility and affinity to water after phosphorylation, thus leading to an improvement in its catalytic activity towards HER. Furthermore, in order to prove the binding strength of the self-supported Ni-Co-P/NF (Figure 5.19), it was put into deionized water for ultrasonication 30 min at a frequency of 42 kHz/s and a power of 300 W. Almost no powder was noted to fall off from the nickel foam substrate, demonstrating good binding strength.

UNIVERSITY of the
WESTERN CAPE

Figure 5.19 (a) Before and (b) after ultrasonication for 30 min.

In summary, the high performance of Ni-Co-P/NF electrode could be attributed to: i) the synergy effect between NiCoP, NiP and Co_2P phases, ii) the large electrochemical active area, iii) the high surface wettability, and iv) the self-supported nanostructure fast electron transfer rate in water splitting.

http://etd.uwc.ac.za/

5.4. Conclusions

In this work, a two-step method was developed to fabricate a self-supported nanosheets arrays Ni-Co-P/NF nanocomposite electrode for the hydrogen evolution reaction. It was demonstrated that the bimetallic cobalt-nickel phosphide has great potential for hydrogen evolution at high current densities. The as-prepared Ni-Co-P/NF electrode exhibits a very good HER activity with an overpotential of 85 mV and shows high stability for 24 h in 1.0 M KOH aqueous solution.

The good performance of Ni-Co-P/NF could be attributed to: (i) the synergy effect of three phases, such as Co_2P, NiP and NiCoP phases, (ii) the unique morphology of Ni-Co-P/NF electrode with randomly growing newborn nanosheets dispersed on villiform 3D integrated framework, which could expose more surface area and lead to the full use of active sites of the electrocatalyst for HER, (iii) the Ni-Co-P prepared by electrodeposition is strongly bonded with the nickel foam substrate, being greatly beneficial to the physical and electrochemical stability of long-term water electrolysis, and (iv) the large electrochemically active area and relatively high surface wettability. Therefore, this work provides a mechanism for the synthesis of low-cost electrocatalyst with high efficiency for hydrogen evolution, which also offers a promising opportunity for the large-scale application of phosphides in alkaline electrolysis ascribed to their higher current density and impressive low overpotential.

UNIVERSITY of the
WESTERN CAPE

http://etd.uwc.ac.za/

5.5 References

1. Jing SY, Lu JJ, Yu GT, Yin SB, Luo L, Zhang ZS, Ma YF, Chen W, Shen PK. Carbon-encapsulated WO_x hybrids as efficient catalysts for hydrogen evolution. *Adv. Mater.*, 2018, 30(28), 1705979.
2. Burke MS, Kast MG, Trotochaud L, Smith AM, Boettcher SW. Cobalt-iron (oxy)hydroxide oxygen evolution electrocatalysts: The role of structure and composition on activity, stability, and mechanism. *J. Am. Chem. Soc.*, 2015, 137(10), 3638-3648.
3. Lu JJ, Zhang LS, Jing SY, Luo L, Yin SB. Remarkably efficient PtRh alloyed with nanoscale WC for hydrogen evolution in alkaline solution. *Inter. J. Hydrogen Energy*, 2017, 42(9), 5993-5999.
4. An K, Xu XX. Mo_2C based electrocatalyst with nitrogen doped three-dimensional mesoporous carbon as matrix, synthesis and HER activity study. *Electrochim. Acta*, 2019, 293, 348-355.
5. Kim SK, Qiu Y, Zhang YJ, Hurt R, Peterson A. Nanocomposites of transition-metal carbides on reduced graphite oxide as catalysts for the hydrogen evolution reaction. *Appl. Catal., B*, 2018, 235, 36-44.
6. Park H, Encinas A, Scheifers JP, Zhang Ym, Fokwa BPT. Boron-dependency of molybdenum boride electrocatalysts for the hydrogen evolution reaction. *Angew. Chem. Inter. Ed.*, 2017, 56(20), 5575-5578.
7. Qian JM, Wang TT, Xia BR, Xi PX, Gao DQ. Zn-doped $MoSe_2$ nanosheets as high-performance electrocatalysts for hydrogen evolution reaction in acid media. *Electrochim. Acta*, 2019, 296, 701-708.
8. Sivanantham A, Shanmugam S. Nickel selenide supported on nickel foam as an efficient and durable non-precious electrocatalyst for the alkaline water electrolysis. *Appl. Catal., B*, 2017, 203, 485-493.
9. Jing SY, Zhang LS, Luo L, Lu JJ, Yin SB, Shen PK, Tsiakaras P. N-Doped porous molybdenum carbide nanobelts as efficient catalysts for hydrogen evolution reaction. *Appl. Catal., B*, 2018, 224, 533-540.

UNIVERSITY of the
WESTERN CAPE

http://etd.uwc.ac.za/

10. Tang CY, Hu Q, Li FJ, He CX, Chai XY, Zhu CZ, Liu JH, Zhang QL, Zhu B, Fan LD. Coupled molybdenum carbide and nitride on carbon nanosheets: An efficient and durable hydrogen evolution electrocatalyst in both acid and alkaline media. *Electrochim. Acta*, 2018, 280, 323-331.
11. Boppella R, Yang W, Tan J, Kwon H-C, Park J, Moon J. Black phosphorus supported Ni_2P co-catalyst on graphitic carbon nitride enabling simultaneous boosting charge separation and surface reaction. *Appl. Catal., B*, 2019, 242, 422-430.
12. Ullah N, Zhao WT, Lu XQ, Oluigbo CJ, Shah SA, Zhang MM, Xie JM, Xu YG. In situ growth of M-MO (M = Ni, Co) in 3D graphene as a competent bifunctional electrocatalyst for OER and HER. *Electrochim. Acta*, 2019, 298, 163-171.
13. Wu CB, Zhang JF, Guo JA, Sun LX, Ming J, Dong HL, Zhao YC, Tian JN, Yang XL. Ceria-induced strategy to tailor Pt atomic clusters on cobalt-nickel oxide and the synergetic effect for superior hydrogen generation. *ACS Sustainable Chem. Eng.*, 2018, 6(6), 7451-7457.
14. Czioska S, Wang JY, Teng X, Chen ZF. Hierarchically structured $CuCo_2S_4$ nanowire arrays as efficient bifunctional electrocatalyst for overall water splitting. *ACS Sustainable Chem. Eng.*, 2018, 6(9), 11877-11883.
15. Li JW, Xu PM, Zhou RF, Li RC, Qiu LJ, Jiang SP, Yuan DS. Co_9S_8-Ni_3S_2 heterointerfaced nanotubes on Ni foam as highly efficient and flexible bifunctional electrodes for water splitting. *Electrochim. Acta*, 2019, 299, 152-162.
16. Callejas JF, Read CG, Popczun EJ, McEnaney JM, Schaak RE. Nanostructured Co_2P electrocatalyst for the hydrogen evolution reaction and direct comparison with morphologically equivalent CoP. *Chem. Mater.*, 2015, 27(10), 3769-3774.
17. Read CG, Callejas JF, Holder CF, Schaak RE. General strategy for the synthesis of transition metal phosphide Films for electrocatalytic hydrogen and oxygen evolution. *ACS Appl. Mater. Interfaces*, 2016, 8(20), 12798-12803.
18. Pu ZH, Amiinu IS, Zhang CT, Wang M, Kou ZK, Mu SC. Phytic acid-derivative transition metal phosphides encapsulated in N,P-codoped carbon: an efficient and durable hydrogen evolution electrocatalyst in a wide pH range. *Nanoscale*, 2017, 9(10), 3555-3560.

UNIVERSITY of the
WESTERN CAPE

http://etd.uwc.ac.za/

19. Infantes-Molina A, Moreno-Leon C, Pawelec B, Fierro JLG, Rodriguez-Castellon E, Jimenez-Lopez A. Simultaneous hydrodesulfurization and hydrodenitrogenation on MoP/SiO_2 catalysts: Effect of catalyst preparation method. *Appl. Catal., B*, 2012, 113, 87-99.
20. Hou CC, Chen QQ, Wang CJ, Liang F, Lin ZS, Fu WF, Chen Y. Self-supported cedarlike semimetallic Cu_3P nanoarrays as a 3D high-performance janus electrode for both oxygen and hydrogen evolution under basic conditions. *ACS Appl. Mater. Interfaces*, 2016, 8(35), 23037-23048.
21. Liang QS, Huang KK, Wu XF, Wang XY, Ma W, Feng SH. Composition-controlled synthesis of $Ni_{2-x}Co_xP$ nanocrystals as bifunctional catalysts for water splitting. *RSC Adv.*, 2017, 7(13), 7906-7913.
22. Wang XG, Li W, Xiong DH, Petrovykh DY, Liu LF. Bifunctional nickel phosphide nanocatalysts supported on carbon fiber paper for highly efficient and stable overall water splitting. *Adv. Funct. Mater.*, 2016, 26(23), 4067-4077.
23. Lu JJ, Yin SB, Shen PK. Carbon-encapsulated electrocatalysts for the hydrogen evolution reaction. *Electrochem. Energy Rev.*, 2019, 2(1), 105-127.
24. Xu M, Huang L, Fang YX, Han L, Yu Y, Dong SJ. The unified ordered mesoporous carbons supported Co-based electrocatalysts for full water splitting. *Electrochim. Acta*, 2018, 261, 412-420.
25. Yao MQ, Wang N, Hu WC, Komarneni S. Novel hydrothermal electrodeposition to fabricate mesoporous film of $Ni_{0.8}Fe_{0.2}$ nanosheets for high performance oxygen evolution reaction. *Appl. Catal., B*, 2018, 233, 226-233.
26. Yang QP, Lv CC, Huang ZP, Zhang C. Amorphous film of ternary Ni-Co-P alloy on Ni foam for efficient hydrogen evolution by electroless deposition. *Inter. J. Hydrogen Energy*, 2018, 43(16), 7872-7880.
27. Gong YQ, Xu ZF, Pan HL, Lin Y, Yang Z, Wang JL. A 3D well-matched electrode pair of Ni-Co-S//Ni-Co-P nanoarrays grown on nickel foam as a high performance electrocatalyst for water splitting. *J. Mater. Chem. A*, 2018, 6(26), 12506-12514.
28. Zhou XX, Zhou J, Huang GP, Fan RL, Ju S, Mi ZT, Shen MR. A bifunctional and stable Ni-Co-S/Ni-Co-P bistratal electrocatalyst for 10.8%-efficient overall solar water splitting. *J. Mater. Chem. A*, 2018, 6(41), 20297-20303.

UNIVERSITY of the
WESTERN CAPE

http://etd.uwc.ac.za/

29. Du ZL, Jannatun N, Yu DY, Ren J, Huang WH, Lu X. C-60-Decorated nickel-cobalt phosphide as an efficient and robust electrocatalyst for hydrogen evolution reaction. *Nanoscale*, 2018, 10(48), 23070-23079.

30. Hou CC, Li Q, Wang CJ, Peng CY, Chen QQ, Ye HF, Fu WF, Che CM, Lopez N, Chen Y. Ternary Ni-Co-P nanoparticles as noble-metal-free catalysts to boost the hydrolytic dehydrogenation of ammonia-borane. *Energy Environ. Sci.*, 2017, 10(8), 1770-1776.

31. Karpuz A, Kockar H, Alper M. Effect of film thickness on properties of electrodeposited Ni-Co films. *Appl. Surface Sci.*, 2012, 258(12), 5046-5051.

32. Zhang LS, Lu JJ, Yin SB, Luo L, Jing SY, Brouzgou A, Chen JH, Shen PK, Tsiakaras P. One-pot synthesized boron-doped RhFe alloy with enhanced catalytic performance for hydrogen evolution reaction. *Appl. Catal., B*, 2018, 230, 58-64.

33. Ding LN, Shu YY, Wang AQ, Zheng MY, Li L, Wang XD, Zhang T. Preparation and catalytic performances of ternary phosphides NiCoP for hydrazine decomposition. *Appl. Catal., A*, 2010, 385(1-2), 232-237.

34. Pornea AM, Abebe MW, Kim H. Ternary NiCoP urchin like 3D nanostructure supported on nickel foam as a catalyst for hydrogen generation of alkaline $NaBH_4$. *Chem. Phys.*, 2019, 516, 152-159.

35. Chen C, Yan D, Luo X, Gao WJ, Huang GJ, Han ZW, Zeng Y, Zhu ZH. Construction of core-shell $NiMoO_4$@Ni-Co-S nanorods as advanced electrodes for high-performance asymmetric supercapacitors. *ACS Appl. Mater. Interfaces*, 2018, 10(5), 4662-4671.

36. He LB, Zhou D, Lin Y, Ge RX, Hou XD, Sun XP, Zheng CB. Ultrarapid in situ synthesis of Cu_2S nanosheet arrays on copper foam with room-temperature-active iodine plasma for efficient and cost-effective oxygen evolution. *ACS Catal.*, 2018, 8(5), 3859-3864.

37. Wang RH, Xu CH, Lee JM. High performance asymmetric supercapacitors: New NiOOH nanosheet/graphene hydrogels and pure graphene hydrogels. *Nano Energy*, 2016, 19, 210-221.

38. Fang ZW, Peng LL, Qian YM, Zhang X, Xie YJ, Cha JJ, Yu GH. Dual tuning of Ni-Co-A (A = P, Se, O) nanosheets by anion substitution and holey engineering for efficient hydrogen evolution. *J. Am. Chem. Soc.*, 2018, 140(15), 5241-5247.

UNIVERSITY of the
WESTERN CAPE

http://etd.uwc.ac.za/

39. Xiaoping Dai ML, Zhanzhao Li, Axiang Jin, Yangde Ma, Xingliang Huang, Hui Sun, Hai Wang, and Xin Zhang. Molybdenum Polysulfide Anchored on Porous Zr-Metal Organic Framework to Enhance the Performance of Hydrogen Evolution Reaction. *J. Phys. Chem. C*, 2016, 120, 12539-12548.

40. Tian JQ, Liu Q, Asiri AM, Sun XP. Self-supported nanoporous cobalt phosphide nanowire arrays: An efficient 3D hydrogen-evolving cathode over the wide range of pH 0-14. *J. Am. Chem. Soc.*, 2014, 136(21), 7587-7590.

41. Li YB, Zhao C. Enhancing water oxidation catalysis on a synergistic phosphorylated NiFe hydroxide by adjusting catalyst wettability. *ACS Catal.*, 2017, 7(4), 2535-2541.

42. Zhang PL, Chen H, Wang M, Yang Y, Jiang J, Zhang BB, Duan LL, Daniel Q, Li F, Sun LC. Gas-templating of hierarchically structured Ni-Co-P for efficient electrocatalytic hydrogen evolution. *J. Mater. Chem. A*, 2017, 5(16), 7564-7570.

43. Ma ZZ, Li RX, Wang M, Meng HJ, Zhang F, Bao XQ, Tang B, Wang XG. Self-supported porous Ni-Fe-P composite as an efficient electrocatalyst for hydrogen evolution reaction in both acidic and alkaline medium. *Electrochim. Acta*, 2016, 219, 194-203.

44. Xing JL, Zou ZH, Guo KL, Xu CL. The effect of phosphating time on the electrocatalytic activity of nickel phosphide nanorod arrays grown on Ni foam. *J. Mater. Res.*, 2018, 33(5), 556-567.

45. Chen GF, Ma TY, Liu ZQ, Li N, Su YZ, Davey K, Qiao SZ. Efficient and stable bifunctional electrocatalysts Ni/Ni_xM_y(M = P, S) for overall water splitting. *Adv. Funct. Mater.*, 2016, 26(19), 3314-3323.

46. Han AL, Chen HL, Zhang HY, Sun ZJ, Du PW. Ternary metal phosphide nanosheets as a highly efficient electrocatalyst for water reduction to hydrogen over a wide pH range from 0 to 14. *J. Mater. Chem. A*, 2016, 4(26), 10195-10202.

47. You B, Jiang N, Sheng M, Bhushan MW, Sun Y. Hierarchically Porous Urchin-Like Ni2P Superstructures Supported on Nickel Foam as Efficient Bifunctional Electrocatalysts for Overall Water Splitting. *ACS Catal.*, 2016, 6(2), 714-721.

48. Pei Y, Yang Y, Zhang Ff, Dong P, Baines R, Ge Yc, Chu H, Ajayan PM, Shen Jf, Ye Mx. Controlled electrodeposition synthesis of Co-Ni-P film as a flexible and inexpensive electrode for efficient overall water splitting. *ACS Appl. Mater. Interfaces*, 2017, 9(37), 31887-31896.

UNIVERSITY of the WESTERN CAPE

http://etd.uwc.ac.za/

49. Xue ZH, Su H, Yu QY, Zhang B, Wang HH, Li X-H, Chen JS. Janus Co/CoP nanoparticles as efficient mott-schottky electrocatalysts for overall water splitting in wide pH range. *Adv. Energy Mater.*, 2017, 7(12), 1602355.

50. Guang-Feng Wei L-RZaZ-PL. Group-VIII transition metal boride as promising hydrogen evolution reaction catalysts. *Phys. Chem. Chem. Phys.*, 2018, 20, 27752.

51. Feng Y, Yu XY, Paik U. Nickel cobalt phosphides quasi-hollow nanocubes as an efficient electrocatalyst for hydrogen evolution in alkaline solution. *Chem. Commun.*, 2016, 52(8), 1633-1636.

52. Zhuang MH, Ou XW, Dou YB, Zhang LL, Zhang QC, Wu RZ, Ding Y, Shao MH, Luo ZT. Polymer-embedded fabrication of Co_2P nanoparticles encapsulated in N,P-doped graphene for hydrogen generation. *Nano Lett.*, 2016, 16(7), 4691-4698.

53. Chang JF, Liang L, Li CY, Wang ML, Ge JJ, Liu CP, Xing W. Ultrathin cobalt phosphide nanosheets as efficient bifunctional catalysts for a water electrolysis cell and the origin for cell performance degradation. *Green Chem.*, 2016, 18(8), 2287-2295.

54. Li JY, Yan M, Zhou XM, Huang ZQ, Xia ZM, Chang CR, Ma YY, Qu YQ. Mechanistic insights on ternary $Ni_{2-x}Co_xP$ for hydrogen evolution and their hybrids with graphene as highly efficient and robust catalysts for overall water splitting. *Adv. Funct. Mater.*, 2016, 26(37), 6785-6796.

55. Yan LT, Cao L, Dai PC, Gu X, Liu DD, Li LJ, Wang Y, Zhao XB. Metal-organic frameworks derived nanotube of nickel-cobalt bimetal phosphides as highly efficient electrocatalysts for overall water splitting. *Adv. Funct. Mater.*, 2017, 27(40), 1703455.

56. Tang C, Zhang R, Lu WB, He LB, Jiang X, Asiri AM, Sun XP. Fe-doped CoP nanoarray: A monolithic multifunctional catalyst for highly efficient hydrogen generation. *Adv. Mater.*, 2017, 29(2), 1602441.

57. Zhang PL, Chen H, Wang M, Yang Y, Jiang J, Zhang BB, Duan LL, Daniel QT, Li FS, Sun LC. Gas-templating of hierarchically structured Ni-Co-P for efficient electrocatalytic hydrogen evolution. *J. Mater. Chem. A*, 2017, 5(16), 7564-7570.

58. Xiao J, Zhang ZY, Zhang Y, Lv QY, Jing F, Chi K, Wang S. Large-scale printing synthesis of transition metal phosphides encapsulated in N, P co-doped carbon as highly efficient hydrogen evolution cathodes. *Nano Energy*, 2018, 51, 223-230.

UNIVERSITY of the
WESTERN CAPE

http://etd.uwc.ac.za/

59. Li Y, Cai P, Ci Sq, Wen Zh. Strongly coupled 3D nanohybrids with Ni_2P/carbon nanosheets as pH-universal hydrogen evolution reaction electrocatalysts. *Chemelectrochem*, 2017, 4(2), 340-344.

60. Li YJ, Zhang HC, Jiang M, Kuang Y, Sun XM, Duan X. Ternary NiCoP nanosheet arrays: An excellent bifunctional catalyst for alkaline overall water splitting. *Nano Res.*, 2016, 9(8), 2251-2259.

61. Xu F, Lu JJ, Luo L, Yu C, Tang Z, Hanna S. Abbo, Salam J. J. Titinchi, Zhu JL, Shen PK, Yin SB. Cu_2S-Cu_3P nanowire arrays self-supported on copper foam as boosting electrocatalysts for hydrogen evolution. *Energy Technolgy*, 2019, 1800993.

UNIVERSITY of the
WESTERN CAPE

http://etd.uwc.ac.za/

CHAPTER 6 Conclusion and Prospective

Energy and the environment are the two eternal themes of human society. In order to achieve the sustainable development of human society and environment, it is significant to develop clean and renewable energy sources. Hydrogen is considered to be the most ideal choice, which forms the foundation of the hydrogen energy economy, and the research on hydrogen production and fuel cells involved in its production and utilization are naturally a vital research endeavor in the world.

Electrocatalysts are one of the key materials for proton exchange member fuel cells and water splitting. The use of electrocatalysts can effectively reduce the reaction energy barriers and improve the energy conversion efficiency. Therefore, the study of low-cost, high activity and excellent stability electrocatalysts are essential for the development of proton exchange member fuel cells and water splitting.

In this thesis, three different kinds of electrocatalysts for oxygen reduction reaction and hydrogen evolution are studied:

UNIVERSITY of the
WESTERN CAPE

(1) Nitrogen-doped PtNiMo ternary alloys were synthesized by impregnation reduction followed by annealing at high temperatures. The introduction of acid-resistant Mo atoms in the alloy not only stabilizes the near-surface Pt atoms, enhancing the catalytic stability, but also changes the electronic structure of adjacent Pt atoms and thus promote the desorption of oxide intermediates. The doped N can form Ni_4N with Ni at high temperature and is stabilized in the electrocatalyst to thus improve stability. Meanwhile, the pyridine N and pyrrole N also formed by annealing the carbon substrate in an NH_3 atmosphere and possess a promoting effect on oxygen

http://etd.uwc.ac.za/

reduction. By adjusting the near-surface Pt atom's content to balance the activity and stability, Pt_3Ni_3MoN/C shows the best activity and stability. It showed mass activity of 900 mA mg^{-1} Pt at 0.90V *vs*. RHE in O_2-saturated 0.1 mol L^{-1} $HClO_4$ aqueous solutions, which is 3.75-fold higher than the commercial TKK Pt/C (240 mA mg^{-1} Pt). After 30k accelerated durability tests, the mass activity of Pt_3Ni_3MoN/C is still 690 mA mg^{-1} Pt, which activity remains ~75%, while the Pt/C merely retains ~44%.

(2) Fabrication of self-supported Cu_2S-Cu_3P NW arrays on cupper foam by liquid-solid reaction and subsequent phosphidation at low temperature are used as an integrated electrode for hydrogen evolution. No binding agents are needed to favor excellent catalytic activity for HER and it only requires a low overpotential of 158 mV to achieve a current density of 10 mA cm^{-2} and it displays a small Tafel slope of 45 mV dec^{-1}. In addition, the activity decrease is ignorable after holding at –500 mA cm^{-2} for a period of 75 h which demonstrates excellent stability, and the possible mechanisms are also discussed in the thesis.

UNIVERSITY of the
WESTERN CAPE

(3) A two-step method was developed to fabricate a self-supported nanosheets arrays Ni-Co-P/NF nanocomposite electrode for hydrogen evolution. It was displayed that the bimetallic cobalt-nickel phosphide has great potential for HER at high current densities. The as-prepared Ni-Co-P/NF electrode exhibits a very good HER activity with overpotential of 85 mV and shows high stability for 24 h in 1.0 M KOH aqueous solution. The reasons for such good performance are also discussed; this work provides a mechanism for the synthesis of low-cost electrocatalyst with high efficiency for hydrogen evolution, which also offers a promising opportunity for the large-scale application of

http://etd.uwc.ac.za/

phosphides in alkaline electrolysis ascribed to their higher current density and impressive low overpotential.

While, there are still some issues need to be further studied.

(1) By means of simulation calculation, such as Density Functional Theory, the theoretical model of different element doping electrocatalysts could be further constructed. Specifically, the lattice constants, alloy formation energy, surface segregation energy, oxygen adsorption energy and *d* orbital state density of different scales, different elemental compositions, and different element ratios could be investigated. Summarizing the changes and laws of the active center, predicting the activity and stability of the electrocatalyst, and guiding the catalytic materials design, this is efficient for the design of highly activity electrocatalytic materials.

(2) In-situ electrochemical studies could be carried out by environmental spherical aberration transmission electron microscopy to observe the active sites of the reactants on the electrocatalysts surface, and their adsorption and/or desorption and conversion processes, the dissolution, migration, agglomeration and re-deposition of metal atoms. Such on-line observations could be combined with the theoretical simulation and physical property characterization, which is significant for us to understand the instinct reasons for the enhanced catalytic activities. As a result, the binding state of the metal active component to the support material could be studied at the atomic level, which is helpful for further understanding the structure-effect relationship of the as-prepared electrocatalysts.

UNIVERSITY of the
WESTERN CAPE

http://etd.uwc.ac.za/

(3) The as-prepared electrocatalysts could be further fabricated into a membrane electrode for single cell characterization. For hydrogen evolution, a single cell combined with Liquid chromatography could be used to test the efficiency for actual hydrogen evolution, which is also useful for us to further understand the relationship between the electrocatalyst and the performance of the single cell, and this is conducive to the combination of theory, experiment and practical applications.

UNIVERSITY of the
WESTERN CAPE

http://etd.uwc.ac.za/